EXPLORING SPATIAL AND COMPOSITIONAL CONTROL OF CONDUCTIVE MATERIALS USING ATOMIC LAYER DEPOSTION

A DISSERTATION SUBMITTED TO
THE DEPARTMENT OF CHEMICAL ENGINEERING AND
THE COMMITTEE ON GRADUATE STUDIES OF
STANFORD UNIVERSITY IN PARTIAL FULFILLMENT OF
THE REQUIRMENTS FOR THE DEGREE OF
DOCTOR OF PHILOSOPHY

Marja N. Mullings

March 2013

© 2013 by Marja Nicki-Dee Mullings. All Rights Reserved.
Re-distributed by Stanford University under license with the author.



This work is licensed under a Creative Commons Attribution-Noncommercial 3.0 United States License.
http://creativecommons.org/licenses/by-nc/3.0/us/

This dissertation is online at: http://purl.stanford.edu/rx232cf1896

I certify that I have read this dissertation and that, in my opinion, it is fully adequate in scope and quality as a dissertation for the degree of Doctor of Philosophy.

Stacey Bent, Primary Adviser

I certify that I have read this dissertation and that, in my opinion, it is fully adequate in scope and quality as a dissertation for the degree of Doctor of Philosophy.

Curtis Frank

I certify that I have read this dissertation and that, in my opinion, it is fully adequate in scope and quality as a dissertation for the degree of Doctor of Philosophy.

Thomas Jaramillo

Approved for the Stanford University Committee on Graduate Studies.

Patricia J. Gumport, Vice Provost Graduate Education

This signature page was generated electronically upon submission of this dissertation in electronic format. An original signed hard copy of the signature page is on file in University Archives.

This page is intentionally left blank.

ABSTRACT

Consumer-driven demand for affordable, smaller and more sophisticated devices has driven advances in nanoscale engineering. Many of these products, whether they are consumer electronics, fuel cells or photovoltaics, are comprised of significant quantities of scarce, expensive and sometimes toxic materials. Manufacturing affordable and more environmentally benign products on decreasing length scales requires more economical use of scarce resources and the exploration of alternative and abundant materials.

Platinum, as one example, is an outstanding catalyst used in automotive, fine chemical and fuel cell applications; however, it is extremely scarce and costly. Placing platinum only where needed and in small quantities to achieve desired performance may help economize its usage. Because nanoscale feature size and spacing influence catalytic behavior, being able to control these parameters may enable the careful engineering of more powerful platinum catalysts. Another scarce and expensive material whose usage follows rising consumer demand for electronics and photovoltaics is indium. Indium tin oxide is the industry standard transparent conducting oxide (TCO) for high-end electronics. The engineering of high-quality yet poorly-understood indium-free alternative metal oxides using earth-abundant and inexpensive materials may further the development of more powerful and advanced devices. In this dissertation, atomic layer deposition (ALD), a promising ultra-thin film growth technique, is used to selectively deposit small amounts of platinum and to alloy zinc tin oxide in order to address these concerns of scarcity and rising costs.

ALD consists of self-limiting, gas-surface half-reactions separated by inert gas purges which allows for highly controlled growth of nanoscale materials. Because ALD is based on surface reactions, selectively blocking nucleation sites by passivating growth surfaces allows for the deposition of material only where desired. The spatial deposition of platinum using ALD is demonstrated in two studies. In the first, a water-soluble polymer, polymethacrylamide (PMAM) acts as a resist to ALD and allowed the deposition of very small features of platinum. In the second study, surface passivation by means of controlling defect site density in self-assembled monolayers (SAMs) also serves as a growth template to control the aerial density and size of platinum nanoparticles deposited via ALD.

The highly tunable nature of the chemistry of each precursor half-reaction in ALD enables the careful alloying or doping of materials in any desired ratio. A range of compositions for the indium-free TCO alternative, zinc tin oxide (ZTO), is explored by varying the dosing cycle ratios of tin oxide (SnO_x) and zinc oxide (ZnO) in each ALD super cycle. Because the effects of ZTO composition on conduction behavior and optical properties are not well understood, having nanoscale control over how the constituent metal oxides grow on one another is an effective approach to learning more about these properties. As a result, ALD is explored as a flexible system to allow for compositional sampling and variation of film lamination in ZTO. The characteristics of ZTO ALD and the structural and optical properties of these films were shown to vary significantly as a function of degree of lamination and composition. These findings suggest that having nanoscale control over these film characteristics via ALD can lead

to further understanding of ZTO. The ALD of ZTO provides an excellent system for the nanoengineering of this material as an indium-free TCO or buffer layer in solar cells.

ACKNOWLEDGEMENTS

The help and support of many wonderful individuals made possible the completion of this thesis. My family, friends, commitment to personal fitness and newfound interests in the fiber arts played important roles in helping me with this challenging undertaking.

The desire to have a greater diversity of career opportunities beyond being a plant engineer was the key driver behind my decision to attend graduate school. The promise of being able to play a role, no matter how minor, in cutting edge research in a field of my choice was exciting. When I began my graduate studies, my interests were not firm but seemed to be aligned with biological research. When I became acquainted with the collegiality of members of the Bent Research Group and with Professor Stacey Bent after interviewing her for an article in the *Stanford Scientific Magazine,* I was confident that I had found a good fit. I am very grateful to Stacey for accepting me into her group. Without her continued support and guidance, I would not have had the tools to conduct successful scientific research. I would like to thank my reading committee members, Professors Curt Frank and Thomas Jaramillo for their support and guidance through the dissertation process, as well as my non-reader, Professor Paul McIntyre, and my chairperson, Professor Bruce Clemens. I would like to especially thank Jeannie Lewandowski for her support in matters related to purchasing and her refreshing input in a variety of subjects. Dr. Chuck Hitzman of the Stanford Nanocharacterization Laboratory was instrumental (no pun intended) in teaching me how to use a variety of analytical tools for my research and for providing mentorship.

The Bent Research Group grew from about six people to over 20 throughout my tenure. I would like to thank my early mentor, Xirong Jiang for all her help in Pt ALD and with the ODTS SAMs system. Dr. Jeff King demonstrated a remarkable and in my experience, unparalleled skill at troubleshooting reactor design, and I would like to thank him for teaching me some of those associated skills. Paul Loscutoff, Jessica Kachian and Pendar Ardalan were also Bent Group members early in my studies who I would like to thank for their patience and guidance. Jonathan Bakke, who was in the same cohort as me, was also a wizard of reactor design, and I would to thank him for his insight and assistance. The next batch of Bent Group colleagues including Nid Methaapanon, who was my second rotation student, and Tom Brennan have been very supportive and helpful.

After returning from a leave of absence, I found that the Bent Group had grown significantly with expertise from a variety of backgrounds. I would like to thank Katie Pickrahn, who picked up where Jonathan Bakke left off in ALD reactor design wizardry, Steve Herron for his continued support, intellectual curiosity and support in all matters related to more sophisticated chemical thinking, Art Wangperawong for his mechanical and electrical engineering perspectives and Katie Roelofs for help with understanding the crystal structure of zinc tin oxide. I owe a tremendous amount of gratitude to Dr. Carl Hägglund, whom I affectionately call "my post-doc" for building the reactor for the tin oxide and zinc tin oxide ALD studies, teaching me about optical properties through means of spectroscopic ellipsometry and for having a very positive and practical approach to troubleshooting. While all the Bent Research Group post doctoral associates were extremely supportive and helpful, including Dr. Han-Bo-Ram Lee,

with his help with Pt ALD and PMAM removal studies, Dr. Jukka Tanskanen, with his fundamental approach to tin oxide and zinc tin oxide ALD growth and Dr. Scott Geyer, with his help with GIXRD, Carl really stands out as a superstar.

Apart from the Bent Research Group, other organizations were elemental in supporting my graduate studies by building my self-confidence, developing important skills and serving as a constructive outlet when research proved particularly stressful.. I would like to thank the Stanford Physical Education Department and Stanford Aerobics and Yoga for training me and allowing me to teach various modalities of group fitness. Personal fitness is of great importance to me and through these organizations, I was able to realize and develop my fitness education skills. During my first year, the Black Graduate Student Association and wonderful mentors helped me navigate the sometimes isolating and confusing world of graduate studies. Dean Noe Lozano and the programs from the Office of the Vice Provost for Graduate Education provided me with very useful interpersonal and self-management skills. The Community Associate Program , through the Graduate Life Office, enabled me to interact with a variety of graduate students and learn how to provide them with a supportive and friendly living environment while leading a book club and teaching knitting and crochet, hobbies that are very dear to me.

In my personal life, I would like to thank my parents and brother for their loving support for my educational aspirations. My family immigrated from Jamaica during the late 1980s and 1990s in order to work hard in the pursuit of a brighter future. For leaving everything and everyone they knew behind in Jamaica for the promising, yet uncertain opportunities of the United States, I am eternally grateful. Alvin Yates, my

best friend and fiancé, deserves all the gratitude and love in the world for standing by me and providing guidance and support during my education. I do not know where I would be without him, and I am always in awe of this wonderful man. Finally, I would like to thank Xiwen "Sharon" Zheng, my oldest friend, for her support as we both went through our "quarter life crises" together.

Table of Contents

Table of Contents xii
List of Figures xv
List of Tables xxiii
Chapter 1. Introduction and Background 1
1.1. Background and Motivation 1
1.2. Atomic Layer Deposition (ALD) 3
1.2.1. ALD Growth Characteristics 4
1.2.2. ALD Temperature Window 5
1.2.3. ALD Precursor Considerations 6
1.2.4. Limitations and Recent Advances in ALD 7
1.2.5. ALD Precursor Chemistries and Process Overview 8
1.3. Surface Passivation and Area-Selective ALD 14
1.3.1. Octadecyltrichlorosilane Self-Assembled Monolayers (SAMs) 16
1.3.2. Polymer resists 20
1.4. ALD of TCOs 21
1.4.1. Overview of TCOs 21
1.4.2. Use of ALD to Control Composition of Ternary Metal Oxides 22
1.5. Organization of Thesis 23
1.6. Collaborations 24
Chapter 2. Analytical Methods 26
2.1. Atomic Layer Deposition Reactors 26
2.2. Ellipsometry 28
2.2.1. Introduction 28
2.2.2. Theory 29
2.2.3. Equipment 31
2.3. Water Contact Angle Goniometry 34
2.3.1. Introduction 34
2.3.2. Theory 34
2.3.3. Equipment 35

2.4. Scanning Electron Microscopy (SEM) 36
2.4.1. Background and Basic Principles 36
2.4.2. History 37
2.4.3. Equipment 38
2.5. X-ray Photoelectron Spectroscopy 40
2.5.1. Introduction 40
2.5.2. Theory 41
2.5.3. Equipment 44
2.6. Auger Electron Spectroscopy (AES) 45
2.6.1. Background 45
2.6.2. Theory 45
2.6.3. Equipment 49
2.7. Ultraviolet-Visible(UV-Vis) Spectroscopy 50
2.7.1. Background 50
2.7.2. Theory 51
2.7.3. Equipment 54
2.8. X-ray Diffraction/Diffractometry (XRD) 54
2.8.1. Background 54
2.8.2. Theory 55
2.8.3. Equipment 57
2.9. Inductively Coupled Plasma-Optical Emission Spectroscopy (ICP-OES) 59
2.9.1. Background and Equipment 59
Chapter 3. Area-Selective Atomic Layer Deposition by Microcontact Printing with a Water-Soluble Polymer 60
3.1. Introduction 60
3.2. Experimental Methods 64
3.3. Results and Discussion 67
3.3.1. PMAM Formation by Spin Coating 67
3.3.2. Patterning of PMAM by μCP 71
3.3.3. Removal of PMAM 74
3.4. Conclusions 78

Chapter 4. Nucleation-Controlled Growth of Nanoparticles by Atomic Layer Deposition 79
4.1. Introduction 79
4.2. Experimental Methods 82
4.3. Results and Discussion 84
4.4. Conclusions 92
Chapter 5. Tin Oxide Atomic Layer Deposition from Tetrakis(dimethylamino)tin and Water 93
5. 1. Introduction 94
5.2. Experimental Details 96
5.3. Results and Discussion 99
5.3.1. SnO_x ALD Growth Characterization 99
5.3.2. SnO_x Film Characterization and Properties 104
5.4. Conclusions 111
Chapter 6. Thin Film Characterization of Zinc Tin Oxide Deposited by Thermal Atomic Layer Deposition 112
6.1. Introduction 113
6.2. Experimental Methods 116
6.3. Results and Analysis 118
6.3.1. ZTO Properties as a Function of Bilayer Period 118
6.3.2. ZTO Properties as a Function of Composition 124
6.4. Conclusions 136
Chapter 7. Conclusions 138
7.1. General Conclusions 138
7.2. Future Experimental Directions for ALD of Conductive Materials 139
7.2.1. Area-Selective ALD (AS-ALD) 139
7.2.2. Future Studies for ZTO ALD Film Characterization 140
7.3. Outlook for ALD Scale-up for Industrial Applications 141
7.3.1. ALD in the Semiconductor Industry 142
7.3.2. ALD in the Photovoltaics (PV) Industry 142
Chapter 8. References 145

List of Figures

Figure 1.1. A schematic of a sample ALD process comprised of gas-phase half reactions divided into timed pulses of reactant and counter-reactant separated by inert purges. This process takes place under vacuum and typically with external heating. 4

Figure 1.2. Temperature window for sample ALD process comprised of three temperature components: (1) low, (2) ALD and (3) high., adapted from *Handbook of Thin Film Materials* [9]. 5

Figure 1.3. Schematic of photolithographic process summarized in the following steps: 1) application of photoresist to Si substrate, 2) exposure to ultraviolet light through patterned photomask, 3) development of photoresist with removal of unprotected material, 4) processing (etching, deposition, oxidation, diffusion, etc.) and 5) stripping of remaining photoresist. 15

Figure 1.4. Schematic of surface deactivation and AS-ALD of a film [40]. 16

Figure 1.5. Schematic of a typical alkyl self-assembling surfactant molecules on a substrate comprised of 1) the surfactant tail group, (2) the alkyl or derivatized-alkyl chain and (3) the surface active head group. 17

Figure 1.6. Schematic of microcontact printing (μCP) processing consisting of : (1) lithographic forming of master, (2) casting of an oppositely patterned stamp, (3) dipping of stamp into ink solution, (4) evaporating of excess ink, (5) contacting of the stamp with the substrate under the application of pressure and (6) lifting off and curing of the pattern. 19

Figure 2.1. Photograph of home-built hot wall reactor capable of holding a four inch wafer. Shower-head design of precursor inlet along with flow of nitrogen carrier gas enables uniform radial distribution of deposited material to the substrate. 27

Figure 2.2. Schematic of the custom-built, hot-walled ALD reactor. The main part was a cylindrical tube, heated externally. The tube was fitted with inlets for nitrogen carrier gas and precursors close to its upstream end. A sample stage with in-situ temperature monitoring is positioned near the center of the tube. A separately pumped mass spectrometer was used to analyze gas sampled downstream the stage by means of a needle valve. The finite element method was used to model the carrier gas flow and diffusion through the tube, indicating even distribution of the precursors. The flow profile in the mid section of the tube is shown..... 28

Figure 2.3. Picture of the Woollam α-SE Variable Angle Spectroscopic Ellipsometer (VASE) with support computer and pump. 32

Figure 2.4. Schematic of basic components of an ellipsometer including a light source, polarizer, compensator, analyzer and detector. 33

Figure 2.5. A schematic of the contact angle, θc, where the solid-liquid (γ_{SL}) and liquid-gas (γ_{LG}) interfaces meet. Also represented is the solid-gas interface (γ_{SG}). 34

Figure 2.6. The FTA 2000 Dynamic Contact Angle Analyzer used to determine static water contact angles of ODTS SAMs for this thesis. The system is comprised of micro-motor, a liquid droplet delivery system, a CCD camera and an analysis program. 36

Figure 2.7. Schematic of primary electron beam interaction with a solid surface to generate different species including secondary electrons (SE), backscattered electrons (BSE), Auger electrons, transmitted electrons and characteristic x-rays. Schematic adapted from *Surface Science Foundations of Catalysis and Nanoscience* [154]. 37

Figure 2.8. Schematic of major SEM components including electron source, electron guns, lens, sample chamber, secondary electron collector and detector system and associated pumps. Adapted from *An Introduction to Electron Microscopy* [161]. 38

Figure 2.9. A schematic of the photoelectric effect. Incident x-ray photons are able to excite and eject a core level electron if its energy is greater than the binding energy of the electron. 40

Figure 2.10. Schematic of Auger transition of three core levels K, L1 and L2. An electron is emitted and another relaxes into its place resulting in the simultaneous ejection of another core-level electron [155]. 47

Figure 2.11. Energy levels for a KLV Auger transition referenced with respect to the Fermi level (E_F) and showing the influence of the spectrometer work function Φsp. Adapted from Surface Science: Foundations of Catalysis and Nanoscience [155]. 48

Figure 2.12. Photograph of the PHI 700 Scanning Auger Nanoprobe located in the Stanford Nanocharacterization Laboratory. 50

Figure 2.13. A multiplicity of electronic transitions from ground to excited states. Only vibrational states are represented as rotational levels are very closely spaced. . 51

Figure 2.14. Schematic of Bragg diffraction in which two identical x-rays of wavelength λ strike a crystalline solid and are scattered from two different atoms. The path length of the lower x-ray beam is $2d\sin\theta$. Constructive interference takes place when the path length is equal to an integer multiple n of the wavelength of radiation given by Bragg's law $n\lambda = 2d\sin\theta$. 56

Figure 2.15. Picture of goniometer, x-ray detectors and sample holder of the X'Pert 2 PANalytical Materials Research Diffractometer. 58

Figure 2.16. ICP-OES process schematic in which bulk material is dissolved in aqueous solution and then sprayed into a plasma so energetic that ionization takes place. A monochromator separates specific wavelengths of interest and a detector measures the intensity of the emitted light at element-specific electromagnetic wavelengths. 59

Figure 3.1. PMAM monomer. 63

Figure 3.2. PMAM film thicknesses as a function of PMAM concentration. (Error bars on spin-coated samples represent one standard deviation over five locations per sample. For 1 wt %, five samples were separately fabricated and its error bar is representative of sample-to-sample variation.) 68

Figure 3.3. Pt atomic percentage from XPS as a function of PMAM thickness following spin coating on a Si substrate. (Error bars on each sample represent one standard deviation over three location per sample.) 69

Figure 3.4. PMAM film thicknesses as a function of PMAM concentration from µCP. 71

Figure 3.5. SEM images of [(a) and (b) 500 x 500 PDMS stamps and [(c) and (d)] 2–4 x 2–4 µm stamps before and after 100 cycles of Pt ALD. 73

Figure 3.6. SEM and scanning AES Pt elemental map of 2–4 x 2–4 µm stamps following 100 cycles of Pt. 74

Figure 3.7. (a) PMAM film thicknesses measured by ellipsometry and (b) IR spectra during removal of PMAM as a function of dipping time in water. (Error bars represent one standard deviation over five locations per sample.) 76

Figure 3.8. XPS spectra in (a) Pt and (b) N core levels obtained from PMAM-coated, uncoated and reactivated samples after Pt ALD for 400 cycles. The reactivated samples was prepared by dipping a PMAM-coated sample in water for 3 h. 77

Figure 4.1. Schematic illustration of the hypothesized SAM-directed growth of Pt NPs with control over aerial density and particle size. (a) Behavior of the SAM with increasing dip time. (b) Decrease in NP aerial density with increasing SAM dip time. (c) Increase in NP size with increasing number of ALD cycles for a constant SAM template. 82

Figure 4.2. SEM images of Pt nanoparticles (NPs) grown by ALD for a variety of ODTS dip times and number of ALD cycles with 200 nm scale bar. 85

Figure 4.3. Mean Pt NP diameter and aerial density versus dip time of ODTS, for (a) 50 cycles and (b) 100 cycles of Pt ALD following the ODTS treatment. The NP diameter and NP density were measured from the software analysis by using SEM images. All corresponding SEM images can be found in Figure 4.2. 86

Figure 4.4. Pt NP diameter, density and atomic percent with changing number of ALD cycles on surfaces coated with ODTS for various dip times, (a) 0, (b) 2, (c) 4, (d) 8 and (e) 12 h. The NP diameter and NP density were measured from the software analysis by using SEM images (Figure 2). Pt atomic percent was obtained using XPS quantification. The error bars on the diameter data makers indicate the distribution of particle sizes. 88

Figure 5.1. Schematic of the custom-built, hot-wall ALD reactor. The main part is a cylindrical tube, heated externally. The tube is fitted with inlets for N_2 carrier gas and precursors close to its upstream end. A sample stage with in-situ temperature monitoring is positioned near the center of the tube. A separately pumped mass spectrometer is used to analyze gas sampled downstream the stage by means of a needle valve. The calculated carrier gas flow and diffusion through the tube indicate even distribution of the gas. The flow profile in the mid section of the tube is shown. 97

Figure 5.2. SnO_x growth rate determined by VASE, as a function of (a) and (c) TDMASn pulse length *x* for timing sequences of *x*:30:2:30 s and (b) and (d) H_2O pulse length *y* for timing sequences of 1:30:*y*:30 s. The substrate was Si(100) at 150 ºC for (a) and (b) and at 30 ºC for (c) and (d)..... 101

Figure 5.3. SnO_x film thickness as a function of number of ALD cycles yielding a growth rate of 0.70 Å/cycle. Thicknesses were obtained using VASE for films deposited on Si(100) at 150 ºC with a time sequence of 1:30:2:30. 102

Figure 5.4. SnO_x ALD growth rate as a function of temperature determined using VASE for films deposited on Si(100) for 200 cycles with timing sequence 1:30:2:30 s 103

Figure 5.5. SnO_x growth rate at 30 ºC determined by VASE as a function of nitrogen purge time following (a) TDMASn pulse length and (b) H_2O pulse length for timing sequences of $1:t_2:2:t_4$ s. time dependence . The substrate was Si(100). 104

Figure 5.6. X-ray photoelectron spectroscopy survey scan of 46 nm SnO_x film deposited on Si(100) at 150 ºC after Ar^+ sputtering. 105

Figure 5.7. Atomic concentration of carbon as a function of deposition temperature of SnO_x deposited on Si(100) at 150 ºC before and after Ar^+ sputtering 106

Figure 5.8. XRD patterns for a 130 nm film of SnO_x deposited on Si(100) at 150 ºC as function of annealing temperature under flow of N_2, as-deposited (black) and 600 ºC anneal (red). 107

Figure 5.9. SEM images of a 46 nm SnO_x film deposited on Si(100) at 150 ºC (a) as-deposited; (b) post-500 ºC anneal; (c) post-600 ºC anneal; (d) cross-section of post-600 ºC anneal. 108

Figure 5.10. SnO_x film refractive index and (b) extinction coefficient extracted from spectroscopic ellipsometry, as a function of the substrate temperature for films deposited using 200 ALD cycles. The inset in (b) illustrates plots of $(\alpha h\nu)^{1/2}$ with linear fits (dashed lines) to the approximately linear portion of the curve. Bandgaps are estimated from the intersection of the linear fits with $(\alpha h\nu)^{1/2} = 0$. (c) Estimated bandgaps as a function of temperature, after 200 cycles of ALD. (d) Bandgaps as a function of film thickness for varying number of ALD cycles and a substrate temperature fixed to 150 °C. The dashed lines in (c-d) represents quadratic fits to the data. 109

Figure 6.1. Schematic of ZTO super cycle formalism visualized as a lamellar stack of ALD cycles of constituent binary oxides. One super cycle is defined by a certain number of SnO_x cycles, *t*, and ZnO cycles, *z*. 120

Figure 6.2. Growth rate versus bilayer period based, Λ, on experimentally-determined values from VASE and an analytical method (Equation 5.5). 121

Figure 6.3. Tin composition fraction versus bilayer period based, Λ, on experimentally-determined values from ICP-OES (black circles)and an analytical model (red dashed line, Equation 5.5). 122

Figure 6.4. X-ray photoelectron spectroscopy survey scan of ZTO deposited on Si(100) at 150 ºC after Ar^+ sputtering for 12 s for Λ = 400 and c_{Sn} = 0.38 from ICP-OES. 123

Figure 6.5. Plan-view, high-resolution SEM images for with bilayer period, Λ, overlaid under the conditions described in Table 6.1. 123

Figure 6.6. Film growth characteristics determined by VASE (red squares) and an analytical model described by Equation 5 (blue dashed line) as a function of tin cycle fraction. For reference, the growth rates linearly interpolated from the binary ALD processes. 126

Figure 6.7. Composition of ZTO determined by ICP-OES, using an analytical model for the growth rate described by Equation 6.6 and linearly interpolated fractional Sn composition as a function of Sn/(Sn+Zn) cycle fraction, f_{Sn}. Number of ZTO ALD cycles, A= 600, number of super cycles, S = 100 and bilayer period, Λ = 6. Films were deposited on Si(100) at 150 ºC and each data point is an average over two data sets. 128

Figure 6.8. Grazing incidence x-ray diffraction (GIXRD) show patterns for a range of ZTO compositions sampled by Sn/(Sn+Zn) cycle fraction, f_{Sn}. Films of ZTO were deposited at 150º C on Si (100). 130

Figure 6.9. High resolution SEM images of ZTO on Si(100) with bilayer period, Λ=6, for A = 600 ZTO ALD cycles as a function of increasing percentages of tin from ICP-OES. The scale bar is 500 nm. 131

Figure 6.10. High resolution SEM images of ZTO on Si(100) with bilayer period, Λ=6 for (a) A = 300 ZTO ALD cycles for f_{Sn} = 0.17 and (b) A = 1200 ZTO ALD cycles for f_{Sn} = 0.83. The scale bar is 500 nm. 132

Figure 6.11. Spectroscopic ellipsometry results for (a) refractive index and (b) extinction coefficient vs. wavelength for ZTO on Si(100) over a range of tin cycle fractions (indicated in the color-coded legend in the upper right hand corner of each plot). For comparison, optical extinction vs. wavelength from measurements of the ZTO transmittance on fused silica is also included in (c). 134

Figure 6.12. VASE multi-sample analyses of bandgaps for a range of ZTO cycle fractions. The bandgaps are found by extrapolating linear portions of the function $(\alpha h\nu)^x$ to zero. In this expression, $h\nu$ is the photon energy and α the absorption coefficient ($\alpha = 4\pi k/\lambda$ with k the extinction coefficient of the material, as determined by VASE). For the direct type bandgap fits in (a), the exponent x = 2, while for the indirect or amorphous type bandgap in (b), x = 0.5. The tin cycle fractions are indicated in the legends. The results are summarized versus the Sn cycle fraction, f_{Sn}, in (c), and versus the composition c_{Sn}, in (d). 135

List of Tables

Table 1.1. Description of regions comprising ALD growth regimes as a function of temperature. 6

Table 1.2. Characteristics for ALD precursors and rationale for importance [9]..... 7

Table 1.3. Crystal phase of ZTO as a function of anneal temperature 13

Table 1.4. Summary of ZTO ALD history as a function of publication date, precursor chemistry and application. 13

Table 2.1. Value of transition type, n and description of forbidden, allowed and indirect or direct transitions. 54

Table 2.2. Interplanar spacings (d_{hkl}) for the seven crystal systems [179, 180]. 57

Table 6.1. Summary of experiments for varying bilayer period Λ and total number of super cycles, S and the growth rate, determined by VASE. Constants were Sn/(Sn+Zn) cycle fraction, f_{Sn} = 0.75, and A = 800 total number of ZTO ALD cycles comprised of 200 ZnO ALD cycles and 600 SnO_x total ALD cycles. Tin composition fractions, c_{Sn}, were determined by ICP-OES. Films were deposited at 150 ºC on Si(100) and on fused silica quartz. 121

Table 6.2. Summary of ZTO experiments as a function of Sn cycle fraction across a duplicate of samples. Systematic variation of tin cycle fractions, f_{Sn} =Sn/(Sn+Zn), gave rise to changes in Sn composition fraction, c_{Sn}, determined by ICP-OES and influenced growth rate, determined by VASE. Constants were total number of ZTO ALD cycles, 600, total number of super cycles, S=100 and degree of lamination, Λ= 6. Films were deposited at 150 ºC on Si(100) and fused-silica quartz. 125

This page is intentionally left blank

Chapter 1. Introduction and Background

1.1. Background and Motivation

The consumer electronics industry and emerging fields related to devices for energy conversion have their origins in the semiconductor industry. The development of integrated circuits represents many years of careful optimization of metal, semiconducting and insulating components required to perform under severe processing and operating conditions. Moore's Law has driven the required performance of the transistors in these devices by predicting the doubling of transistor density every eighteen months [1]. Placing more transistors per chip requires significant reduction in feature length for every generation of metal oxide field-effect transistor (MOSFET).

By the 90 nm generation, the frequency of these MOSFETs approached the GHz range, but the thickness of the SiO_2 gate had decreased sufficiently to cause significant transistor leakage [2]. This 90 nm generation marked the end of the traditional MOSFET scaling era whereby homogeneous scaling of the SiO_2 gate was required to increase device performance. The current era is marked by the use of heterogeneous components in which new device structures and new deposition techniques have been developed to improve device performance and keep pace with Moore's Law [3]. An example of the use of heterogeneous components is Intel's current 22 nm transistor tri-gate design with a high-κ dielectric [4]. Consumer demand for smaller and more powerful mobile electronics continues to increase. Film growth on high-aspect ratio structures at these smaller length scales has become more critical. Therefore,

fundamental research on nanoscale material components of semiconductor devices remains essential to meeting these demands for miniaturization.

This thesis focuses on the nanoscale deposition and characterization of conductive metal and metal oxides that are relevant to integrated circuit fabrication and also have applications in devices for energy conversion. The principles and practices from semiconductor surface science are the foundation of the studies presented in this thesis. The hydroxylated silicon dioxide surface serves the principal substrate for gas-phase vacuum deposition of these conductive materials. An increasingly popular deposition technique, atomic layer deposition (ALD), is the method for growing these films and is refined in the current work to demonstrate spatial and compositional control over the deposited materials. This work helps to better understand how to achieve control over the spacing of expensive catalytic material, which may aid in more economical use of very rare metals and may have consequences in further understanding catalytic processes on a fundamental nanoscale. In Chapters 3 and 4, surface passivation for spatial control of platinum grown via ALD is described, including a self-assembled monolayer (SAM) template used to direct the growth of platinum nanoparticles (Chapter 3) and a polymer resist for area-selective growth of well-defined arrays of platinum thin films (Chapter 4). In subsequent chapters, ALD is used to carefully alloy the earth-abundant, non-toxic and inexpensive transparent conducting oxide (TCO), zinc tin oxide (ZTO), which may be used in thin film solar cells and transistors, light emitting diodes, architectural glasses and flat panel displays.

This chapter serves as an introduction and background for important concepts in the spatial and compositional control of conductive materials via ALD. An

understanding of ALD is central to this thesis, so an extensive treatment of the topic will be presented. Following this overview, specifics of the precursor chemistry for each material deposited will be described. A more specific background for modifications of ALD in the form of area-selective ALD (AS-ALD) and surface passivation to direct the growth of platinum will be examined. The next sections then present an overview of TCOs and describe how ALD can be used to control composition. Following these background sections, the central goals of this work and the organization of the thesis are presented. Finally, because the culmination of this work was made possible by working closely with talented colleagues, this chapter concludes with a section describing these collaborations.

1.2. Atomic Layer Deposition (ALD)

ALD is an increasingly popular method for growing uniform and conformal thin films [5-9]. This vacuum deposition technique is based on alternating gas-surface reactions separated by inert purges allowing for self-limited growth, ideally yielding uniform and conformal films independent of substrate geometry. ALD has been used to deposit a wide range of materials, including metals [10-16], metal oxides [17-21] and metal sulfides [22-25]. As a result, ALD has been applied to different fields, with the following examples: semiconductors [26-28] , photovoltaics [23, 25, 29-31] and the mimicry of biological systems [28, 32-36]. Furthermore, the diversity of ALD systems has also allowed for the area-selective growth of a variety of materials [5-9, 37-45]. Moreover, conformal coverage of three-dimensional substrates is a characteristic feature resulting from the self-limited growth mechanism of ALD [46-52]. The following

section will describe the characteristics of ALD, and how it is used for the selective deposition of materials.

1.2.1. ALD Growth Characteristics

The ALD growth process can be divided into cycles of reactant and counter-reactant pulses separated by inert purges. Each cycle consists of four components which represent timed doses of gaseous species. A sample ALD schematic is presented in Figure 1.1 and consists of (1) pulse of reactant which reacts with certain ligands of the substrate, (2) inert gas purge of excess reactant, (3) pulse of counter-reactant designed to react only with the ligands of the reactant and (4) another inert gas purge to remove excess amounts of the counter-reactant.. The cycle-by-cycle, approximately monolayer-by-monolayer, growth with inert purges to prevent super-saturation allows ALD to be capable of growing ultra-thin films in a self-limited fashion.

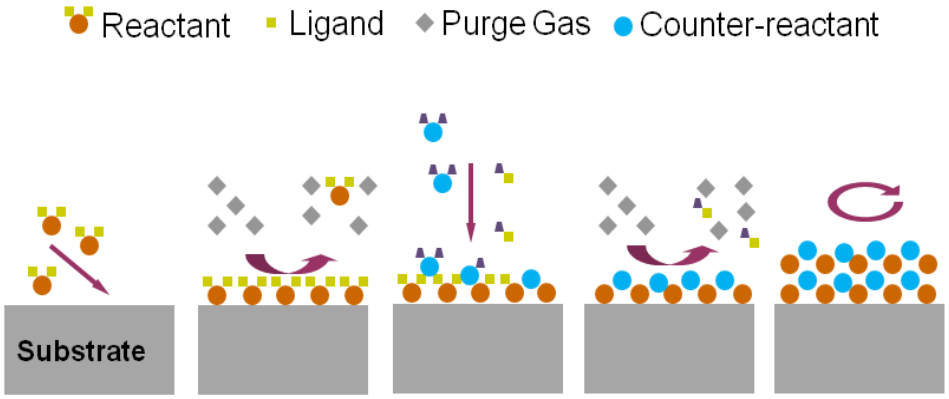


Figure 1.1. A schematic of a sample ALD process comprised of gas-phase half reactions divided into timed pulses of reactant and counter-reactant separated by inert purges. This process takes place under vacuum and typically with external heating.

Precursors from chemical vapor deposition (CVD) have historically motivated the choice of ALD chemistry [9]. Furthermore, characteristics of the surface adsorption

of the precursors drives ALD growth. Therefore, the choice of precursor chemistry is a major design element of ALD systems. A brief introduction to the precursor chemistry of platinum, tin oxide and zinc tin oxide ALD processes will be presented in the next section. Experimental parameters that also give rise to saturated growth include the duration of precursor and inert gas purge dosing, choice of substrate, growth temperature and reactor design.

1.2.2. ALD Temperature Window

A key parameter for designing an ALD system is determining its temperature window. Upper and lower limits of growth temperature will aid in the understanding of deposition kinetics. Figure 1.2 provides a schematic of a typical ALD temperature window adapted from the *Handbook of Thin Film Materials* [9].

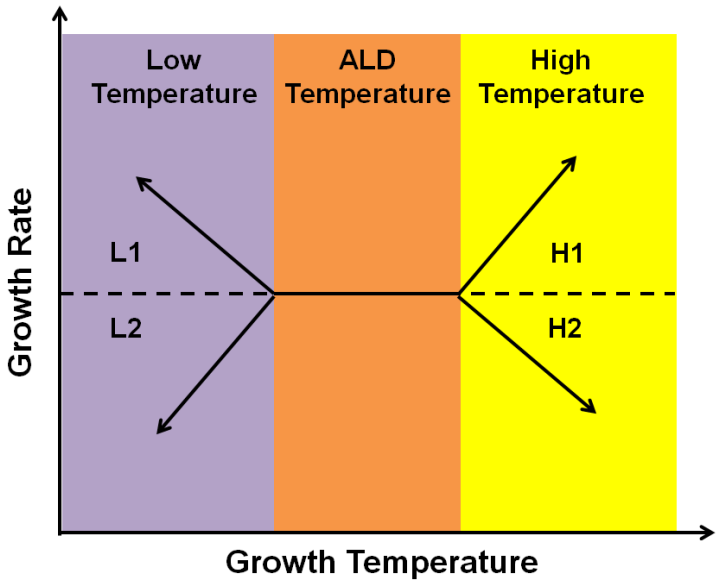


Figure 1.2. Temperature window for sample ALD process comprised of three temperature components: (1) low, (2) ALD and (3) high., adapted from *Handbook of Thin Film Materials* [9].

The component regions of Figure 1.2 are explained in Table 1.1. When the growth rate is constant as a function of temperature (the center region in Figure 1.2), an ALD temperature window may be defined. When the growth rate increases as a function of decreasing temperature, region L1, precursor condensation occurs. Another reason for increased growth rate, this time at higher temperatures, region H1, the precursor undergoes thermal decomposition. For decreased growth rate at lower temperatures, region L2, there is an activation energy limitation due to incomplete reactions. In region L3, desorption or loss of species surfaces is responsible for decreased growth rate at higher temperatures.

Table 1.1. Description of regions comprising ALD growth regimes as a function of temperature.

Region	Description
L1	Precursor condensation
L2	Activation energy limitation
H1	Precursor thermal decomposition
H2	Precursor surface desorption

1.2.3. ALD Precursor Considerations

As previously mentioned, precursor selection is an important component in the design of an ALD process. Table 1.2, adapted from the *Handbook of Thin Film Materials,* provides a list of ALD precursor characteristics and provides justification for their importance [9].

Table 1.2. Characteristics for ALD precursors and rationale for importance [9].

ALD precursor characteristic	Importance
Volatility	Efficiency of precursor transport
Thermal stability	Prevention of self-decomposition thus maintaining self-limiting nature of process
High reactivity and complete reactions	Fast completion of surface reaction, self-limiting mechanism and short cycle times
No etching of film or substrate materials	Avoidance of competing reactions
Volatile byproducts	Avoidance of reactor corrosion and film impurities
No dissolution into the film or substrate	Maintenance of self-limited growth

To meet the demands of a specific system and in many cases to take into account environmental, health, safety and economic considerations, ingenious organometallic chemistries have been and continue to be used for the synthesis of new precursors. The development of tin oxide precursors from the harsh halide chemistries of $SnCl_4$ and SnI_4 [53-55], to the non-halogenated alternatives such as $Sn(NCH_3)_2)_4$ (TDMA)[56, 57] and a cyclic tin amide (1,3-bis(1,1-dimethylethyl)-4,5-dimethy,(4*R*,5*R*)-1,3,2-diazastannolodin-2-ylidene) [58, 59], is an example of these efforts.

1.2.4. Limitations and Recent Advances in ALD

While ALD is a powerful deposition technique, a major disadvantage is the slow deposition rate due to the nature of sub-monolayer or near single-monolayer growth, typically on the order of ~1 Ångstrom per cycle or hundredths of nanometers each second. The design of new precursors, the use of plasma-enhanced chemistries, obtaining a better understanding of existing processes using in-situ methods, modified reactor design and subsequent redefinition of temperature windows and precursor pulse times are just some potential approaches to enhancing growth rate while reducing

reaction time. Two emerging techniques for improving throughput have been through batch and spatial ALD. In batch ALD, a temporal process, multiple substrates are processed at a single time. Substrates pass under reaction zones and are exposed to precursors separated by inert gas shields [60]. Another means of improving the time efficiency of ALD may be through spatially-separated ALD precursors, a concept first patented by Suntola in the 1970s, which removes the need for inert purges [61]. Batch and spatial ALD may further the integration of ALD into industrial applications especially in photovoltaic applications [62-64].

1.2.5. ALD Precursor Chemistries and Process Overview

This section provides an overview of the conductive materials and their respective ALD processes. The metal of interest in the present work was platinum and an ALD process from the literature was adapted for the selective deposition of this material. For metal oxides, a tin oxide process was developed and careful alloying of this material with zinc oxide was used to control the composition of zinc tin oxide. The precursor chemistries of these systems are described in the next sections.

1.2.5.1. Platinum Overview and ALD Precursor Chemistry

Platinum is an outstanding catalyst whose properties are actively being studied and refined for use as catalytic converters in automobiles [65], in common industrial processes for polymerization [66], in fuel cells [67, 68], as a component of chemotherapeutic drugs [69] and in the biomimicry of photosynthesis for water-splitting [36]. Platinum is one of the rarest elements accounting for a crustal abundance of ~1 ppb [70]. Furthermore, demand for Pt from two major industries is on the rise: (1)

the automotive industry, which accounts for about 60% of demand and (2) jewelry-making, which accounts for about 25 %. This scarcity coupled with high demand results in increasing costs for this metal [65]. According to the 2012 U.S. Geological Survey Mineral and Commodity Summaries, the annual average price of platinum per troy ounce (t oz) increased from 2007 ($1308/t oz) to 2011 ($1720 /t oz), by over 31 % [71]. To minimize usage of the material and to take advantage of potentially improved catalytic properties on the nanoscale, ALD has been used to selectively deposit Pt. Placing an expensive metal only where needed may not only reduce costs, but may also enhance flexibility for process design.

The details of the Pt ALD process are described in Chapter 3 and Chapter 4. This ALD process is adapted from the work of Aaltonen et al. [15]. The precursors are (methylcyclopentadienyl)trimethylplatinum $(MeCp)PtMe_3$ and an oxidant source, which may be O_2, O_3 or air. For the work presented in this thesis, air was used as the counter-reactant.

While many details of the growth kinetics of the Pt ALD process remain to be discovered, mass spectroscopy has been used to show that oxidation takes place both during the oxidant pulse and also during the $(MeCp)PtMe_3$ surface adsorption [72]. Gas phase infrared spectroscopy studies by Kessels et al. were used to refine the chemical equations that Aaltonen et al. predicted for the Pt ALD process. Equations 1.1 and 1.2 show the surface reactions as suggested by Kessels et al. [73]:

$$2(MeCp)PtMe_3\,(g) + 3O(ads) \rightarrow 2(MeCp)PtMe_2(ads) + CH_4\,(g) + CO_2\,(g) + H_2O\,(g) \quad (1.1)$$

$$2(MeCp)PtMe_2(ads) + 24O_2\,(g) \xrightarrow{Pt} 2Pt(s) + 3\ O\ ads) + 16CO_2(g) + 13H_2O(g) \quad (1.2)$$

Of note, is that the platinum itself acts as a catalyst for the dissociative chemisorption of O_2. In sum, Kessels et al. suggest that the saturation of chemisorbed oxygen atoms drives this Pt ALD mechanism [73].

1.2.5.2. Tin Oxide (SnO_x) Overview and ALD Precursor Chemistry

Tin oxide, SnO_x, $1 \leq x \leq 2$, is an n-type semiconductor with excellent optical, electrical and chemical properties [1-6]. These attractive material properties have enabled the application of SnO_x to many fields including gas sensing [7-10], surface coatings for functional glasses [11-13], field effect transistors [14, 15], catalysis [16-18] and transparent conducting oxides in photovoltaics and flat panel displays [19-23]. When used as a dopant in indium oxide, tin oxide enhances electrical conductivity [24]. In parallel with its large number of applications, many techniques exist for thin film deposition of SnO_x. Some of these processes include chemical vapor deposition (CVD) [25-29], spray-pyrolysis [30, 31], sputtering [32] and atomic layer deposition (ALD) [33-45].

The first SnO_x ALD processes were developed in the 1990s [53, 74, 75]. As with many other ALD systems, the precursors were first adapted from existing CVD processes [53, 75]. Depending on growth temperature, some of these films had the advantage of being crystalline as deposited, but yielded corrosive and equipment-damaging byproducts due to the use of halogenated precursors [53-55]. Elam et al. were the first to publish on the development of a SnO_2 ALD process that used non-halogenated precursors [76] with further developments by Heo et al.[58, 59]. The SnO_x ALD process described in this thesis builds upon Elam's choice of tin precursor, tetrakis(dimethylaminotin) (TDMASn) and fully characterizes the system with use of water as the counter-reactant.

1.2.5.3. Zinc Tin Oxide (ZTO) Overview and History of ALD Process

Impurity-doped or alloyed zinc oxides may serve as alternatives to existing transparent conducting oxides (TCOs) or buffer layers for solar cells. Zinc oxides alloyed or doped with aluminum (AZO) and gallium (GZO) are examples of ITO TCO alternatives [1, 11-13]. While AZO and GZO exhibit attractive properties as inexpensive indium-free alternatives, other options such as zinc tin oxide (ZTO) are also being studied as an inexpensive indium-free TCO [1, 10, 14-22]. Unfortunately, a comprehensive review of the literature suggests little agreement among various structural, optical and electrical properties, motivating a more detailed characterization of this material.

In spite of uncertainties about ZTO, there is some agreement on thermodynamically stable crystal structures of this material. It has been observed that ZTO has two possible stoichiometries that correspond to thermodynamically stable structures. One is zinc methastannate $ZnSnO_3$. This form has two crystalline polymorphs: (1) a face-centered perovskite [77] and an ilmenite [78] structure. The other stoichiometry is for zinc orthostannate, Zn_2SnO_4, which possesses cubic spinel structure [79]. Annealing studies from hydrothermal synthesis and sputtering suggest that ZTO transforms to $ZnSnO_3$ from 300-500 ºC and Zn_2SnO_4 for temperatures exceeding 600 ºC [79]. At these high temperatures, obtaining pure Zn_2SnO_4 is difficult, as mixed phases including both forms of ZTO and SnO_2 are formed [79]. This information is summarized in Table 1.3

Table 1.3. Crystal phase of ZTO as a function of anneal temperature

Anneal Temperature (ºC)	Crystal Phase
300-500	$ZnSnO_3$
500-600	Not reported
>600	$ZnSnO_4$, with mixed phases of $ZnSnO_3$ and SnO_2

While sputtering has been the most-studied deposition method for ZTO [80-82], other techniques include hydrothermal synthesis [79], sol-gel spin coating [83-85], chemical vapor deposition [86] and only very recently, atomic layer deposition (ALD) [87-91]. Because the first report of a successful ZTO ALD system was just reported in 2010, the details of ZTO ALD surface chemistry have not yet been reported. Table 1.4 shows a brief history of ZTO ALD precursor chemistries and potential applications. The most popular application is for use in a copper indium gallium sulfur (CIGS) buffer layer [88-91]. For all of these processes, the zinc oxide component employed diethyl zinc (DEZn). The ZTO ALD process developed in this thesis uses tetrakis(dimethylamino)tin, diethyl zinc and water as reactants.

Table 1.4. Summary of ZTO ALD history as a function of publication date, precursor chemistry and application.

Author, Publication Year	Tin Precursor	Oxidant Source
Choi, 2010 [87]	Tetrakis(ethylmethylamino) tin	Oxygen Plasma
Hultqvist et al., 2010 [88]	Tin(IV)-tert-butoxide	Water
Hultqvist et al., 2011 [89]	Tin(IV)-tert-butoxide	Water
Kapilashrami et al., 2012[90]	Tetrakis(dimethylamino)tin	Water
Lindhal et al., 2012 [91]	Tetrakis(dimethylamino)tin	Water

1.3. Surface Passivation and Area-Selective ALD

Since ALD is based on self-saturated surface reactions, it can produce excellent, conformal films even in complex nanostructures. Chemical methods for modifying or passivating a surface provides a growth template for the placement of material only where needed. This selective deposition may assist in reducing cost of expensive components and may motivate design flexibility.

This area-selective deposition has its origins in semiconductor fabrication where devices are built in a top-down fashion consisting of patterning steps that are designed to affect specific areas of the substrate [92]. A series of masking layers are used to selectively define the desired areas on the wafers and block other regions. In this process, called photolithography, a material called photoresist is a light-sensitive material that is processed into a specific pattern on a substrate after being exposed to high energy light [93]. Photoresist is typically a thin polymeric layer, its precursor or a small molecule specifically designed to transfer a circuit pattern to a semiconductor substrate. Following the patterning of the photoresist, specific parts of the substrate are covered and protected by the photoresist. During subsequent processing steps such as deposition, etching, diffusion and oxidation, only the uncovered parts will be affected. Once the desired processing steps are completed, the photoresist is chemically removed. Figure 1.3 presents a schematic of this area-selective process.

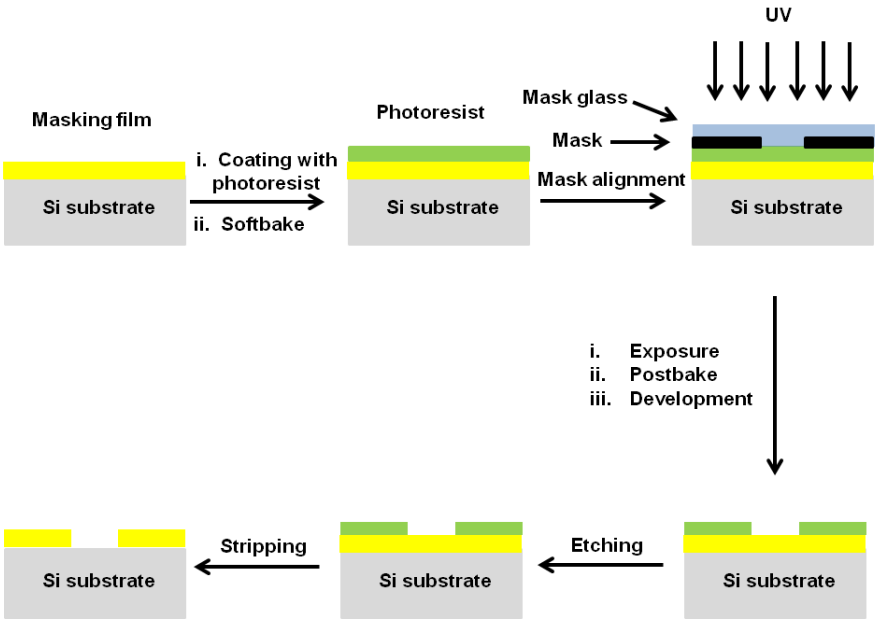


Figure 1.3. Schematic of photolithographic process summarized in the following steps: 1) application of photoresist to Si substrate, 2) exposure to ultraviolet light through patterned photomask, 3) development of photoresist with removal of unprotected material, 4) processing (etching, deposition, oxidation, diffusion, etc.) and 5) stripping of remaining photoresist.

While lithography is the standard area-selective method for circuit fabrication, loss of growth selectivity by nucleation when material grows in undesired regions motivates the need for alternative deposition techniques [94-97]. For example, for a limited number of systems, chemical vapor deposition (CVD) precursor chemistry has been modified so that nucleation occurs preferentially on one surface over another, thereby improving growth selectivity [98, 99]. However, by the very nature of chemical vapor deposition, selectivity is difficult to achieve because the surface and vapor phase reactions are not self-limited. Area-selective atomic layer deposition (AS-ALD) is defined by self-limited, surface adsorption-controlled reactions and therefore may serve as an alternative method to improve growth selectivity. AS-ALD is a bottom-up

patterning method that takes advantage of the self-saturated gas-surface reaction properties of ALD. Figure 1.4 presents a simple schematic of this process [39].

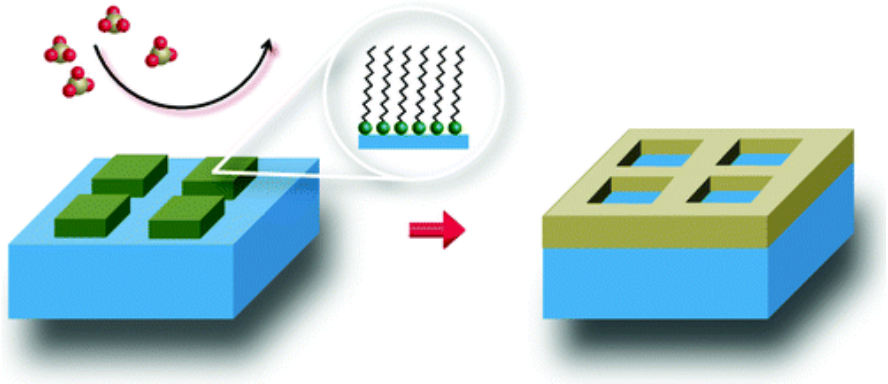


Figure 1.4. Schematic of surface deactivation and AS-ALD of a film [40].

Modification of the substrate properties enables deposition of materials only where needed in the additive process of AS-ALD, unlike in conventional lithography, which is subtractive [100]. Surface modification can be achieved by different approaches, including self-assembled monolayers (SAMs) and polymers. SAMs and polymer resists are described in subsequent sections for use in AS-ALD.

1.3.1. Octadecyltrichlorosilane Self-Assembled Monolayers (SAMs)

To achieve substrate modification for AS-ALD, self-assembled monolayers (SAMs) have been most commonly employed. Self-assembled monolayers (SAMs) are organic films that form spontaneously on solid surfaces into relatively ordered domains [101]. The phenomenon of self assembly allows for tunability of desired materials with control over the components of a SAM molecule. In fact, a review of the SAMs literature has shown that they can modify the material and electrical properties of a variety of surfaces [101].

The ability of SAMs to chemically modify surfaces lie in the properties of its three major components: (1) functional tail group, (2) alkyl or derivatized-alkyl chain and (3) head group. Figure 1.5 shows a schematic of a typical self-assembling molecule.

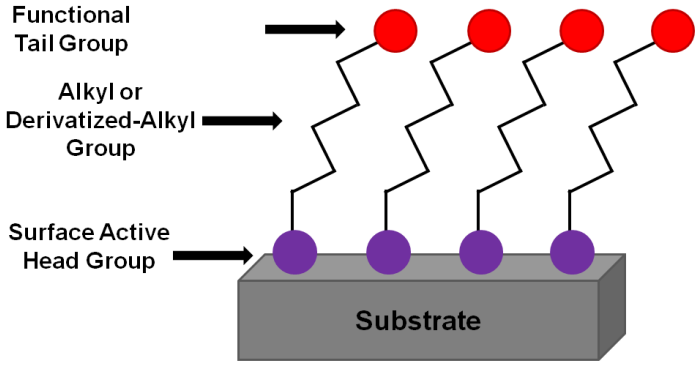


Figure 1.5. Schematic of a typical alkyl self-assembling surfactant molecules on a substrate comprised of 1) the surfactant tail group, (2) the alkyl or derivatized-alkyl chain and (3) the surface active head group.

If the head group of the SAM is chemically active toward the substrate, then a strong interaction will result in chemisorption and the formation of a strong chemical bond. This reaction is exothermic and is kinetically favorable. Covalent bonds such as Si-O and S-Au are common SAM head group-substrate bonds [101]. The degree to which the SAMs order themselves depends on the intermolecular van der Waal forces between tail groups [102]. These tail groups order themselves to achieve a high degree of van der Waal forces thus decreasing the free energy of the organic layer. As a result of these forces, these small molecules are able to achieve two-dimensional short-range order. The kinetics of adsorption, temperature of the SAM precursor solution and the identities of the substrate, head and tail groups are among the factors that may affect the quality of the organic layer. In a well-controlled system with sufficient time for complete surface reactions it is expected that a uniform organic monolayer will be formed; however, in some cases, defects may exist. In Chapter 4, the density of these

SAM defects is controlled by immersion time in precursor solution and used to direct the growth of platinum nanoparticles via ALD.

As previously mentioned, by coating the surface through a self-assembly process, SAMs change the surface properties according to the nature of their tail group [29, 100]. Various SAM molecules, such as octadecyltrichlorosilane (ODTS) [103-112], tridecafluoro-1,1,2,2-tetrahydrooctyltrichlorosilane (FOTS) [107, 110, 111], octadecyltrimethoxysilane [107, 113] and 1-octadecene [106, 110, 114], have been used in AS-ALD. In this thesis, ODTS was chosen to be the SAM of interest because of its optimal growth on the SiO_2 surface and its demonstrated performance in acting as a resist for AS-ALD [38, 115-117].

In addition, the patterning of SAM molecules is important for the AS-ALD process, since the patterns of surface properties induced by the SAM coating are directly transferred into the final patterns of the deposited film. Soft lithography [109, 111, 112], photolithography [118, 119], and nanotemplating [104, 105] have each been investigated for the patterning step in AS-ALD. Among these patterning methods, the soft lithography process of microcontact printing (μCP) has been intensively studied for AS-ALD because it is an easy and effective way to make a pattern without the need for expensive tools. Because elastomeric stamps (typically made of polydimethylsiloxane (PDMS)) are used, the SAM coating can be applied to curved surfaces as well as planar ones [120, 121]. Figure 1.6 summarizes key steps in μCP: (1) a patterned master is first made using lithographic methods, (2) an oppositely patterned polydimethylsiloxane (PDMS) stamp is made from the master, (3) the stamp is dipped into an ink solution (4)

excess ink is evaporated, (5) the stamp is applied with pressure onto the substrate and (6) the printed substrate is cured by heating.

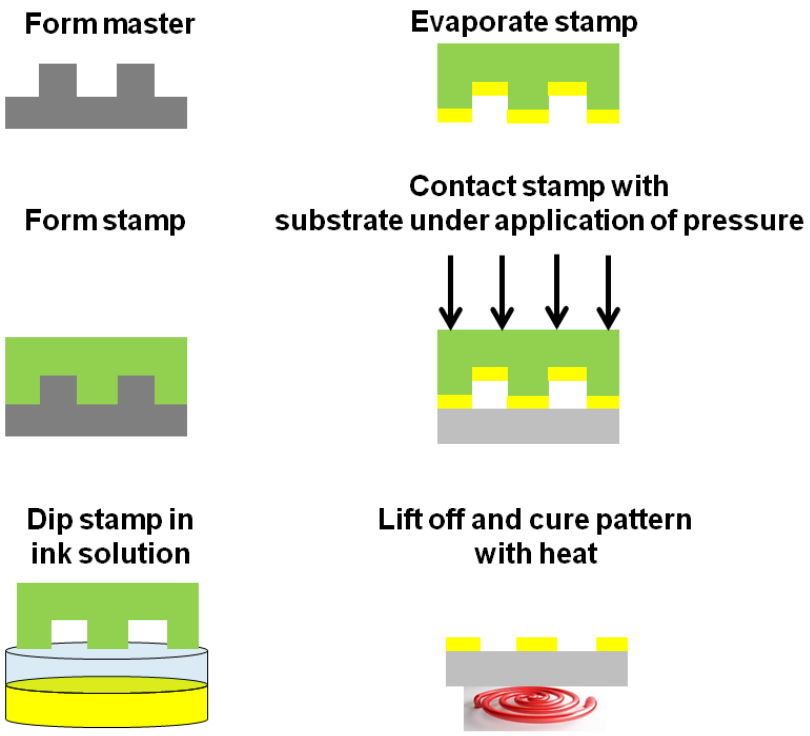


Figure 1.6. Schematic of microcontact printing (μCP) processing consisting of : (1) lithographic forming of master, (2) casting of an oppositely patterned stamp, (3) dipping of stamp into ink solution, (4) evaporating of excess ink, (5) contacting of the stamp with the substrate under the application of pressure and (6) lifting off and curing of the pattern.

Though very effective at blocking the growth of ALD films, SAMs have several limitations in the AS-ALD process. In previous Bent Group research, it was found that the packing density of SAM molecules is a critical factor for the ability to block film growth [107, 111, 122]. To achieve complete blocking of ALD films, the formation of densely packed SAMs is required, but this is time-consuming and requires careful control over humidity and other conditions [107, 111, 122]. In effect, these challenges

present a drawback in using SAMs as ALD resists and integrating them into current processes for device fabrication. In addition, because the thickness of the SAM layer is in the range of few nanometers, the lateral growth of the deposited film above the thickness of the SAM, namely a size effect, can be problematic for the fabrication of nanoscale patterns [123]. As a result of the limitations of SAMs, another type of resist, a polymer, was studied for AS-ALD of platinum (Chapter 3).

1.3.2. Polymer resists

Another form of surface passivation for ALD has been polymer resists. Many polymers offer the advantages of being inexpensive and easy to apply onto substrates by well-established methods, such as spin coating. Because polymers are not formed by molecular ordering like SAMs, packing density limitations characteristic of SAMs can be avoided. Additionally, the easy thickness controllability of polymer films is beneficial for nanoscale pattern fabrication. Previous studies have used poly(methyl methacrylate) (PMMA) [124-129], poly(vinyl-pyrrolidone) [130] and poly-*tert*-butyl-methacrylate[131] for AS-ALD resist. However, the studies were mainly focused on the blocking ability of the polymer depending on the reaction chemistry [125, 127] and the feasibility of applying AS-ALD using polymers to various ALD processes [124, 130].

For patterning methods in AS-ALD, the previous reports have employed conventional photolithography with a UV light source [125-127, 129]. Also, Färm et al. used atomic force microscopy to make a pattern in the PMMA polymer by localized heating [130]. Although soft lithography has shown many advantages for AS-ALD with SAMs, the patterning for polymer resists to date was still performed by

conventional top-down processes. In Chapter 3, the use of polymethacrylamide (PMAM) will be discussed as a water-soluble thermally-stable polymer used in microcontact printing in AS-ALD.

1.4. ALD of TCOs

The second half of this thesis describes the use of ALD to deposit transparent, conducting tin oxide (Chapter 5) and to sample compositions by alternating layers of zinc and tin oxide (Chapter 6).

1.4.1. Overview of TCOs

TCOs are wide-bandgap ($\geq$ 3 eV), transmissive to visible light ($\geq$ 80%) and highly conductive ($\geq 10^3$ S-cm^{-1}) metal oxides with many applications in consumer electronics--flat panel displays, functional glasses and light emitting diodes-- and in photovoltaics [80, 82, 132, 133]. The oxides of indium, tin and zinc, which comprise the zinc indium tin oxide (ZITO) family, are the most commercially-important TCOs [134]. These binary TCOs are typically doped with an impurity to improve stability at high temperatures [135]. Within the ZITO family, indium tin oxide (ITO) remains the industry-standard for high-end TCOs because of its high conductivity ($\geq 10^4$ S-cm^{-1}) [136-138]. However, the scarcity of indium coupled with the increasing demand in consumer and photovoltaic markets has led to rising costs [81]. According to the 2012 U.S. Geological Survey Mineral and Commodity Summaries, the annual average price of indium per kilogram increased almost 25% from 2010 ($565/kg) to 2011 ($720/kg) [139]. The high expense and scarcity of indium motivate the need to find alternative TCO materials and investigate a wide variety of deposition techniques. In the section

below, ALD is briefly described as a promising method of carefully depositing these TCO materials.

1.4.2. Use of ALD to Control Composition of Ternary Metal Oxides

ALD consists of sequentially dosed half-reactions. The highly tunable nature of each precursor half-reaction enables the alloying or doping of materials. So far, ALD has been used to deposit many ternary metal oxides including AZO [140-144], GZO [145, 146], ITO [56], (Zn,Mg) O_x [147], Zn(O,S) [148] (Sn,Al)O_x [149] and very recently, ZTO [88-91], the indium-free alternative of interest in this thesis.

The challenges faced in depositing ternary metal oxides by ALD parallel those that are common in binary ALD processes with the added complexity of system compatibility. Not only must the individual binary ALD systems be reproducible and well-characterized, but there also needs to be compatibility in chemistries, ALD temperature windows and overlap in the ability to growth surfaces. Another important but not necessarily obvious consideration is the crystal phase of the as-deposited binary component metal oxides. It may be worthwhile to choose binaries with as-deposited crystalline phases to facilitate ease of film structural and electrical characterization. As shown in Chapter 6, the difference in phase between amorphous as-deposited SnO_x and polycrystalline hexagonal wurtzite ZnO resulted in loss of long-range order as a function of increasing tin content. While the amorphicity of these films may make electrical and structural characterization more challenging, amorphous films may be preferred for some systems over others. In spite of the challenges of developing ternary metal oxide ALD systems, the ability to control film lamination and composition to tune desired film properties motivates continued studies in this field.

1.5. Organization of Thesis

This thesis has been organized to provide further details on the use of ALD for spatial and compositional control of conductive materials. Chapter 2 provides a detailed description of ALD reactors used to deposit these materials. The principles and theory of a variety of analytical methods and the associated equipment are also described in Chapter 2. The next two chapters describe the use of ALD to spatially control platinum. In Chapter 3, a water-soluble polymer, PMAM, is used as a resist for the AS-ALD of platinum. Microcontact printing of this polymer with 500 μm x 500 μm and 2 μm x 2 μm arrays are used to define regions for selected growth. The use of elemental mapping from scanning Auger electron spectroscopy shows successful polymer stamping and good control over the deposition of platinum in desired regions. In Chapter 4, another means of spatially-selective ALD of platinum is explored. In this case, ODTS is used as a template to direct the growth of platinum nanoparticles. The presence of defects provides nucleation sites for platinum ALD and the ability to control the density of these defects enables the control of the nanoparticle density and to some extent size. Images from scanning electron microscopy and particle counting software provided the clearest evidence for the ability to control platinum nanoparticle growth using this method.

In Chapters 5 and 6, an ALD processes for conductive metal oxides, tin oxide and zinc tin oxide, respectively, are carefully developed and described. Thin film characterizations of the structural and optical properties of these TCOs are also presented. Chapter 5 describes the development of a tin oxide ALD system that uses a mild counter-reactant, water, capable of depositing films at near-room temperature. The

development of this tin oxide system combined with a compatible zinc oxide process enabled the characterization of a thermal zinc tin oxide ALD system (Chapter 6). This chapter explores the effects of film lamination--a parameter defined as the degree of lamination--on the growth behavior and material properties of zinc tin oxide. Previous ternary oxide ALD studies have not rigorously studied such effects.

The thesis concludes with Chapter 7 in which the general conclusions and future directions for this work are presented.

1.6. Collaborations

The work in this thesis represents collaboration and interactions with many talented scientists. Dr. Xirong Jiang provided mentorship and training for ODTS SAM growth and initial platinum ALD studies during her final years as a graduate student and therefore provided a solid foundation for much of this work. Dr. Han-Bo-Ram Lee was instrumental in image analysis of platinum nanoparticles deposited via ALD on ODTS SAM templates (Chapter 4). While full details of how this nucleation behavior was modeled are not included in this thesis, general findings are described in Chapter 4. Dr. Lee also conducted the experiments and analysis associated with removal of PMAM for the AS-ALD of platinum via Fourier Transform Infrared (FTIR) spectroscopy (Chapter 3). Dr. Carl Hägglund provided expertise in optical analysis of tin oxide and ZTO via spectroscopic ellipsometry (Chapters 5 and 6). His contributions were not limited to characterizing the optical behavior of these TCOs. He was also the designer and chief builder of the ALD reactor used for metal oxide experiments, which is discussed in detail in Chapter 2. Dr. Jukka Tanskanen provided insight into the effects of surface hydroxylation density and the reactivity of the tin precursor on the overall growth of

ZTO (Chapter 6). His expertise in DFT will be used for future publications of the effects of ligand size difference on the ZTO ALD growth mechanism and surface reactions for tin oxide ALD.

Chapter 2. Analytical Methods

This chapter describes the theoretical and major experimental methods used to carry out the research described in this thesis. Because ALD is central to these studies, a brief description of the reactors used is provided. After this brief introduction, several analytical techniques used in analyzing platinum, tin oxide and zinc tin oxide thin films are described. All but one technique, inductively-coupled plasma optical emission spectroscopy (ICP-OES), are surface-sensitive. These surface analytical methods include ellipsometry, water contact angle goniometry, scanning electron microscopy (SEM), x-ray photoelectron spectroscopy (XPS), Auger electron spectroscopy (AES), ultraviolet-visible spectroscopy (UV-Vis) and x-ray diffractometry (XRD).

2.1. Atomic Layer Deposition Reactors

The ALD experiments performed for studies on platinum were carried out in a home-built hot wall reactor as described in previous Bent Group studies [38, 39, 150]. This reactor was used for studies performed in Chapters 3 and 4. A photograph of the ALD reactor configured for platinum and titanium dioxide systems is shown in Figure 2.1Figure 2.1. A substrate, up to four inches in diameter, could be loaded through a door placed perpendicular to the substrate. Nitrogen carrier gas (99.999 %, Air Products) at 10 sccm flows through the top of the reactor. The shower-head design of the precursor inlet coupled with the flow of nitrogen made possible uniform distribution of material. A chemical-series rotary vane pump (Alcatel) was used to achieve vacuum (~100 mTorr) during the ALD process. A heater sat directly below the reactor stage and was responsible for heating the substrate. Heating tape was wrapped around the

reactor body and along specific precursor lines for region or zone-specific heating. A LABVIEW program was used to externally control the heating of these components and the opening of pneumatic valves associated with precursor delivery.

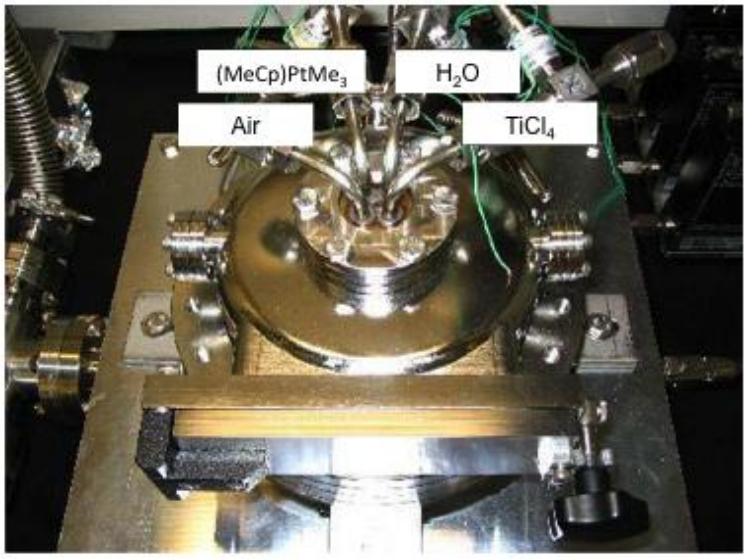


Figure 2.1. Photograph of home-built hot wall reactor capable of holding a four inch wafer. Shower-head design of precursor inlet along with flow of nitrogen carrier gas enables uniform radial distribution of deposited material to the substrate.

The ALD experiments used for growth of SnO_x, ZnO and ZTO, which are described in Chapters 5 and 6, were carried out in a custom-built, viscous-flow, hot-wall reactor shown schematically in Figure 2.2. The substrates were loaded into a tube style body (with 35 mm diameter and ~300 mm length) on a stage with an internal thermocouple close to the substrate. Nitrogen carrier gas (99.999%, Air Products) at 10 sccm was flowed through the tube, enabling efficient transport of the precursors introduced at its upstream end. The reactor was evacuated by a rotary vane pump (Alcatel) resulting in a typical pressure of 100 mTorr during ALD. Precursor pressure pulse amplitudes were in the range of 1 to 50 mTorr above the 100 mTorr baseline

pressure. A quadrupole mass spectrometer (SRS RGA200) was used to sample the gas composition through a needle valve downstream of the ALD substrate.

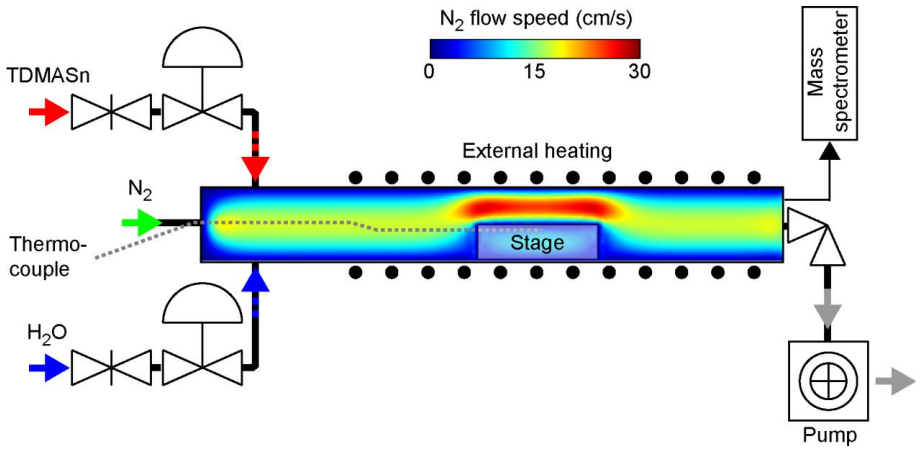


Figure 2.2. Schematic of the custom-built, hot-walled ALD reactor. The main part was a cylindrical tube, heated externally. The tube was fitted with inlets for nitrogen carrier gas and precursors close to its upstream end. A sample stage with in-situ temperature monitoring is positioned near the center of the tube. A separately pumped mass spectrometer was used to analyze gas sampled downstream the stage by means of a needle valve. The finite element method was used to model the carrier gas flow and diffusion through the tube, indicating even distribution of the precursors. The flow profile in the mid section of the tube is shown.

2.2. Ellipsometry

2.2.1. Introduction

Ellipsometry is a powerful optical technique used in many applications including thin film metrology. Its name is derived from the elliptical shape traced by the electric field vector for light and measures the change in light polarization upon reflection from a substrate. This analysis yields information about layers that are thinner than the wavelength of the light itself, down to a single atomic layer or less [151]. Spectroscopic ellipsometry measures functions of complex reflection coefficients, which by themselves are not useful [152]. Useful information such as film

thickness, surface roughness, thickness and a variety of optical properties are determined by modeling the near-surface region of the substrate and then fitting these data to models [153].

2.2.2. Theory

Elliptically polarized light possessing an electric field vector that traces the same ellipse at a fixed point in space is the most general state of polarization for monochromatic light. The changes in polarization of light due to reflection from the substrate are measured and used to calculate useful optical properties. First, monochromatic light is linearly polarized and then elliptically polarized by a compensator, also known as a retarder, which changes the phase of the incident wave thereby delaying one of the two orthogonal light constituents. All of these components are in line with the x-ray source. Following light reflection from the substrate surface, light polarization is analyzed by the coupling of a linear analyzer and a photodetector. The electric vector matrix, **E** can be represented by the polarization of light into *p* and *s* components which are parallel and perpendicular to the substrate plane, respectively [154]. The effect of the reflection on the incidence light is quantified by the reflection coefficent matrix **R**, as shown in Equation 2.1 [154]. Reflection of incident light $\mathbf{E}_r$ and the incident $\mathbf{E}_i$ are correlated by the reflection coefficient matrix, **R**

$$\mathbf{E}_r = \mathbf{R}\mathbf{E}_i \tag{2.1}$$

$$\mathbf{R} = \begin{bmatrix} R_{pp} & 0 \\ 0 & R_{ss} \end{bmatrix} = \begin{bmatrix} R_{pp}|e^{j\delta_{pp}} & 0 \\ 0 & R_{ss}|e^{j\delta_{ss}} \end{bmatrix} \tag{2.2}$$

In the above equation j=√(-1) and R_{pp} and R_{ss} are the reflection coefficients. The quantity ρ represents the ratio of the reflection coefficients as measured by the ellipsometer (Equation 2.3):

$$\rho = \frac{R_{pp}}{R_{ss}} = \left|\frac{R_{pp}}{R_{ss}}\right| e^{j(\delta_{pp}-\delta_{ss})} = \tan\psi \cdot e^{j\Delta} \qquad (2.3)$$

$$\tan\psi = \left|\frac{R_{pp}}{R_{ss}}\right| \qquad (2.4)$$

The quantities ψ and Δ are called the ellipsometric angles or Stokes parameters [151]. Ellipsometry measures ψ and Δ, which represent the relative amplitude change and the relative phase shift, respectively. The quantity tan ψ in Equation 2.4 is the ratio of the amplitude attenuation for the *p* and *s* polarization based on reflection. The angle Δ from Equation 2.3 represents the difference between phase shifts for the *p* and *s* polarizations following reflection.

These ellipsometric angles are used with the Fresnel equations to solve for optical properties and film thickness [153]. The Fresnel equations describe the behavior of light moving between media with different refractive indices. The different media studied include the air, the film and the substrate; therefore, three complex indices of refraction were defined. They are N_0 (air), N_1 (film) and N_2 (substrate) where these complex indices of refraction are comprised of the real (*n*) and imaginary (*k*) components:

$$N = n + ik \qquad (2.5)$$

The Fresnel equations can be used to correlate the ratio of reflection coefficients ρ with the indices of refraction *N*, the incident angle of the light θ, the wavelength of the light λ, and the film thickness, *d* and may be represented as follows in Equation 2.6:

$$\rho(N_0, N_1, N_2, \theta, \lambda, d) = \tan\psi \cdot e^{j\Delta} \quad (2.6)$$

Since the ellipsometric angles are directly measured, it is of interest to separate Equation 2.6 as follows:

$$\psi = \tan^{-1}|\rho(N_0, N_1, N_2, \theta, \lambda, d)| \quad (2.7)$$

$$\Delta = \arg[\rho(N_0, N_1, N_2, \theta, \lambda, d)] \quad (2.8)$$

Equations 2.7 and 2.8 comprise a system of two equations with nine independent variables. Fortunately, the angle of incidence and the wavelength of light, λ, can be fixed or systematically controlled by software. The components of each refractive index may be found in a database or measured prior to film deposition. Following initial guesses for film thickness and the real component of refractive index, ρ can be determined numerically from the Fresnel equation. Sophisticated models that take into account materials characteristics such as interfacial surface roughness, dispersion of voids, mixed optical properties have been developed in order to more accurately determine ρ [152].

2.2.3. Equipment

The three ellipsometers used for experiments conducted in this thesis included the Gaertner L116C Ellipsometer and two Woollam Variable Angle Spectroscopic Ellipsometers, the α-SE, located in the Bent Research Group and the M2000, located in the Stanford Nanofabrication Facility. The Bent Research Group Woollam α-SE is pictured in Figure 2.3.



Figure 2.3. Picture of the Woollam α-SE Variable Angle Spectroscopic Ellipsometer (VASE) with support computer and pump.

Figure 2.4 shows a schematic of the basic components of an ellipsometer. Single-wavelength ellipsometers such as the Gaertner use a monochromatic light source which is typically a laser in the visible spectral region. Spectroscopic ellipsometers such as the Woollam models described above use broad band light sources and can cover the infrared and ultraviolet regions. Before the light strikes the sample, a polarizer linearly polarizes light and a compensator, such as a quarter wave plate, further alters polarization state. After reflection, the light passes through a compensator, a second polarizer, which is called an analyzer, and is subsequently sent to a detector.

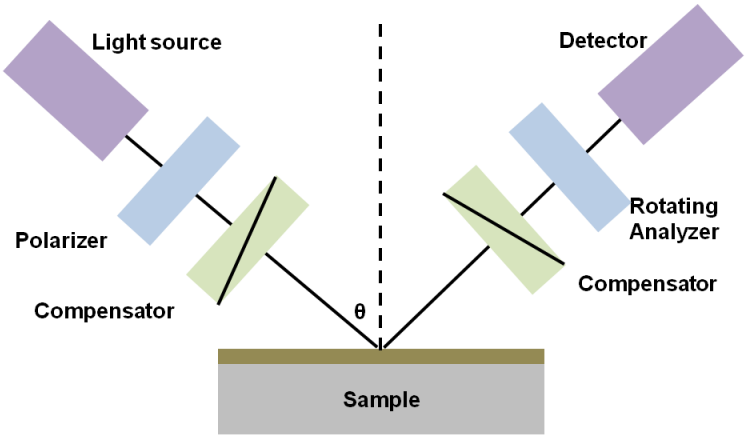


Figure 2.4. Schematic of basic components of an ellipsometer including a light source, polarizer, compensator, analyzer and detector.

Measurements taken with the Gaertner ellipsometer used $\theta = 45$ º and $\lambda = 633$ nm from a HeNe laser source. This ellipsometer was monochromatic and had a quarter wavelength compensator. The optimum sample height was manually determined by maximizing specular reflectance from the sample to the detector. After inputting tabulated values for the complex indices of refraction for the air and the substrate, the ellipsometry software was used to calculate angles ψ and Δ and then iteratively solve for the unknown film thickness. The Woollam spectroscopic ellipsometers allowed for sampling of θ at 65 º, 70 º and 75 º over a wide spectral range of λ (200-1690 nm). Established models were modified so that thickness and optical properties of multiple layers could be determined simultaneously without using tabulated values of *n* and *k*.

2.3. Water Contact Angle Goniometry

2.3.1. Introduction

The extent to which a liquid wets a solid surface is a quantifiable means of determining interfacial interactions. For instance, the degree to which a liquid wets a surface coating on a flat solid can provide useful surface-sensitive information on the hydrophobicity, homogeneity or roughness of that material.

2.3.2. Theory

The contact angle measures the wettability of a solid surface by a liquid and can be described by the Young equation:

$$\gamma_{LG}\cos(\theta_c) = \gamma_{SG} - \gamma_{SL} \qquad (2.9)$$

where the θ_c represents the contact angle and γ_{LG}, γ_{SG} , γ_{SL} represent interfacial tension among the liquid/gas, solid/gas and solid/liquid interfaces.

Figure 2.5 presents a schematic of the components of the Young equation.

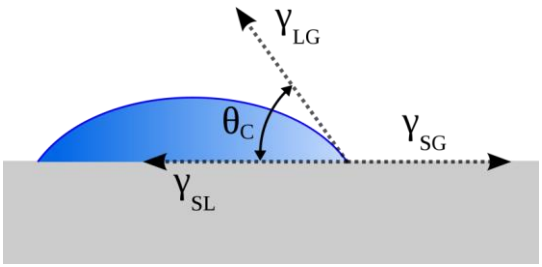


Figure 2.5. A schematic of the contact angle, θc, where the solid-liquid (γ_{SL}) and liquid-gas (γ_{LG}) interfaces meet. Also represented is the solid-gas interface (γ_{SG}).

A low value for θ_c means that the liquid spreads and therefore wets the solid surface well while a high value represents poor wetting. In the analysis performed to

determine θ_c in this thesis, water was used as the liquid and therefore the contact angle measured is called the water contact angle (WCA). At equilibrium conditions, a system possesses a unique static WCA [155]. In general, values of WCA below 30 º represent a hydrophilic interaction while those above 30 º represent a hydrophobic interaction [155]. For instance, for the ODTS SAM on silicon dioxide (SiO_2) used in this thesis, the static water contact angle was about 110 º [156, 157]. By knowing the values for WCA on a bare SiO_2 surface and that for a completely formed. defect-free ODTS SAM, insight into incomplete SAM formation could be determined.

The WCA described above is a static or equilibrium value, and this was the only type of WCA that was measured for the work in this thesis. However, θ_c, may also be measured at a maximal value when the liquid drop swells. This value is known as the advancing contact angle [155]. Conversely, when the liquid drop shrinks, the minimal or receding θ_c may be measured. Contact angle hysteresis is defined by the difference pbetween the advancing and receding θ_c [155]. Contact angle hysteresis has been used to characterize inhomogeneous surface properties such as roughness and mobility [155].

2.3.3. Equipment

Determining WCA is very convenient and is performed using a charge coupled device (CCD) camera to directly image and a computer program to measure the solid-liquid-vapor angle of a static drop of water on flat solid surface [158]. For the experiments described in this thesis, a FTA200 Dynamic Contact Analyzer was used. Figure 2.6 shows an image of the equipment which was comprised of a liquid droplet delivery system, a micro-motor, a CCD camera and an analysis program.



Figure 2.6. The FTA 2000 Dynamic Contact Angle Analyzer used to determine static water contact angles of ODTS SAMs for this thesis. The system is comprised of micro-motor, a liquid droplet delivery system, a CCD camera and an analysis program.

2.4. Scanning Electron Microscopy (SEM)

2.4.1. Background and Basic Principles

In scanning electron microscopy (SEM) a focused primary electron beam is rastered across a surface and generates secondary electrons that can be analyzed in order to generate an image. An electron may interact with a sample surface in a variety of ways to generate different signals (Figure 2.7). Signals produced by these interactions can be described as a "volume of interaction" and include secondary electrons (SE), back-scattered electrons (BSE), characteristic X-rays, light (cathodoluminescence), transmitted electrons and sample current[159]. From these different signals surface morphology, topography and composition may be determined. While it is rare that any one microscope has all of these features, advances in optical technology and image processing have produced equipment capable of high resolution--on the order of < 1 nm.

In order to generate an image with such high resolution, primary electron beams are narrowly focused and yield a large depth of field. A large depth of field yields three-dimensional imaging with high resolution.

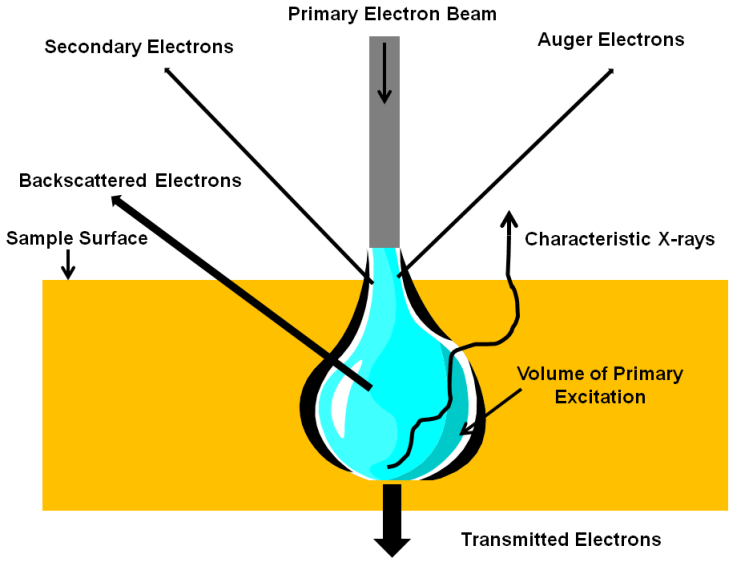


Figure 2.7. Schematic of primary electron beam interaction with a solid surface to generate different species including secondary electrons (SE), backscattered electrons (BSE), Auger electrons, transmitted electrons and characteristic x-rays. Schematic adapted from *Surface Science Foundations of Catalysis and Nanoscience* [154].

2.4.2. History

Conceptualization of the SEM began in the 1930s with work of German physicist Max Knoll [159]. In the early 1940s, the modest resolution of the SEM (~50 nm) was overshadowed by the improving resolution of transmission electron microscopes (TEMs); therefore interest in developing SEMs lagged for almost a decade [159]. In 1960, when Everhart and Thornley improved the SE detector to improve the signal to noise ratio and image contrast, there was a resurgence in the development of commercially-viable SEMs. Since then, numerous advances in intensity and brightness of electron sources, contrast mechanisms, electron detection systems, lens technology,

computation, image acquisition software, sample preparation methods and pressure regulation have led to the creation of more powerful microscopes with resolution approaching the sub-nanometer scale. Relative ease of use coupled with these improvements in resolution and image acquisition have enabled SEM to play a major role in surface analysis.

2.4.3. Equipment

Basic components of an SEM include an electron optical column housing an electron source, electron gun, lenses, a vacuum chamber for sample loading, pumps, sophisticated electronics, detectors and software. Figure 2.8 shows a schematic of an SEM.

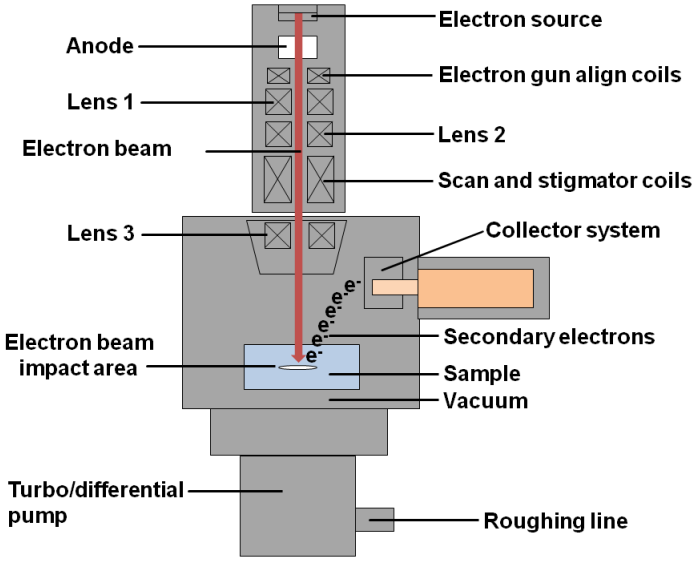


Figure 2.8. Schematic of major SEM components including electron source, electron guns, lens, sample chamber, secondary electron collector and detector system and associated pumps. Adapted from *An Introduction to Electron Microscopy* [161].

The electron gun sits atop the electron optical column and produces a beam that is finely focused into a spot as small as 1 nm in diameter on the sample surface. This beam is scanned in a rectangular raster over the specimen, and the intensities of various signals created by beam electrons and specimens (described in Figure 2.7) are measured and manipulated using software [160]. These acquired and stored images are mapped as a function of variation in brightness and contrast on the image display. The signal of interest is usually from SEs and varies with the topography of the samples so that edges are bright and recesses are dark [160]. Image magnification is defined as the ratio of the size of the displayed image to the size of the area scanned.

The resolution in an SEM depends on the degree to which the signal can be associated with the position of the electron beam and for a particular beam location, the size of the region within the sample from which the signal originates [161]. The type of signal, beam spot size, beam current, sample composition and beam distance from the sample influence image resolution. In general, when an SEM is operated under lower voltages, with minimal sample impingement and therefore minimal sample interaction, the spot size is the factor that primarily affects image resolution [161]. At higher voltages, the volume of interaction from which the signal originates increasingly becomes the primary determinant of image resolution [161]. All the SEM images in this dissertation were performed in secondary electron (SE) mode. These FEI SEMs with field guns (FEGs) were the XL30 Sirion and the Magellan 400 XHR. The XL30 Sirion had a resolution of ~ 5nm whereas the Magellan 400 XHR, a more modern and powerful tool, had an optimum resolution of 0.8 nm.

2.5. X-ray Photoelectron Spectroscopy

2.5.1. Introduction

X-ray photoelectron spectroscopy (XPS), also known as Electron Spectroscopy for Chemical Analysis (ESCA), is a technique that allows for the elemental identification of components within a material by the study of the energy distribution of the electrons emitted from x-ray irradiated compounds. Performing surface analysis via XPS involves the use of monoenergetic soft x-rays followed by analysis of the detected electrons. The photons of the x-rays penetrate the sample on the order of 1-10 µm, interact with surface atoms and cause the ejection of electrons via the photoelectric effect [162]. Figure 2.9 shows a schematic of the photoelectric effect.

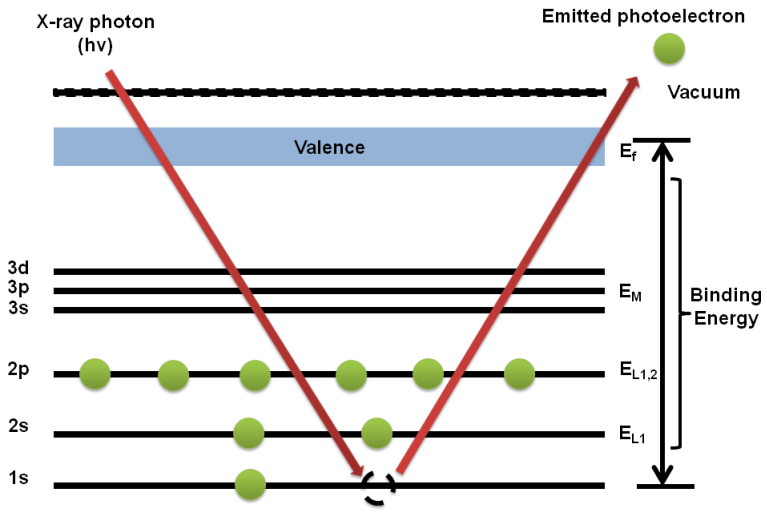


Figure 2.9. A schematic of the photoelectric effect. Incident x-ray photons are able to excite and eject a core level electron if its energy is greater than the binding energy of the electron.

Since core level electrons from atoms within a film have energies unique to each atom, an atomic fingerprint can be determined. The core level electrons can provide

useful information beyond atomic concentration from the electron counts such as shifts in binding energy of other atoms, which may elucidate the chemical environment of surrounding electrons. Because excited electrons can travel only 1-10 nm through solids, XPS is very surface-sensitive.

2.5.2. Theory

Heinrich Hertz discovered the photoelectric effect in 1887, and these findings provide the theoretical foundation of XPS. In the photoelectric effect, Hertz observed that light could eject electrons from a metal provided that its energy was greater than the work function of the metal. The process was extended to practical application in the mid-1960s by Kai Siegbahn and was first known as ESCA. Commercially manufactured spectrometers were available in the early 1970s. For his pioneering work in XPS, Siegbahn was awarded the Nobel Prize for Physics in 1981.

The technique of XPS uses the principles associated with the photoelectric effect as incoming soft x-rays photons (~1500 eV) with binding energies greater than core level electrons are able to excite and eject these electrons. Typically, the energy of the incident x-rays (hν) can be selected by choosing a light source while an electron detector measures the resulting kinetic energy of the electrons (E_K). The Einstein equation defines the electron binding energy (E_B) referenced to vacuum level as the difference between the incident photon energy (hν) and the kinetic energy of the electrons E_K (Equation 2.10) [154, 162].

$$E_B = h\nu - E_K \qquad (2.10)$$

The process of photoemission describes the initial and final states of an atom with *n* and *n-1* atoms, respectively. Therefore, the binding energy of an electron is equal to the difference between the final and initial states of the atom as shown in Equation 2.11,

$$E_B(k) = E_f(n-1) + E_i(n) \quad (2.11)$$

where $E_f(n-1)$ is the final state energy following photoemission and $E_i(n)$ is the initial state energy before emission. More rigorous treatment of a single-electron event uses electron wave-functions to understand the processes that take place following ionization including relaxation, relativistic effects and electron correlation [154].

Analyzing the kinetic energy of the emitted electron, E_K, provides a framework for understanding the many final ionic states for each type of atom. E_K may be described as shown in Equation 2.12 **,**

$$E_K = h\nu - E_B - \Phi_s \quad (2.12)$$

where hν is the energy of the photon, E_B is the binding energy of the atomic orbital corresponding to the difference in the initial and final states of the atom and Φ_s is the work function of the spectrometer. Many final states of ions from each type of atom exist. As a result, many corresponding kinetic energies exist for these emitted electrons. There is also a different probability of cross-section for each final state. Binding energies for different ionization cross sections may also be referenced with respect to the Fermi level. A schematic can be drawn in which line lengths correspond to the relative probabilities of the s, p, d and f ionizations. Because the p, d and f levels become split upon ionization, vacancies exist with respect to certain spin-orbit ratios. For instance, there is a 1:2 ratio for p levels, 2:3 for d levels and 3:4 for f levels. The unique set of binding energies for each element enables XPS to identify and determine

the concentration of elements on a surface [162]. Chemical shifts, which are changes in elemental binding energies, are caused by differences in chemical potential and polarizability of compounds. As a result, the chemical state of materials analyzed may be determined.

Auger electrons may also be emitted in the photoelectric process because of the relaxation of the remaining excited ions after photoemission. This Auger emission occurs ~10^{-14} s after the emission of a photoelectron. A competing process, fluorescence, is only a minor contributor in this energy range. In the Auger process, an outer level electron falls into and occupies the inner orbital vacancy while a second electron is simultaneously emitted carrying away the excess energy. Path lengths of incident x-ray photons (~1-10 μm) and emitted electrons (tens of Ångstroms) give rise to the surface sensitivity of XPS. Only those electrons that originate from within tens of Ångstroms below the surface can be emitted without energy loss. These emitted electrons can be used to generate peaks corresponding to ionization cross sections.

Typical spectral output from a peripheral computer with associated software shows a spectrum displayed as a plot of the electron counts versus electron binding energy at small fixed energy intervals. Sharp, well-defined peaks come from electrons that have not undergone inelastic energy loss while those that have lost energy increase the level of the background at binding energies higher than the peak energy. Spectral lines associated with the XPS data collection include the photoelectron lines, Auger lines, x-ray satellites, x-ray ghost lines, shake-up lines, multiplet splitting, energy loss lines and valence lines and bands. Electrons undergo inelastic collisions before

emerging from the background and each element has a characteristic inelastic mean free path.

2.5.3. Equipment

Major components of a commercial XPS system include the following: 1) x-ray source, 2) ultra-high vacuum (UHV) chamber with UHV pumps, 3) electron collection lens 4) electron energy analyzer 5) magnetic field shielding, 6) electron detector system, 7) sample loading chamber with arm and relevant pumps 8) sample mounts, 9) sample stage and manipulators and 10) ion gun used for sputtering. The spectrometer used for thin film characterization in this work was a PHI VersaProbe Scanning XPS Microprobe. In standalone spectrometers such as the PHI VersaProbe, x-rays are generated by the bombardment of high-energy electrons on a metal anode. Common metal anodes that generate x-rays at certain transitions are the Al-Kα (1486.6 eV), Mg-Kα (1253.6 eV) and monochromatic Al-Kα (1486.7 eV) transitions. The x-ray source used in these studies was the monochromatic Al-Kα, which were derived from the diffraction and focusing of a beam of non-monochromatic X-rays from crystalline quartz with a corresponding wavelength of 8.334 Å or 1486.7 eV.

During data acquisition, a series of lenses in the electron analyzer focuses electrons emitted from a sample, and an energy analyzer selects and counts electrons of certain energies. More modern XPS systems use a hemispherical energy analyzer that consists of two concentric hemispherical electrodes held at different potentials. Electrons of only a certain kinetic energy, called the pass energy, can pass through the electrodes without hitting the walls. In this way, the hemispherical energy analyzer acts

as a narrow band energy filter. After filtering, these electrons are directed to a detector that counts the electrons and converts them to electric signal. During data acquisition, the PHI XPS software allowed for real-time monitoring of electron counts plotted against binding energy. Following data acquisition, the PHI MultiPak software was used for Gaussian peak fitting using a Shirley background as a baseline.

2.6. Auger Electron Spectroscopy (AES)

2.6.1. Background

Auger electron spectroscopy (AES), which may also be known as scanning Auger microscopy (SAM), is used to study elemental and chemical composition of atomic layers of surfaces. In this process, following core level ionization, an atom will relax to a lower energy state to fill a vacancy through a two electron coulombic rearrangement resulting in a doubly ionized state. The energy difference between these states is carried away by the Auger electron. The ejected Auger electron has a kinetic energy characteristic of its parent ion. With the exception of hydrogen and helium, every element can emit an Auger electron and therefore be identified by its Auger spectrum. Electrons have small mean free path in solids (~5-10 nm). In fact, Auger electrons can only escape from the outer 5-50 Å of a surface. As a result, AES is surface sensitive.

2.6.2. Theory

AES was described by Pierre Auger in the early 1920s to explain radiationless relaxation of excited ions in cloud chambers [163, 164]. Though many texts credit Auger with first discovering this effect, revisionist historians credit Lise Meitner as

being the first to do so in 1922 [165, 166]. Though it may be controversial to say so, many forces of discrimination worked together to deny Meitner credit and a Nobel for this and other discoveries. The first practical equipment to measure Auger electrons was discovered in 1967 by Palmberg and Tharp and Scheibner through use of Low Energy Electron Diffraction (LEED) [167, 168]. By 1969, surface sensitivity of AES was improved by the use of a cylindrical mirror analyzer (CMA) [169]. The sensitivity of AES continues to be improved.

In the Auger process, the incident primary electron bombardment takes place at energies in the 50 meV to 3 keV range [154]. Unlike the single-electron system described in the XPS section, Auger spectroscopy relies on the coupling between electrons. Following ionization due to core level election ejection, a higher lying core or valence electron may fill the resulting hole in a radiationless transition. The atom is therefore in an excited state. The ejection of a second electron removes this excited state. Figure 2.10 adapted from *Surface Science: Foundations of Catalysis and Nanoscience,* summarizes the a KL_1L_2 Auger transition which involves three core levels [154].

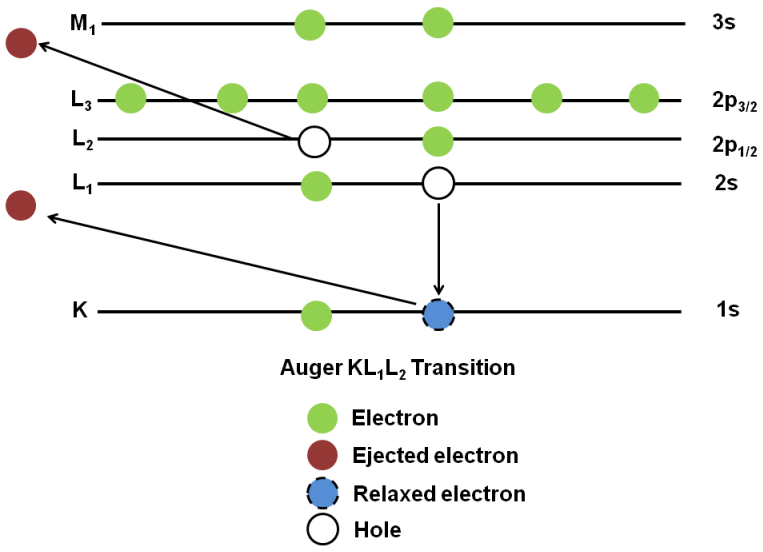


Figure 2.10. Schematic of Auger transition of three core levels K, L1 and L2. An electron is emitted and another relaxes into its place resulting in the simultaneous ejection of another core-level electron [155].

Determining the energy of an Auger transition is difficult because of the numerous electron effects and final state energies for consideration. In fact, only low resolution is required for quantitative surface analysis, so small energy differences between final and initial state multiplets may be neglected [154]. While Auger transitions from different elements are usually widely spaced, when they do overlap quantitative analysis becomes difficult [154]. In the case of Auger transition overlap, XPS may be a useful alternative for quantitative analysis.

Figure 2.11, adapted from *Surface Science: Foundations of Catalysis and Nanoscience*, presents a schematic of approximating a KLV Auger transition where the energy scale is referenced with respect to the Fermi level (E_F) and the relevant associated energetics [154]. The primary electron e_p^- has enough energy to ionize the core level energy E_W. An electron at energy E_X relaxes into the initial hole left by e_p^-. The energy from this ionization process is carried away by electron E_Y which is ejected

into vacuum. In order to reach vacuum level, E_Y must exceed the work function of the sample. E_Y not only has to exceed the work function of the sample but must also exceed that of the spectrometer Φ_{sp} in order to be detected. With all these energy barriers to overcome, the kinetic energy of an electron for this KLV Auger transition can be represented as shown in Equation 2.13:

$$E_{Kin} = E_{XWY} = E_K - E_L - E_V - \Phi_{sp} \qquad (2.13)$$

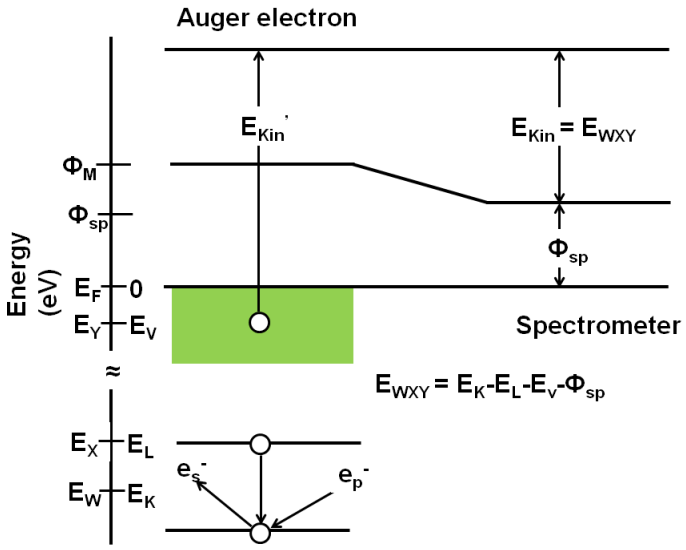


Figure 2.11. Energy levels for a KLV Auger transition referenced with respect to the Fermi level (E_F) and showing the influence of the spectrometer work function Φsp. Adapted from Surface Science: Foundations of Catalysis and Nanoscience [155].

Figure 2.7 from Section 2.4 shows that the volume of primary excitation results in different types of electron emission including secondary, backscattered and Auger electrons. The acquired signal is a function of the kinetic energy of these electrons, *N(E)*, and is composed of peaks from the Auger electrons at well-defined energies along with a continuous background [154]. The signal *N(E)* is also known as the integral signal. Oftentimes, because peaks are difficult to determine based on the

N(E) spectrum, the differential signal d*N(E)*/d*E* is calculated and plotted versus the kinetic energy. Auger transitions are labeled according to the most negative part of this differential spectrum.

In a binary mixture, AB, compositional fractions are taken with respect to relative sensitivity factors, s_X, and the mole fractions of one component, A, can be approximated as shown in Equation 2.14 [154].

$$x_A = \frac{I_A/s_A}{I_A/s_A + I_B/s_B} \tag{2.14}$$

In Equation 2.14, I_A and I_B are the peak intensities of the constituent components and s_A and s_B the associated relative sensitivity factors. This equation can be expanded for a multi-component system. Peak intensity is more accurately determined from peak area for data taken in integral mode than from peak amplitude taken in differential mode.

2.6.3. Equipment

AES is usually performed under ultra high vacuum (UHV). Peripherals to the UHV chamber typically include an electron gun, scanning electronics for imaging, an energy analyzer and computer for data storage and processing [170]. The AES used in this thesis is the PHI 700 Scanning Auger Nanoprobe (Figure 2.12). This AES was fully automated with control software and data processing using the PHI MultiPak software. Besides the analysis depth of 5-50 Å, this equipment had a secondary electron image resolution of 6 nm, Auger electron analysis resolution of 8 nm and atomic percentage detection limits below 0.1 %. The coupling of an SEM with AES allowed for correlation between surface morphology and elemental composition, which

can be clearly seen in the elemental mapping of platinum features amid PMAM stamps described in Chapter 3.

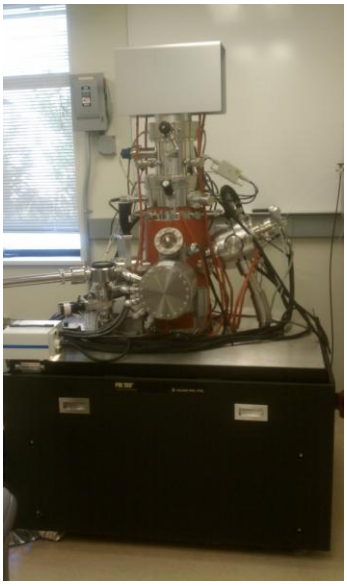


Figure 2.12. Photograph of the PHI 700 Scanning Auger Nanoprobe located in the Stanford Nanocharacterization Laboratory.

2.7. Ultraviolet-Visible(UV-Vis) Spectroscopy

2.7.1. Background

Ultraviolet-Visible (UV-Vis) spectroscopy measures the wavelength and intensity of sample absorption or reflectance of near-ultraviolet, visible and (depending on instrumentation) near infrared (NIR) radiation. Ultraviolet and visible light are energetic enough to promote outer electrons to higher energy levels. Electronic transitions in the UV-Vis and NIR range characterize the following: molecules, metal cations, complexes of metal cations and ligands, bulk solids and highly dispersed metal / metal oxide moieties with properties distinct from the bulk [171]. UV-Vis

spectroscopy was used to learn more about extinction and bandgaps of SnO_x, ZnO and ZTO thin films described in Chapters 5 and 6.

2.7.2. Theory

In UV-Vis spectroscopy, transitions between electronic energy levels result in the absorption of electromagnetic radiation over the visible spectral range. When a molecule absorbs energy, the most probable transition is from the highest occupied molecular orbital (HOMO) to the lowest unoccupied molecular orbital (LUMO) [172]. Because molecules have many possible states of vibrational and rotational excitation, electronic transitions consist of many closely-spaced energy intervals that a spectrometer outputs as a broad band of absorption centered near the wavelength of the major transition [172]. Figure 2.13shows a schematic of many possible electronic transitions with superimposed vibrational transitions.

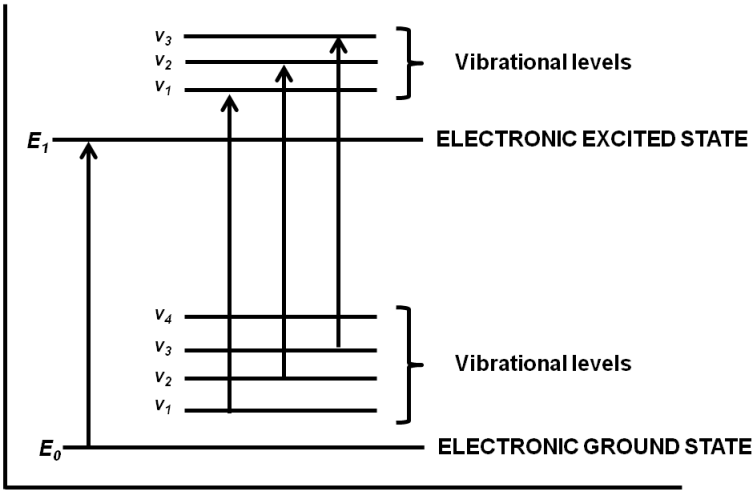


Figure 2.13. A multiplicity of electronic transitions from ground to excited states. Only vibrational states are represented as rotational levels are very closely spaced.

The Beer-Lambert Law describes the fraction of light transmitted (I) to the incident intensity (I_0) to be dependent on the path length of the light through the sample (ι), the absorption cross section of the transition (σ) and the difference in electron population (N_1 and N_0) between final and initial electronic states (E_1 and E_0, respectively). As a result, the Beer-Lambert Law may be written as shown in Equation 2.15 [172].

$$\frac{I}{I_0} = e^{-\sigma(N_0 - N_1)\iota} \qquad (2.15)$$

Equation 2.15 is based on Beer's law which is frequently written in terms of absorbance (A), the molar absorptivity coefficient of the material (ε) and the concentration of the absorbing species (ι) (Equation 2.16).

$$A = \varepsilon c l = -\log_{10}\left(\frac{I}{I_0}\right) \qquad (2.16)$$

Semiconductors, such as those materials studied in Chapters 5 and 6, are interesting for UV-Vis analysis because excitation from occupied to unoccupied levels can be affected by UV-Vis radiation. The electronic bandgap is defined as the difference in energy between the valence band maximum (VBM) and the conduction band minimum (CBM). The optical bandgap, which can be interpreted from the shape of a UV-Vis absorption spectrum, is a convenient way to estimate the electronic bandgap. These electronic transitions may be allowed or forbidden indirect or direct transitions. A direct transition may be described as a two-particle interaction between an electron and a photon, while an indirect transition may be described as a three-particle interaction (photon, electron and phonon) [171]. A transition is allowed or forbidden based on the dipole selection rules of the system [171].

While collection of UV-Vis data is relatively straightforward and convenient, determining bandgap is difficult due to significant error from factors that complicate interpretation of the spectra. J. Tauc developed a method for determining optical bandgap from interpretation of the exponential tail of the absorption edge [173] . The absorption data is fit to expected trendlines for direct and indirect bandgaps, and then a tangent line is drawn for bandgap extrapolation [173-175]. Absorbance *A* is normalized to the path length ι of light through the material, which for these studies represented the film thickness, to produce the absorption coefficient α. Equation 2.17 shows this relation:

$$\alpha\ (\mathrm{cm}^{-1}) = \frac{\ln(10)\ x\ A}{\iota(cm)} \qquad (2.17)$$

Tauc [173] and Davis and Mott [174, 175] found that values of $\alpha > 10^4 \mathrm{cm}^{-1}$ often obey the relation presented in Equation (2.18):

$$\alpha h\nu \propto \left(h\nu - E_g\right)^{1/n} \qquad (2.18)$$

where the quantity $h\nu$ is the photon energy, E_g is the optical bandgap, α is the absorption coefficient and *n* represents values of 3, 2, 3/2 or 1/2 corresponding to forbidden and allowed direct and indirect transitions as shown in Table 2.1 [176]. Plots of $(\alpha h\nu)^n$ versus $h\nu$ in which a tangent line is extrapolated to the baseline are called Tauc plots [175, 176].

Table 2.1. Value of transition type, n and description of forbidden, allowed and indirect or direct transitions.

N	**Transition**
2	Direct (allowed)
2/3	Direct (forbidden)
1/2	Indirect (allowed)
1/3	Indirect (forbidden)

When Tauc analyses are difficult, confusing or impractical, other methods of determining light extinction behavior such as spectroscopic ellipsometry (SE) may be used.

2.7.3. Equipment

UV-Vis spectrometers offer wide spectral ranges extending from UV to IR and may have diffuse reflectance configurations. Common components of a spectrometer include a light source, monochromator, long pass filters, transmission cell, diffuse reflectance sphere, focusing lenses and optical fibers. A Cary 6000i UV-Vis-NIR Spectrophotometer with a spectral range of 175 to 1800 nm was used to perform the UV-Vis data collection.

2.8. X-ray Diffraction/Diffractometry (XRD)

2.8.1. Background

X-ray diffraction (XRD) occurs when the atomic planes of a crystal causes incident monochromatic x-rays to constructively interfere with one another as they

leave the material. In materials where there is no long range periodic order, such as in an amorphous material, there will be destructive interference. Peak intensities are determined by the distribution of atoms within the lattice, and the diffraction pattern is the fingerprint of periodic atomic arrangements in a given material. Databases of XRD patterns enable convenient phase identification for many types of crystalline materials. XRD is a nondestructive means of determining crystal structure, phase, texture average grain size strain and crystal defects [2].

2.8.2. Theory

When x-rays strike an atom, its electrons will oscillate with the same frequency as this incoming beam. Where there is no long-range periodic order, such as in an amorphous material, there will be destructive interference. However, in a crystalline material, where there is order, there is a greater probability for constructive interference and there will be some well-defined x-ray leaving the samples at various directions resulting in diffraction patterns.

In 1913, English physicist father and son team William Henry and William Lawrence Bragg developed a relationship to explain why the cleavage faces of crystals appear to reflect x-rays at certain angles of incidence, θ. From their work, Bragg's law was used to explain the interference pattern of x-rays scattered by crystals as a function of angle of incidence, θ, distance between atomic layers, d, wavelength λ and n an integer as shown in Equation 2.19 and shown schematically in Figure 2.14 [177].

$$2d \sin\theta = n\lambda \qquad (2.19)$$

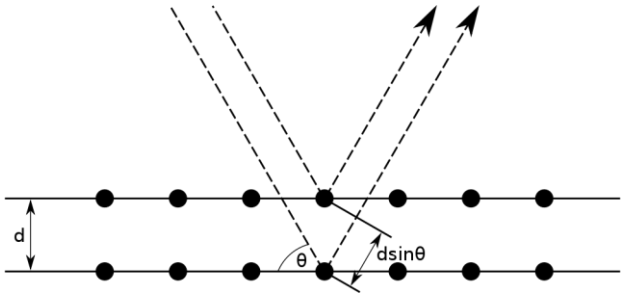


Figure 2.14. Schematic of Bragg diffraction in which two identical x-rays of wavelength λ strike a crystalline solid and are scattered from two different atoms. The path length of the lower x-ray beam is 2dsinθ. Constructive interference takes place when the path length is equal to an integer multiple *n* of the wavelength of radiation given by Bragg's law $n\lambda = 2dsin\theta$.

Bragg's law is used to describe the condition for constructive interference from crystallographic planes based on a mathematical model of a three-dimensional diffraction grating-- the Miller indices, *h,k* and *l*. Intensity of scattered waves as a function of the Bragg angle is used to generate diffraction patterns, though diffraction patterns as a function of 2θ are typically used during data analysis. When Miller indices are applied along unit cell axes *a*, *b* and *c* with axial angles α, β and γ between these axes, six different crystal classes as a function of *d* spacings can be formalized as shown in Table 2.2 [154, 177, 178].

Table 2.2. Interplanar spacings (d_{hkl}) for the seven crystal systems [179, 180].

Crystal system	**Unit cell geometry**	$\frac{\mathbf{1}}{\boldsymbol{d_{hkl}^2}}$
Cubic	a=b=c, α=β=γ=90º	$\frac{h^2+k^2+l^2}{a^2}$
Tetragonal	a=b≠c, α=β=γ=90º	$\frac{h^2+k^2}{a^2}+\frac{l^2}{c^2}$
Hexagonal	a=b≠c, α=β=90,º γ=120 º	$\frac{4}{3}\left(\frac{h^2+hk+k^2}{a^2}\right)+\frac{l^2}{c^2}$
Rhombohedral	a=b=c, α=β=γ≠90º	$\frac{(h^2+k^2+l^2)\sin^2\alpha+2(hk+kl+hl)(\cos^2\alpha-cos\alpha)}{a^2(1-3\cos^2\alpha+2\cos^3\alpha)}$
Orthorhombic	a≠b≠c, α=β=γ=90º	$\frac{h^2}{a^2}+\frac{k^2}{b^2}+\frac{l^2}{c^2}$
Monoclinic	a≠b≠c, α=γ=90º≠ β	$\frac{1}{\sin^2\beta}\left(\frac{h^2}{a^2}+\frac{k^2\sin^2\beta}{b^2}+\frac{l^2}{c^2}-\frac{2hl\cos\beta}{ac}\right)$
Triclinic*	a≠b≠c, α≠ β≠ γ≠ 90º	$\frac{\mathbf{1}}{\boldsymbol{V^2}}(\boldsymbol{S_{11}h^2+S_{22}k^2+S_{33}l^2+2S_{12}hk+2S_{23}kl+2S_{13}hl})$

* For the triclinic crystals, V represents the volume of a unit cell and the values of S_{xy} represent space groups which may be found elsewhere [179].

2.8.3. Equipment

Common components of an X-ray diffractometer include an x-ray tube, sample holder and x-ray detector (Figure 2.15). The geometry of a diffractometer is such that the sample rotates in the path of the x-ray beam at an angle θ while the detector is mounted on an arm that rotates at an angle 2θ to collect diffracted x-rays [180]. X-rays are generated in a cathode ray tube by heating a filament to produce electrons. These electrons are then accelerated toward a target by applying a voltage and bombarding the target material with electrons [178]. When core electrons are ejected from x-ray bombardment, characteristic x-ray spectra are generated.

X-ray spectra consist of several reflections with the K_α and K_β being most common. These values are specific wavelengths characteristic of the target material, which for these experiments was Cu K_α = 1.54 Å [178]. These CuK_α x-rays are collimated and directed onto the sample which produces spectra from the continuous collection of diffracted x-rays as the sample and detector rotate through their respective angles. As previously mentioned, peak intensities are the result of meeting the requirements of Bragg's law, whereby constructive interference occurs. A detector collects, records and processes signal and converts it to units of counts which is then manipulated by software to generate a plot of counts versus 2θ.

From these data, patterns may be compared to files of d-spacings and planes of reflection from the International Centre for Diffraction Data (ICDD) as powder diffraction files (PDFs) for material characterization. The x-ray diffractometer used to study the crystallographic orientation of SnO_x, ZnO and ZTO thin films described in Chapters 5 and 6, respectively was the X'Pert 2 PANalytical Materials Research Diffractometer (Figure 2.15).



Figure 2.15. Picture of goniometer, x-ray detectors and sample holder of the X'Pert 2 PANalytical Materials Research Diffractometer.

2.9. Inductively Coupled Plasma-Optical Emission Spectroscopy (ICP-OES)

2.9.1. Background and Equipment

Inductively coupled plasma optical emission spectroscopy (ICP-OES) is a bulk material analytical technique that has been used to measure elemental composition with detection limits on the order of ppb [181]. To prepare for analysis, solid samples are first dissolved in a liquid, which is typically an acidic aqueous solution. This solution is then sprayed into the core of an inductively coupled argon plasma whose temperature is so high (6000-10000 ºC) that ions become excited at element-specific electromagnetic wavelengths. This emitted light is measured using a spectrometer which yields an intensity profile that is then converted to elemental concentration based on comparisons with calibration standards [180]. Figure 2.16 shows a schematic of the process. The equipment used for ICP-OES elemental analysis was a Thermo Scientific ICAP 6300 Duo View Spectrometer**.** Elements that cannot be measured using ICP-OES are the halogens, carbon, oxygen and nitrogen.

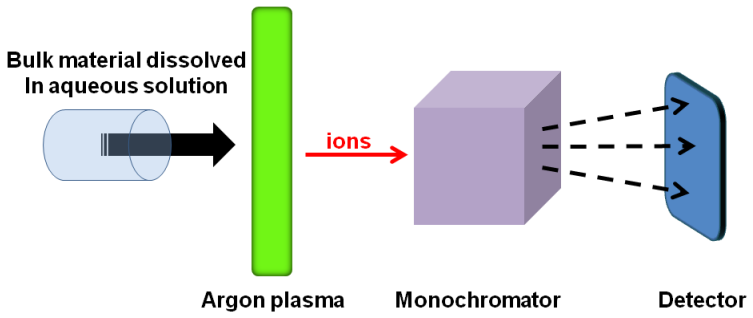


Figure 2.16. ICP-OES process schematic in which bulk material is dissolved in aqueous solution and then sprayed into a plasma so energetic that ionization takes place. A monochromator separates specific wavelengths of interest and a detector measures the intensity of the emitted light at element-specific electromagnetic wavelengths.

Chapter 3. Area-Selective Atomic Layer Deposition by Microcontact Printing with a Water-Soluble Polymer

In this chapter, the use of a water-soluble polymer for area selective atomic layer deposition (ALD) with microcontact printing (μCP) is described. Polymethacrylamide (PMAM) was spin-coated and patterned onto substrates of silicon by μCP , generating patterns down to 2 μm in size. The resist properties were tested against Pt ALD. The results show that films of Pt were grown selectively on the PMAM-free regions and significantly blocked in the presence of the polymer. Scanning electron microscopy and scanning Auger electron spectroscopy showed sharp pattern transfer of PMAM and good propagation of the pattern into the Pt layer. The PMAM layer was simply removed just by dipping in water. After the removal process, the PMAM-coated surface exhibited the same properties as the original surface. The use of PMAM as an ALD resist offers good selectivity and high spatial resolution and provides a new, convenient route toward achieving spatially patterned film growth.

3.1. Introduction

Atomic layer deposition (ALD) is one of the most promising techniques for depositing ultrathin films with high conformality for three-dimensional nanoscale device fabrication [12, 29, 182]. Because ALD is based on self-saturated surface reactions, it can produce excellent, conformal films even in complex nanostructures. Area selective atomic layer deposition (AS-ALD) is a bottom-up patterning method that takes advantage of the self-saturated surface reaction properties of ALD. Namely, modification of the substrate properties enables deposition of materials only where

needed in the additive process of AS-ALD, unlike in conventional lithography, which is subtractive [39]. To achieve substrate modification, self-assembled monolayers (SAMs) have been most commonly employed. By coating the surface through a self-assembly process, SAMs change the surface properties according to the nature of their tail group, as described in the introductory chapter [29, 39]. Until now, various SAM molecules, such as octadecyltrichlorosilane (ODTS) [38, 106, 107, 110, 150, 183-187], tetrahydrooctyltrichlorosilane [38, 107, 110], octadecyltrimethoxysilane [47, 107] and 1-octadecene [106, 110, 114] have been used in AS-ALD. In addition, the patterning of SAM molecules is important for the AS-ALD process, because the patterns of surface properties induced by the SAM coating are directly transferred into the final patterns of the deposited film. Soft lithography [38, 150, 187] photolithography [118, 188], and nanotemplating [184, 185] have each been investigated for the patterning step in AS-ALD. Among these patterning methods, the soft lithography process of microcontact printing (μCP) has been intensively studied for AS-ALD because it is an easy and effective way to make a pattern without the need for expensive tools. Because elastomeric stamps typically made of polydimethylsiloxane (PDMS) are used, the SAM coating can be applied to curved surfaces as well as planar ones [189, 190].

Though very effective at blocking the growth of ALD films, SAMs have several limitations in the AS-ALD process. In our previous research, the packing density of SAM molecules was found to be a critical factor for the ability to block film growth [38, 107, 110]. To achieve complete blocking of ALD films, the formation of densely packed SAMs is required, but this is time-consuming and requires careful control over humidity and other conditions [38, 107, 110]. In effect, these challenges present a

drawback in using SAMs as ALD resists and in integrating them into present processes for device fabrication. In addition, because the thickness of the SAM layer is in the range of a few nanometers, the lateral growth of the deposited film above the thickness of the SAM, namely a size t, can be problematic for the fabrication of nanoscale patterns [43].

Other researchers have investigated the use of polymers for the ALD resist. Many polymers offer the advantages of being inexpensive and easy to apply onto substrates by well-established methods, such as spin coating. Because polymers are not formed by molecular ordering like SAMs, the limitation with respect to the packing density of the SAMs can be avoided. Additionally, the easy thickness controllability of polymer films is beneficial for nanoscale pattern fabrication. Previous researchers have studied poly(methyl methacrylate) (PMMA) [37, 126, 191-194], poly(vinyl-pyrrolidone) [195] and poly-*tert*-butyl-methacrylate [196] for AS-ALD resist. However, the studies were mainly focused on the blocking ability of the polymer depending on the reaction chemistry [192, 193] and the feasibility of applying AS-ALD using polymers to various ALD processes [191, 195]. For patterning methods in AS-ALD, previous papers have employed conventional photolithography with a UV light source [126, 192-194]. Also, Färm et al. used atomic force microscopy to make a pattern in the PMMA polymer by localized heating [195]. Although soft lithography has shown many advantages for AS-ALD with SAMs, the patterning for polymer resists to date is still performed by conventional top-down processes.

This chapter describes PMAM as a deposition resist and applies it to AS-ALD with the soft lithography technique. The structure of the PMAM monomer is shown in

Figure 3.1. PMAM possesses water solubility as well as good thermal stability (up to 340°C) [197]. Its water solubility properties simplify the processing of the polymer and its deposition onto the substrate and may benefit its integration with existing systems and minimize hazardous waste handling [198]. Moreover, removal of the polymer resist with gentle water treatment after AS-ALD may avoid oxidation or degradation of the substrate or deposited materials in contrast with other polymer removal methods such as warm acetone solvent or O_2 plasma. The Pt process was chosen as the test system for AS-ALD. Pt has been used in a variety of applications including acting as an electrode material in fuel cell catalysts and in dynamic random access memory devices [199, 200]. Pt was also the material used in an early study of selective chemical vapor deposition with microcontact printing [201].

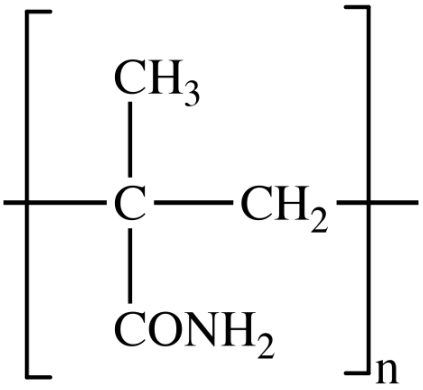


Figure 3.1. PMAM monomer**.**

PMAM was first deposited on oxide-coated silicon substrates using spin coating. The thickness of PMAM was controllable by changing the concentration of the PMAM solution, and the PMAM layer effectively blocked the Pt deposition. Based on the spin-coated PMAM results, μCP was applied to the patterning of PMAM. After AS-ALD,

the removal process of PMAM was carried out just by dipping the substrate in water to reactivate the surface. The results provide a new route for carrying out AS-ALD with a simple patterning and removal process.

3.2. Experimental Methods

All silicon sample pieces were cut from Si (001) wafers. Si wafers used for polymer stamping and spin coating, and for the IR studies of polymer removal, were purchased from Sci-Tech, Inc. The Si wafers were p-type with a boron dopant and a resistivity of 1.0–10.0 Ω-cm. .Silicon substrates were first cleaned by sonication in chloroform and a deionized (DI) water rinse. Piranha etch (volume ratio of concentrated H_2SO_4 /H_2O_2 (7:3) followed by a second DI water rinse and drying in compressed air, completed the cleaning process. A chemical oxide of silicon resulted from this treatment. PMAM was purchased from Polyscience. Water was chosen to be the solvent for the PMAM solution and a range of concentrations (0.25, 0.5, 0.75, 1.0, 1.25, and 1.5 wt %) was prepared for the purposes of spin coating. Before spin coating, the freshly cleaned Si (001) substrate was baked on a hot plate at 200°C for 2 min to enhance adhesion between the substrate and PMAM. PMAM was then applied to the Si substrates by spin coating. 30 µL of PMAM solution was transferred onto the Si (001) substrate and each sample was subjected to 5 min of spinning at 4000 rpm.

Pattern transfer of PMAM onto the Si substrates was accomplished by a previously reported standard CP procedure [39]. Conventional photolithography was used to fabricate masters on patterned Si wafers for CP. PDMS Sylgard 184, used for the casting of stamps, was purchased from Dow Corning. Masters containing two different stamp patterns were used. The first contained a grid of 500 x 500 µm squares.

When a PDMS stamp was cast from this master and inked with PMAM, these squares would be recessed and the PMAM would be transferred in regions outside the squares. The second master contained a grid of 500 x 500 μm squares in which each square possessed a mesh structure of 2–4 x 2–4 μm features. A PDMS stamp cast from this mesh master and inked with PMAM would transfer polymer outside the large squares and onto the small 2–4 x 2–4 μm features. The PDMS stamps containing 500 x 500 μm squares were sonicated in an ethanol–water mixture 7:3 = ethanol:water for 10 min before use and dried for 30 s with a stream of air. The stamps were inked in 0.5 and 1.0 wt % of PMAM solution for 5 s, air dried for 30 s, and then contacted with the Si substrates for 90 s using an external weight of 33 g. For the stamps containing the smaller features of 2–4 x 2–4 μm, the same stamping procedure was followed but with a slightly heavier weight of 43 g.

After the PMAM application, the samples were placed in an oven at 100°C and baked overnight (8–15 h) to drive off the water solvent. For the removal of PMAM, deionized (DI) water was tested as a solvent. Samples for which PMAM was coated on the Si (001) substrate by 1.0 wt % of solution were dipped in the DI water for various times and then the thickness and chemical bonding of the remaining layer were investigated using ellipsometry and Fourier transform infrared (FTIR) spectroscopy, respectively.

The PMAM-containing samples (both spin-coated and stamped), as well as silicon substrate control samples, were introduced to a custom-built, flow-type ALD reactor for the growth of Pt using the precursors $MeCpPtMe_3$ and air [39]. More information about the ALD reactor can be found in Chapter 2 and elsewhere [38, 39,

150]. Each Pt ALD run consisted of 100 cycles with a deposition temperature of 280–300°C. Both precursors were pulsed for 2 s and were separated by inert purges of 30 s. The 30 s purge time was selected to prevent chemical vapor deposition and growth on the polymer.

After the formation of PMAM films, the thicknesses of the resulting PMAM films were measured by a Gaertner Scientific Corp. L116C He–Ne ellipsometer. Following ALD, samples were characterized with several analytical techniques, including X-ray photoelectron spectroscopy (XPS), scanning electron microscopy (SEM) and scanning Auger electron spectroscopy (AES). XPS analyses were performed using the PHI VersaProbe 5000 Scanning XPS and the SSI S-Probe Monochromatized XPS Spectrometer, both using Al Kα radiation with an X-ray monochromator. The C 1s peak at 285.0 eV was used as a reference. The FEI XL30 Sirion SEM with field-emission gun (FEG) source was used to image stamped surfaces. Auger survey scans and elemental maps were taken with the PHI 700 Scanning Nanoprobe. A Nicolet 7600 FTIR was used to probe for the removal of the polymer by following the presence of key IR absorption peaks indicative of PMAM. Spectra were acquired in transmission mode with a mercury–cadmium–telluride detector at a resolution of 4 $cm.^{-1}$

3.3. Results and Discussion

3.3.1. PMAM Formation by Spin Coating

To explore the basic coating characteristics, the application of PMAM was carried out by spin coating. Using various concentrations of PMAM solution, the thicknesses of the PMAM layers were measured by ellipsometry. The thickness linearly increases as a function of PMAM concentration, as shown in Figure 3.2. Because the PMAM solution becomes more viscous with increase in concentration, the thickness of the resulting

PMAM film increases. In addition, the PMAM films showed uniform color over the entire surface, indicating that the film thickness is uniform, which is consistent with the small range of thickness deviation measured by ellipsometry. The formation of PMAM films with controllable thicknesses up to 250 Å could be achieved by spin coating.

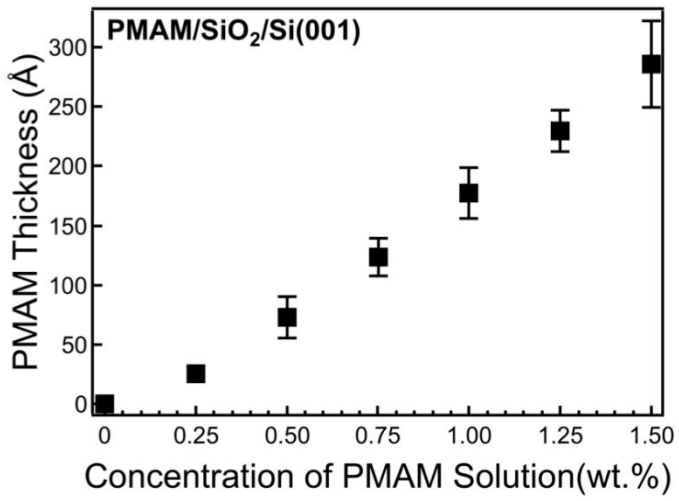


Figure 3.2. PMAM film thicknesses as a function of PMAM concentration. (Error bars on spin-coated samples represent one standard deviation over five locations per sample. For 1 wt %, five samples were separately fabricated and its error bar is representative of sample-to-sample variation.)

By controlling the solution concentration, films of different thickness were deposited on SiO_2 substrates to determine the minimum PMAM thickness for blocking Pt ALD. Substrates with various thicknesses of PMAM were prepared by spin coating, and then the Pt ALD process was carried out for 100 cycles. Figure 3.3 shows the amount of Pt quantified by XPS measurement as a function of PMAM thickness. Even with 25 Å of PMAM, Pt was not observed within the detection limit of the XPS analysis Pt atom % 0.1 to 0.2%, indicating that the PMAM thin film effectively blocks Pt deposition. Hence, for PMAM film thicknesses of 25 Å or higher, Pt ALD was blocked. In our previous paper, ODTS as a resist required formation times of over 12 h to effectively block Pt deposition [38].

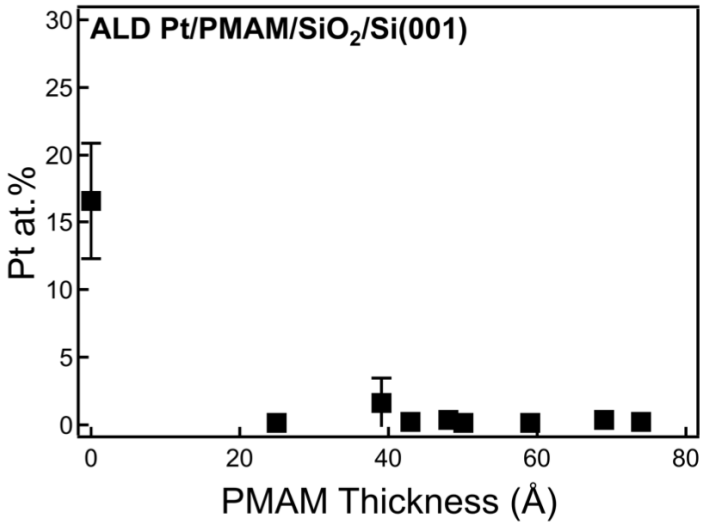


Figure 3.3. Pt atomic percentage from XPS as a function of PMAM thickness following spin coating on a Si substrate. (Error bars on each sample represent one standard deviation over three location per sample.)

For the blocking process of AS-ALD using SAMs, the formation of densely packed SAMs is required because defects and pinholes in loosely packed SAMs become weak points against the nucleation of ALD film. Compared to the ODTS SAM, a PMAM polymer film of similar thickness formed by spin coating for 5 min shows equivalent blocking ability. This indicates that the PMAM layer is much more densely packed than ODTS after evaporation of the water solvent during spin coating.

Several ALD processes showed no deposition selectivity on hydrophobic polymer-coated and uncoated regions [126, 191-193, 195]. It was believed that nucleation occurs from diffused precursors inside the polymer because precursors diffuse easily into relatively porous polymers. Sinha et al. reported that TiO_2 was deposited on PMMA only from $TiCl_4$ and water but not from $Ti(ipr)_4$ and water because of the difference in diffusivity from differences in molecular size of the two precursors. Therefore, thicker polymer films over 150 nm were required to prevent deposition of

TiO_2. In other papers, two Al_2O_3 ALD processes from $Al(CH_3)_3$ and $AlCl_3$ as a precursor and water as a reactant were applied to AS-ALD with polymer. When PMMA was used for the deposition deactivator, the amount of Al_2O_3 from $AlCl_3$ was larger than that from Al $(CH_3)_3$ and when poly4-vinylpyridine was used, it showed the opposite trend. Therefore, our ALD blocking results indicate that the Pt precursor does not diffuse into PMAM even for thicknesses below 3 nm. The ability of PMAM to prevent Pt nucleation may stem from either a low diffusivity of the Pt precursor in PMAM or from the fact that this ALD process does not use H_2O as a reactant, in contrast to the other systems, because water uptake in the polymer could contribute to growth [126, 191-193, 195]. Further studies should be carried out to determine the extendibility of the PMAM polymer to other AS-ALD systems.

3.3.2. Patterning of PMAM by µCP

Based on the PMAM coating characteristics and blocking properties achieved by spin coating, the formation of PMAM films was studied using µCP. Similar to the case of spin coating, the thickness of PMAM as a function of concentration was examined to determine the optimal aqueous solution condition. Also sampled during these experiments was the printing time, which is the length of time the stamp is in contact with the substrate. Figure 3.4 shows the thickness of PMAM with concentration and printing time using an unpatterned (blanket) stamp. Apparently, the thickness increases with increasing concentration of PMAM solution, which is consistent with the results from spin coating. The increase in the thickness is significant with longer printing time. Longer printing times resulted in thicker films. This trend became more dramatic with higher concentrations of PMAM, especially for 1.0 wt %. The PMAM thicknesses at the substrate after blanket µCP ranged from below 100 to over 400 Å.

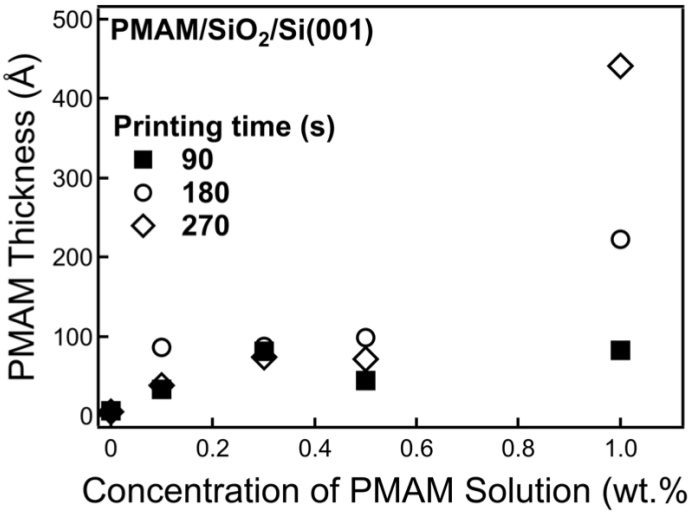


Figure 3.4. PMAM film thicknesses as a function of PMAM concentration from µCP**.**

Once the conditions for Pt ALD blocking were determined from the blanket PMAM stamping studies, investigations of PMAM patterning using AS-ALD were carried out. PMAM concentrations between 0.5 and 1.0 wt % were used to achieve film thicknesses exceeding 50 Å for the AS-ALD experiments. PDMS stamps of both 500 x 500 and 2–4 x 2–4 μm patterns were inked with the polymer solution and transferred to the Si substrate. Figure 3.5 shows SEM images following stamping of the PMAM solution onto the substrate. The brighter regions in Figure 3.5a correspond to the presence of the 50 Å thick PMAM polymer film. In Figure 3.5c, the PMAM appears as the darker features. Sharp pattern transfer was observed for both stamp patterns and, apparently, patterned areas were completely wetted by the PMAM. Stamping the larger features was significantly easier than the smaller features, for which more care was needed to apply uniform pressure of the inked stamp to the substrate and during stamp removal. SEM measurements were also made after Pt ALD on the PMAM-patterned substrates, as shown in Figure 3.5b and d. Both images show retention of the stamped pattern and the larger pattern image shows inversion of the contrast.

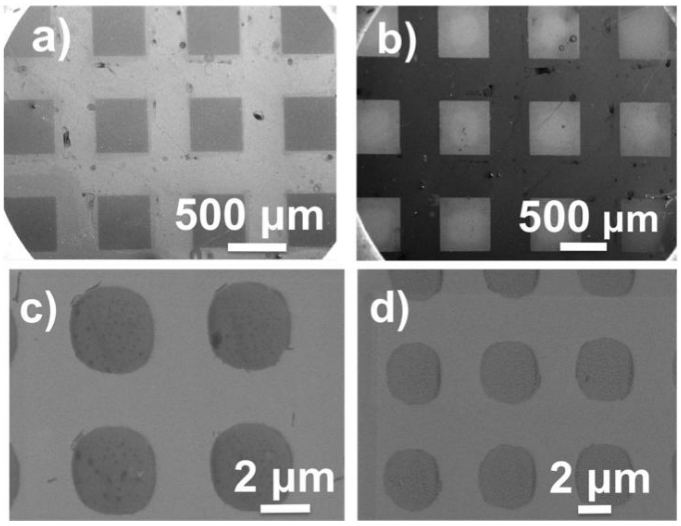


Figure 3.5. SEM images of [(a) and (b) 500 x 500 PDMS stamps and [(c) and (d)] 2–4 x 2–4 µm stamps before and after 100 cycles of Pt ALD.

Elementally specific analysis provides more detailed information on the AS-ALD results. The results of scanning AES taken after Pt ALD on a patterned sample with 2–4 µm features are shown in Figure 3.6. Figure 3.6a is an SEM image taken in the AES system, and Figure 3.6b contains the Pt AES elemental mapping image, acquired by measuring the intensity of the Pt AES peak as a function of beam position. The maps show the relative elemental distributions (peak intensity) as pixel intensity, where the bright regions in Figure 3.6b indicate the presence of Pt, whereas the dark areas indicate the absence of Pt. The lateral resolution of the scanning AES is 10 nm. The images clearly show the Pt has deposited in the regions without PMAM and that the pattern is largely retained. Consistent with the SEM image of Figure 3.5c, Figure 3.6a indicates that for the 2–4 x 2–4 µm features, PMAM transferred has sharp and well-defined edges. Although the feature edges are sharp, they are not perfectly formed, as seen by the small defects within parts of the transferred material. Compared to spin coating, these defects are probably due to the relatively low packing density. Because

the solution of PMAM is transferred onto the substrate via an elastomeric PDMS stamp, the uniformity in the distribution of the PMAM solution on the stamp may be lower than that in spin coating.

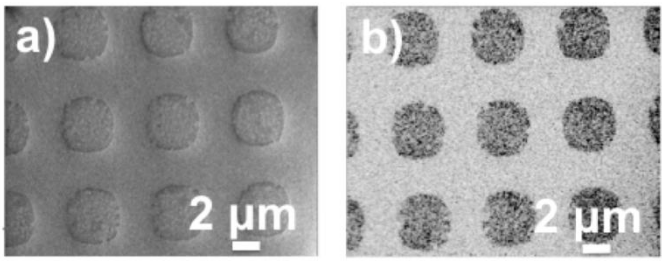


Figure 3.6. SEM and scanning AES Pt elemental map of 2–4 x 2–4 µm stamps following 100 cycles of Pt.

To first order, the maximum resolution of µCP patterning depends only on the resolution of the stamp and the stamping process. Although µCP is a simple process, high resolution down to tens of nanometers has been achieved according to literature [202]. This result indicates that the current process of AS-ALD can be used at the submicrometer scale. However, size effects from isotropic growth of ALD films may ultimately limit the resolution when the minimum feature size is comparable to the thickness of the deposited film [43].

3.3.3. Removal of PMAM

Because PMAM is applied in an aqueous solution, these solubility properties of PMAM also suggest the possibility for easy removal of PMAM after the AS-ALD process is completed. To determine whether PMAM can be removed from the substrate after processing, the PMAM layer removal process in water was studied. PMAM layers were prepared by spin coating with the same process used for AS-ALD and dipped in DI water in separate experiments of 0, 0.5, 1, 2 and 3 h. Figure 3.7a shows the

thickness change in PMAM with various dipping times in water. The thickness of the PMAM layer rapidly decreases within 0.5 h of dipping time and reaches a nearly constant value below 20 Å for longer times. The IR data shown in Figure 3.7b present a progression of DI water dipping times compared to the as-deposited PMAM layer. The IR spectrum of the as-deposited PMAM layer shows characteristic absorption peaks including the carbonyl stretching mode typically found at 1690 cm^{-1} and the amide bands at 1600 $cm.^{-1}$ In addition, a peak at 1100 cm^{-1} is observed, assigned to a Si–O–Si stretch originating from the SiO_2-coated Si substrate.

Figure 3.7b shows that after 1 h of dipping time, the key IR absorption modes for PMAM become attenuated, indicating that almost all the PMAM layers dissolve in the water, consistent with the thickness change data. After 3 h of dipping in water, the carbonyl and amide peaks are significant within the experimental signal to noise. Because the spectra are obtained by subtracting the transmittance of the sample after the process from that before the process, the changes in the Si–O–Si stretching peak at 1100 cm^{-1} peak after water dipping reflect slight differences in the thicknesses of SiO_2, which is sensitive to spatial variations in the measurement. The residual thickness that remained below 20 Å is probably due to an increase in SiO_2 thickness.

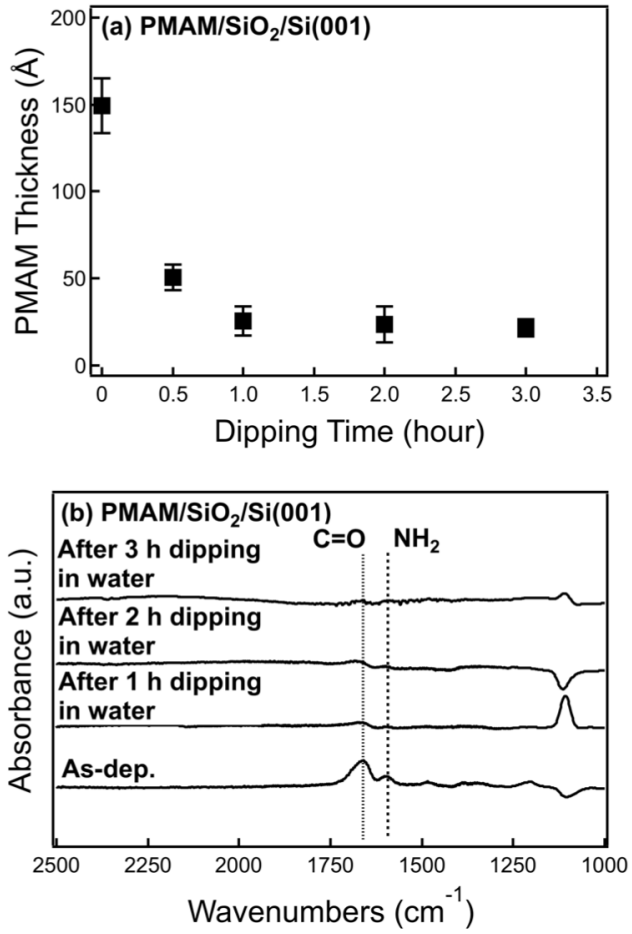


Figure 3.7. (a) PMAM film thicknesses measured by ellipsometry and (b) IR spectra during removal of PMAM as a function of dipping time in water. (Error bars represent one standard deviation over five locations per sample.)

After removal of the PMAM layer, the degree of reactivation of the surface was studied by examining its ability to block Pt ALD. The sample dipped in water for 3 h was loaded into the chamber together with PMAM-coated and uncoated samples for comparison. Figure 3.8a shows the Pt XPS core-level spectra after 400 cycles of Pt ALD for the three samples. Two XPS peaks were observed at the same binding energies, 71.0 and 74.4 eV, from the reactivated and uncoated samples. The low and high binding energy peaks correspond to pure metallic Pt $4f_{7/2}$and Pt $4f_{5/2}$, respectively[203]. In contrast, a negligible Pt XPS signal was detected from the PMAM

film after a high number of cycles (400). I n the N XPS core-level spectra, there is no detectable peak from the uncoated and reactivated samples, as shown in Figure 8b. From the PMAM-coated sample, a N peak was observed at 399.6 eV, which is consistent with previous XPS results on PMAM [204]. The reactivated sample obtained by dipping in water shows the same deposition characteristics of Pt with that of an uncoated sample, indicating that PMAM is completely removed by the water solvent.

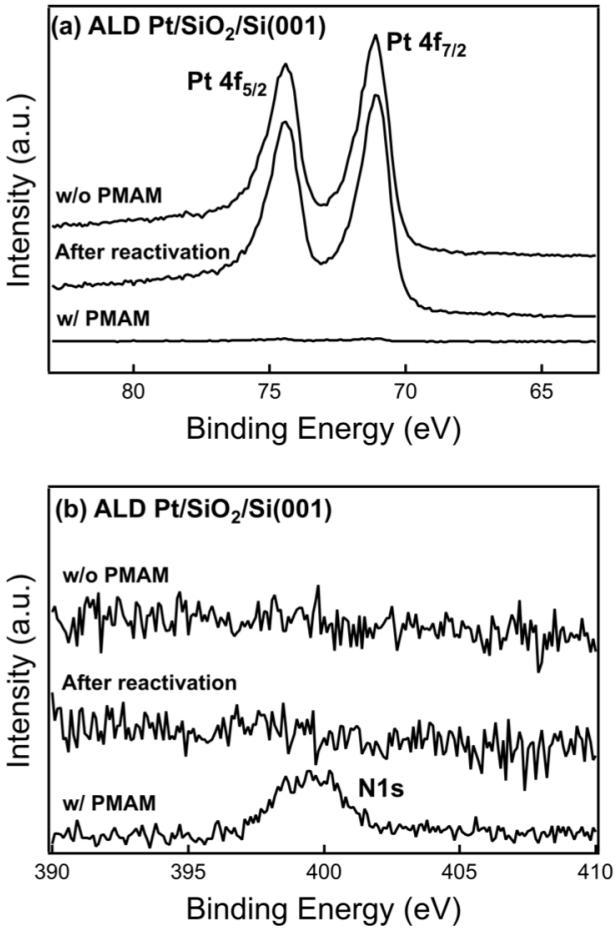


Figure 3.8. XPS spectra in (a) Pt and (b) N core levels obtained from PMAM-coated, uncoated and reactivated samples after Pt ALD for 400 cycles. The reactivated samples was prepared by dipping a PMAM-coated sample in water for 3 h.

3.4. Conclusions

In this chapter, the water-soluble polymer (PMAM) is a potential resist for Pt AS-ALD. The PMAM layer can be easily fabricated by spin coating, and its thickness is controllable by changing the concentration of the aqueous PMAM solution. Compared to reported studies of ODTS SAMs, PMAM showed effective blocking properties as well as short application time. μCP was used to transfer PMAM patterns onto substrates. Following Pt ALD, Pt growth was mostly limited to the PMAM-free regions. AS-ALD of Pt using PMAM showed good selectivity and a high spatial resolution. Improvements to the μCP method ensure even greater selectivity and make it a very attractive alternative to traditional lithography. The PMAM layer was simply removed just by dipping in water. After 3 h dipping, the PMAM layer was completely removed and Pt films were formed by ALD on this reactivated substrate. The use of PMAM as an AS-ALD resist provides a new, convenient route toward achieving spatially patterned film growth. The published manuscript describing this working can be found in Ref. 43 [42].

Chapter 4. Nucleation-Controlled Growth of Nanoparticles by Atomic Layer Deposition

In this chapter, a method for growing metal nanoparticles (NPs) by atomic layer deposition (ALD) with the ability to vary aerial density and NP size using nucleation control is demonstrated. Self-assembled monolayers (SAMs) pre-adsorbed on the substrate serve as a template for subsequent growth of the NPs by ALD. Defects in the SAM resulting from incomplete formation time in solution are shown to act as nucleation sites for Pt. The strategy is demonstrated experimentally using ALD of Pt from a metal organic Pt precursor and dry air as the counter-reactant on silicon dioxide surfaces pretreated with octadecyltrichlorosilane SAMs. The aerial density and mean diameter of the Pt NPs are controlled by changing the SAM dip time and the number of ALD cycles.

4.1. Introduction

Metallic nanoparticles (NPs) possess interesting properties[205, 206]. The small size and high surface-to-volume ratio of NPs are responsible for chemical, physical, electrical, and mechanical properties that do not exist on larger length scales. NPs are being pursued for many applications including optical tags [206, 207] sensors [208, 209], lasers [210, 211], photovoltaics [212-216] and catalysts [217-219]. In the case of catalysis, the spatial distribution of NPs, together with particle size and composition, are important considerations for increasing reactivity [220].

Atomic layer deposition (ALD) provides excellent capabilities for depositing a variety of materials in high surface area supports including those that are highly

structured [221-225] and is proving to be a useful method for depositing NPs as well. Since ALD comprises self-saturating surface reactions, in an idealized model, the resulting film is deposited in a layer-by-layer manner so that ALD leads to growth of a continuous film even after just the first few cycles. In reality, however, deviations such as island growth and nucleation delay may be observed. Although ALD has been traditionally used to deposit thin films, previous work has suggested that ALD can be applied to fabricate discrete NPs by exploiting these deviations [226, 227]. For example, various metals, such as Ru, Pt, Pd, and Co, have been intensively investigated for NP fabrication by ALD [228-232]. However, the characteristics of ALD over the initial growth regime, including nucleation delay and island growth, have not been well studied fundamentally.

The growth characteristics during ALD can be further modified by changing the properties of the substrate surface. This possibility has been nicely demonstrated in work on area-selective ALD (AS-ALD) [29, 117, 233, 234]. An extension of ALD that has been developed to carry out bottom-up patterning, AS-ALD commonly uses self-assembled monolayers (SAMs) to change the surface properties spatially such that the SAM acts to inhibit deposition during ALD. In previous papers, the Bent Research Group has shown that the SAMs may interfere with the ALD process through a dual mechanism: (1) the head groups react with the active sites (−OH groups) on the substrate making them unavailable for ALD chemistry, and (2) the packed hydrophobic tails prevent ALD precursors from accessing any remaining active sites at the substrate without contributing any active functionalities themselves [107]. In addition, studies have shown that a minimum time is required to form defect-free SAMs for AS-ALD,

and if the formation time is shorter, discrete NPs may form in resultant defect sites [39]. For AS-ALD, defective SAMs are undesirable since they reduce selectivity; however, these defects also provide a model system for studying NP nucleation during ALD.

In the studies described in this chapter, the possibility of using the defect sites in SAMs to control NP formation by ALD is explored. The density of defect sites in SAMs can be controlled by varying their formation time from solution, with defect density decreasing with time (Figure 4.1a) [235-239]. Since nucleation occurs at these defects, it is proposed that, by controlling the dip time in the SAM precursor solution, NP aerial density can be controlled as shown in Figure 4.1b. Furthermore, it is proposed that, by changing the number of ALD cycles, the mean NP size can be varied (Figure 4.1c). In this chapter, the chemical properties of how the substrate surface can direct the Pt ALD nucleation process to obtain growth of particles rather than a continuous film is demonstrated. Furthermore, surface functionalization of the substrate is shown to provide a nucleation and growth template allowing for the control of the spatial dispersion and size of the NPs. In this way, a tunable method for fabricating NPs by ALD is introduced.

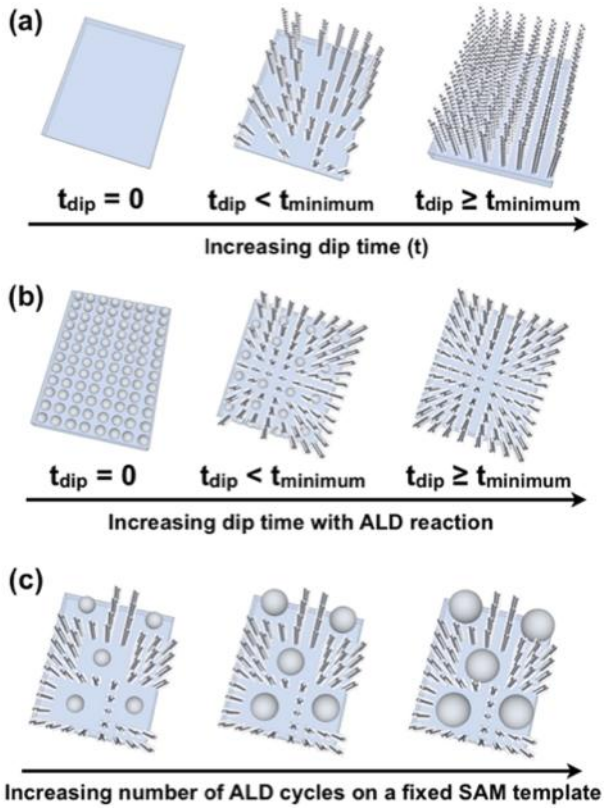


Figure 4.1. Schematic illustration of the hypothesized SAM-directed growth of Pt NPs with control over aerial density and particle size. (a) Behavior of the SAM with increasing dip time. (b) Decrease in NP aerial density with increasing SAM dip time. (c) Increase in NP size with increasing number of ALD cycles for a constant SAM template.

4.2. Experimental Methods

Octadecyltrichlorosilane (ODTS) (90%) and toluene were purchased from Sigma-Aldrich. All silicon sample pieces were cut from Si(100) wafers (Sci-Tech Inc.). Before SAM growth on silicon substrates, the substrates were first pre-cleaned by sonication in chloroform followed by a DI water rinse. A piranha cleaning (volume ratio of concentrated H_2SO_4/H_2O_2 of 7:3) followed by a second DI water rinse and drying in compressed house air completed the cleaning process. A chemical oxide of silicon resulted from this treatment. ODTS SAMs were deposited on piranha-cleaned

silicon samples at room temperature in a low-moisture glovebox that was continuously purged by dry air. Immersion times ranged from 0 to 12 h, selected based on previous work over this interval [107]. After immersion in the SAM solution, SAM growth was quenched in the following way: (1) immersion into toluene for 5 s, (2) drying with a stream of house air for 10–30 s depending on sample size, (3) immersion into chloroform for 5 s, and (4) drying with a stream of house air for 10–30 s depending on sample size. To prevent degradation from water vapor in the atmosphere, samples were then placed in a desiccator until later analysis. The thicknesses of the resulting films were determined by ellipsometry (Gaertner Scientific Corp. L116C He–Ne Ellipsometer) and compared against a piranha-cleaned control. Surface hydrophobicity of ODTS-coated substrates was measured by a static water contact angle measurement system (FTA 2000 Dynamic Contact Angle Analyzer) and was also compared to a bare control sample.

The ODTS-coated samples with dip times ranging from 0 to 12 h were introduced into an ALD reactor for subsequent Pt ALD. The Pt ALD process was carried out between 280 and 300 °C using (methylcylopentadienyl)trimethylplatinum ($MeCpPtMe_3$) and dry air as precursors for a various number of ALD cycles. Precursors were pulsed for 2 s and were separated by inert gas purges of 30 s. The chamber base pressure was below 40 mTorr, and the precursor sample vial temperature was kept at 50 °C. Precursor exposure time, reactant exposure time, and purging time were 2, 2, and 8 s, respectively. More details about the ALD reactor can be found in a previous publication [38] and in Chapter 2.

Following ALD, samples were characterized by several analytical techniques, including XPS, SEM, and scanning Auger electron spectroscopy (AES). XPS analyses were performed using the PHI VersaProbe 5000 Scanning XPS and the SSI S-Probe Monochromatized XPS Spectrometer both using Al Kα radiation with an X-ray monochromator. The C1s peak at 285.0 eV was used as a reference. Auger survey scans and elemental maps were taken with the PHI 700 Scanning Nanoprobe. The FEI XL30 Sirion Scanning Electron Microscope with FEG source was used to image surface morphology. NP size and density were determined using ImageJ software. The plan-view SEM images of NPs were converted into threshold images to define the NPs. Resulting graphical information on the NPs, such as diameter, area, and number of NPs, was extracted. Nanoparticles on the edges of the image were excluded from the graphical analysis.

4.3. Results and Discussion

Pt NP formation by ALD was controlled by changing the defect site density, as described schematically in Figure 4.1b. Visual confirmation of NP aerial density and diameter as functions of dip time and number of ALD cycles is available from the SEM images presented in Figure 4.2.

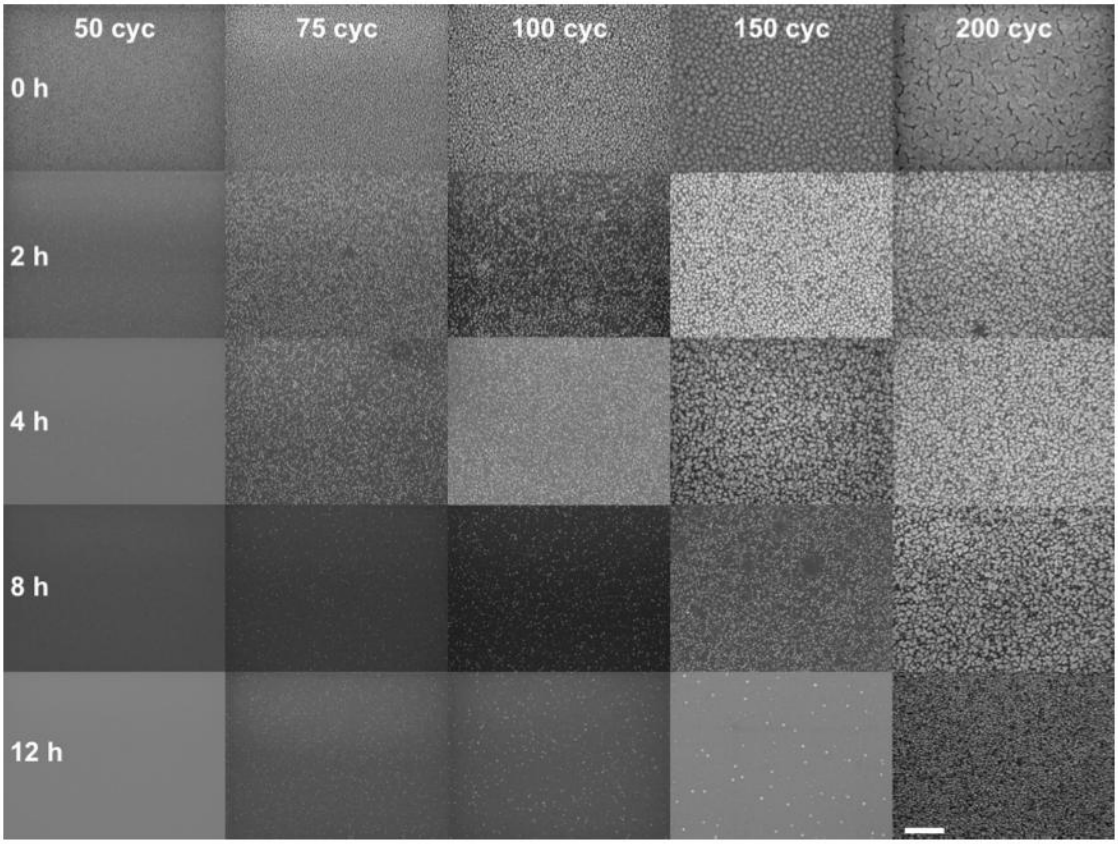


Figure 4.2. SEM images of Pt nanoparticles (NPs) grown by ALD for a variety of ODTS dip times and number of ALD cycles with 200 nm scale bar.

Figure 4.3a and b show the measured mean diameter and aerial density of the NPs as a function of SAM dip time followed by 50 cycles and 100 cycles of Pt ALD, respectively. After 50 Pt ALD cycles, the mean diameters of the NPs show a nearly constant value of 5 nm in Figure 4.3a irrespective of dip time. Similarly, the mean diameters of the NPs after 100 cycles of Pt ALD are almost constant between 2 to 12 h of dip time, as shown in Figure 4.3b. However, the mean diameters were larger (7 nm) after 100 ALD cycles compared to 50 ALD cycles. In contrast to the NP mean diameters, which were largely insensitive to SAM dip time, the NP density varied with SAM dip time. As seen in Figure 4.3a, the aerial density of the NPs after 50 cycles decreased rapidly when dip times were increased from 0 to 2 h, then exhibited a slower

decrease upon further dip time up to 12 h. Although the data points for aerial density after 100 ALD cycles are more scattered, the overall trend of the plot also shows a decrease in density with increasing dip time.

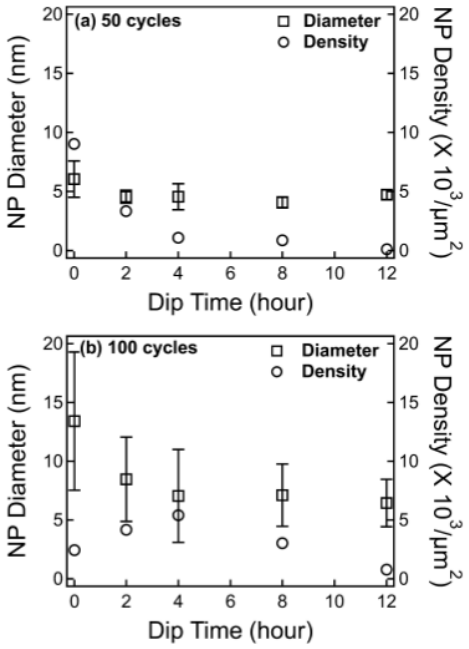


Figure 4.3. Mean Pt NP diameter and aerial density versus dip time of ODTS, for (a) 50 cycles and (b) 100 cycles of Pt ALD following the ODTS treatment. The NP diameter and NP density were measured from the software analysis by using SEM images. All corresponding SEM images can be found in Figure 4.2.

The experimental results suggest that while NP diameter is not a function of dip time, while the NP density is. These observations can be understood in the context of the proposed model of nucleation at SAM-coated surfaces. Since the ODTS coating removes active nucleation sites for Pt ALD, nucleation will occur primarily at defects on the SAM. These defects arise from vacancies or openings in the SAM layer that expose unprotected active sites at the surface upon which Pt nucleation can occur. Moreover, the size of the defect and the number of defect sites in imperfectly formed SAM layers should affect the Pt NP size and density, respectively. However, previous research on initial formation of ODTS on SiO_2 by AFM analyses indicates that the

effect of defect size should be insignificant in this system. Specifically, the studies showed that ODTS displayed an island-like surface morphology after a dip time of just 1 min and 90% surface coverage by the SAM layer after two minutes [236, 240]. In previous reports, even after 2 h of dip time, a surface coated with ODTS shows the maximum contact angle, indicating the formation of a densely packed, hydrophobic ODTS layer [150, 186, 241]. As a result, the defect sites in the ODTS layer under the current coating conditions can be considered zero-dimensional point defects rather than two-dimensional defects. Consequently, only the defect density should be changing significantly with increasing dip time, and for the same number of Pt ALD cycles, the density of Pt NPs will change, while the diameter will not. This expectation is consistent with the experimental results presented in Figure 4.2 and Figure 4.3.

In addition to the effect of SAM coverage, we also investigated the effect of ALD cycle number. The relationship between NP diameter and aerial density with ALD cycle number was studied by subjecting samples with a fixed ODTS SAM dip time to a range of Pt ALD cycles (the scheme in Figure 4.1c and Figure 4.2). An analysis of Pt NPs deposited on ODTS-free surfaces was conducted for comparison. Figure 4a–e shows the mean Pt NP diameter and aerial density determined by SEM analysis (images presented in Figure 4.2), as well as the Pt atomic percentage determined by XPS, for post-ALD samples with 0, 2, 4, 8, and 12 h of ODTS dip time, respectively. The data point at 200 cycles on the ODTS-free surface was excluded due to the continuous, film-like morphology of Pt ALD under these conditions (see Figure 4.2). It is evident from Figure 4.4 that the mean NP diameter and the Pt atomic percentage both monotonically

increase with the number of ALD cycles. In addition, the slopes of the functions for NP diameter versus ALD cycle gradually decrease with increasing dip time.

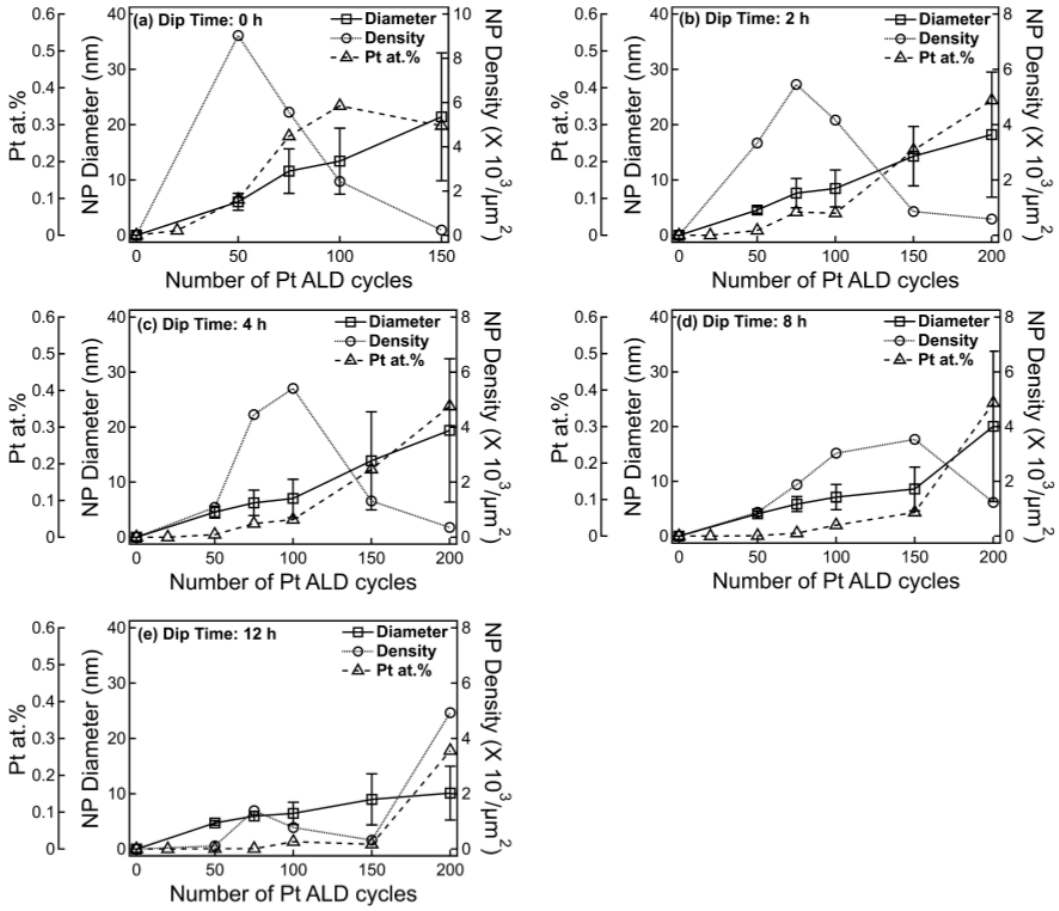


Figure 4.4. Pt NP diameter, density and atomic percent with changing number of ALD cycles on surfaces coated with ODTS for various dip times, (a) 0, (b) 2, (c) 4, (d) 8 and (e) 12 h. The NP diameter and NP density were measured from the software analysis by using SEM images (Figure 2). Pt atomic percent was obtained using XPS quantification. The error bars on the diameter data makers indicate the distribution of particle sizes.

In contrast to the NP diameter and Pt atomic percentage, the aerial density of Pt NPs reaches a maximum value at a certain number of ALD cycles then continuously decreases with increasing cycle number. Interestingly, the ALD cycle where the maximum density is observed changes with increasing ODTS dip time. For the ODTS-free surface (0 h dip time), the maximum density is observed at 50 cycles as shown in

Figure 4.4a. Subsequently, the ALD cycle number at which the highest density occurs increases from 75 to 100 to 150 cycles for 2, 4, and 8 h dip times, respectively. No decrease in the aerial density was observed on the 12 h dip time surface, as seen in Figure 4.4e.

On the basis of the results in Figure 4.3 and Figure 4.4, it is clear that the density of Pt NPs can be controlled in two ways: by changing ODTS dip time or ALD cycle number. Interestingly, changing the ALD cycle number provides a more sensitive degree of control because the range of dip times that exhibit good control over the density is narrow, as shown in Figure 4.3a. In terms of size dispersion, the NPs deposited under influence of the SAM show a narrower size distribution than that without the SAM. With the SAM, 50% of the Pt NPs are distributed within ±2 nm of the mean diameter. Although conventional solution methods are capable of producing finer size control of NPs, with deviations below 1 nm [242-244], the current method does allow better NP size control than using ALD without a SAM [245, 246].

Several insights into the ALD nucleation behavior can be gained from the data in Figure 4.4. The increase in mean diameter of the NPs with the number of ALD cycles is expected based on the growth in a cyclic manner. However, the increase in aerial density with the number of ALD cycles does not follow immediately from the models in Figure 4.1 and therefore requires further consideration. This aerial density increase indicates that Pt NPs nucleate throughout the ALD process. Several models can lead to nucleation that occurs throughout the ALD cycles, such as the presence of a constant (finite) nucleation rate anywhere in the SAM, or generation of new defects (i.e., nucleation sites) caused by the ALD process. With continuing nucleation, particles that

begin nucleation earlier in the process will be larger, while those that begin later in the process will be smaller, resulting in a wide range of sizes. This prediction is borne out by the data.

The size distribution data, indicated by the error bars in Figure 4.4, show that the range of Pt NP sizes also increases with an increased number of ALD cycles. The comparison between results on the ODTS-coated and ODTS-free substrates also provides insight into the Pt ALD nucleation and growth process. Although the mean diameters at 50 cycles show only a modest increase for the 0 h dip time sample (6.1 nm) relative to the 8 h dip time sample (4.1 nm), the density for the 0 h dip time sample is much larger than either the 8 h dip time or any sample in which ODTS is present. This result indicates a much higher nucleation site density on the ODTS-free surface, which is expected since the ODTS SAM acts to block nucleation. Moreover, the behavior at higher than 50 ALD cycles on the ODTS-free (0 dip time) surface, in which the NP aerial density decreases, is attributed to coalescence of the NPs due to the short distance between individual NPs.

The same effect exists for SAM-coated surfaces, but coalescence takes longer (more ALD cycles) to occur as indicated by the position of the maximum in the density versus cycle number curve. The nucleation site density, as well as the different surface properties between ODTS-coated and ODTS-free surfaces, probably affect this coalescence. In concurrence with the model of NP coalescence, the SEM images show that the Pt NPs are no longer circular but are irregular in shape at higher cycle numbers (Figure 4.2). In addition, the size distribution of Pt NPs is narrower on an ODTS-coated substrate than on an ODTS-free substrate. Interestingly, the mean NP diameter and size

distribution (given by the length of the error bars on the diameter data) increase at the same time the density is decreasing.

The trend mentioned above for smaller diameter particles forming on the ODTS-coated surfaces may be due to two possible explanations: inhibition of Pt NP growth by the ODTS coating or slower Pt nucleation in the presence of ODTS. In the first case, because ALD Pt nucleates on point defect sites in the ODTS layer, the growth of Pt NPs may be laterally influenced by surrounding ODTS molecules, in turn affecting the NP diameter. It is noted that, since Pt NPs are formed on the point defects at the interface between the ODTS SAM and the SiO_2 surface, any lateral inhibition of growth of Pt by the ODTS should end once the Pt thickness exceeds the height of the SAM layer, which will be no greater than the length of the ODTS molecule (2.7 nm) [247]. Moreover, as described in the experimental methods section, the growth rates obtained from the fitting are almost constant and consistent with the reported value of 0.05 nm/cycle, irrespective of ODTS coating, indicating that ODTS does not significantly inhibit Pt NP growth. In the second case, if Pt NP nucleation is slower, nucleation will tend to occur later in the ALD cycles, and the size of Pt NPs on the ODTS-coated surface will be smaller than that on the ODTS-free surface.

From the experimental data, growth characteristics of Pt NPs consistent with limited nucleation sites as a result of the ODTS coating are observed. It is found that the size and aerial density of Pt NPs depend on dip time and number of ALD cycles. In addition, the growth characteristics of Pt NPs on SAM-coated substrates cannot simply be inferred from characteristics on ODTS-free surfaces. The data clearly suggest that additional considerations for nucleation are needed. As a result, Dr. Han-Bo-Ram Lee

developed a mathematical model to describe the growth behavior of Pt NPs, and the model and its fitting to experimental data are explained elsewhere [248].

4.4. Conclusions

In this chapter, it was shown that the surface modification with a SAM can be used to obtain the growth of particles rather than a continuous film by ALD. SAM defect sites act as nucleation centers for deposition, and varying the ODTS SAM defect density through substrate dip time results in control over the density of deposited NPs by Pt ALD. For a fixed number of ALD cycles, the mean diameter of Pt NPs is not changed, but the aerial density is decreased with increasing dip time. As the number of ALD cycles increases, the diameter of Pt NPs increases on ODTS-coated surfaces with the same dip time. This approach is significant, as it allows for a degree of control over nanoparticle density and size.

Chapter 5. Tin Oxide Atomic Layer Deposition from Tetrakis(dimethylamino)tin and Water

Due to the abundance and usefulness of tin oxide for applications such as transparent conductors, sensors and catalysts, it is desirable to establish high quality atomic layer deposition (ALD) of this material. ALD allows for uniform, conformal coating of complex topographies with ultrathin films and can broaden the applicability of tin oxide to systems such as nanostructured solar cells. The present work examines the ALD of tin oxide by means of the precursor tetrakis(dimethylamino)tin (TDMASn) and water as counter-reactant. Low temperature growth in the range of 30 to 200 ºC on Si(100) and glass substrates is studied. It is found that the growth rate increase with reduced temperature, up to ~2.0 Å/cycle at 30 ºC, as compared to 0.70 Å/cycle at 150 ºC. The ALD process is established to be saturated even at the lowest temperature studied, for which the film contamination levels are below the detection limits of X-ray photoelectron spectroscopy. As-deposited films are smooth (rms roughness of 33 Å for a 460 Å thick film deposited on Si at 150 ºC) and amorphous according to X-ray diffractometry. However, post-annealing to 600 ºC in nitrogen leads to the formation of polycrystalline rutile SnO_2. The optical constants obtained from variable angle spectroscopic ellipsometry suggest that as-deposited films have amorphous type bandgaps which decreases with increasing temperature and film thickness. High quality, amorphous SnO_2 films with to a degree tunable optical properties are thus obtained by ALD at temperatures as low as 30 ºC using a commercially available tin precursor and water.

5. 1. Introduction

Tin oxide, SnO_x, $1 \leq x \leq 2$, is a wide bandgap semiconductor material with excellent optical, electrical and chemical properties[249-254]. As a consequence, SnO_x is used in a variety of applications including gas sensing[255-258], surface coatings for functional glasses[259-261], field effect transistors[262, 263], catalysis[264-266] and as transparent conducting oxides (TCOs) in photovoltaics and displays[81, 267-270]. As part of the solid solution of indium tin oxide, it produces one of the most commercially important TCOs [271]. In parallel with its large number of applications, many deposition techniques exist for thin films of SnO_x including chemical vapor deposition (CVD)[272-276], spray-pyrolysis[277, 278], sputtering [279] and atomic layer deposition (ALD)[53-55, 58, 59, 74-76, 280-284]. ALD is the focus of this study because it has the potential to enhance the ways SnO_x may be integrated with other materials and to broaden its applications.

For the purpose of growing uniform and conformal thin films, ALD is an increasingly popular method [5-9]. This vacuum deposition technique is based on alternating gas-surface reactions separated by inert purges allowing for self-limited growth, ideally yielding uniform and conformal films independent of substrate geometry. ALD has been used to deposit a wide range of materials, including metals [10-16], metal oxides [17-21] and metal sulfides [22-25]. It has also allowed for the area-selective growth of a variety of materials [5-9, 37-45]. Moreover, conformal coverage of three-dimensional substrates is a characteristic feature resulting from the self-limited growth mechanism of ALD [46-52].

Starting in the 1990s, ALD was explored as a way to deposit SnO_x films [53, 74, 75]. As with many other ALD systems, the choice of precursors for depositing SnO_x were derived from related CVD processes [53, 75]. Depending on growth temperature, some of these films had the advantage of being crystalline as deposited, but yielded corrosive and equipment-damaging byproducts due to the use of halogenated precursors [53-55]. Elam et al. were the first to publish on the development of a SnO_2 ALD process that used non-halogenated precursors [76] with further developments by Heo et al.[58, 59]. The work by Elam et al. elucidated the ALD process using tetrakis(dimethylamino)tin (TDMASn) and H_2O_2 and determined an average growth rate of 1.2 Å/cycle, a temperature window of 50-200 ºC and an average 94 % transmission of visible light for a film thickness of 140 nm. Growth rates of SnO_2 using TDMASn and other oxidant counter-reactants of ozone and water were also reported, although these particular ALD processes and the resultant films were not described in detail.

In this work, we build upon these previous results and further elucidate the ALD of SnO_x films using the same non-halogenated precursor, TDMASn, with water as the counter-reactant. We demonstrate the ability to deposit SnO_x at temperatures as low as 30 ºC, at growth rates equaling or exceeding that of ALD with H_2O_2 as the counter-reactant. Compared to harsher counter-reactants such as H_2O_2 and O_3, water can make SnO_x ALD more compatible with sensitive applications in, for instance, biological and polymeric systems. The use of water may further reduce operating costs and ease integration into existing processes. Moreover, water is the counter-reactant of the well-studied ZnO ALD system based on diethyl zinc [285, 286]. SnO_x ALD with water is

therefore of potential interest for the development of a thermal zinc tin oxide (ZTO) ALD process, and as such provides an opportunity for ALD of ZTO with regard to its role as a transparent conducting oxide [82].

5.2. Experimental Details

The ALD experiments were carried out in a custom-built, viscous-flow, hot-wall reactor shown schematically in Figure 5.1 and previously described in Chapter 2. The substrate was loaded into a tube style body (with 35 mm diameter and ~300 mm length) on a stage with temperature monitoring through an incorporated thermocouple placed close to the substrate position. Nitrogen carrier gas (99.999%, Air Products) at 10 sccm was flowed through the tube, enabling efficient transport of the precursors introduced at its upstream end. The reactor was evacuated by a rotary vane pump (Alcatel) resulting in a typical pressure of 100 mTorr during ALD. Precursor pressure pulse amplitudes were in the range of 1 to 50 mTorr. Numerical calculations using the finite element method based on software from COMSOL Multiphysics were used to ensure adequate reactor design through modeling of carrier gas flow and diffusion as described elsewhere [287]. A quadrupole mass spectrometer (SRS RGA200) was used to sample the gas composition through a needle valve downstream of the ALD substrate.

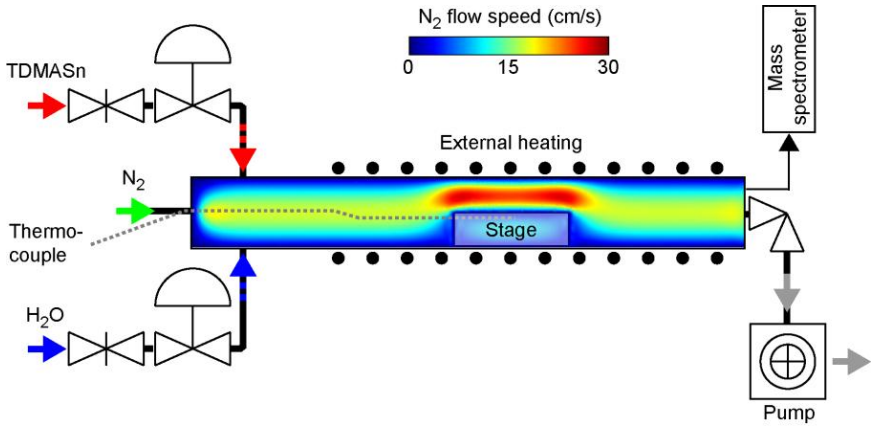


Figure 5.1. Schematic of the custom-built, hot-wall ALD reactor. The main part is a cylindrical tube, heated externally. The tube is fitted with inlets for N_2 carrier gas and precursors close to its upstream end. A sample stage with in-situ temperature monitoring is positioned near the center of the tube. A separately pumped mass spectrometer is used to analyze gas sampled downstream the stage by means of a needle valve. The calculated carrier gas flow and diffusion through the tube indicate even distribution of the gas. The flow profile in the mid section of the tube is shown.

Tetrakis(dimethylamino)tin (TDMASn, Strem, >99% purity) was used as a precursor with deionized water as the counterreactant. The TDMASn precursor vial was heated to 45 ºC and the line used to transport it into the reactor was heated to similar or higher temperature to ensure consistent vapor injections for deposition. Due to dilution in the carrier gas and effective pumping of the reactor, precursor condensation on the substrate was avoided even when the substrate temperature was slightly below the precursor vial temperature.

Substrates for SnO_x ALD included n-type Si(100) with phosphorous dopant and a resistivity of 1.0-5.0 Ω-cm (WRS Materials) and microscope slide glass (Thermo Scientific, Gold Seal, CAT. NO. 2050). All substrates were pre-cleaned using a Piranha etch (70% H_2SO_4, 30% H_2O_2) to remove organics and generate a chemical oxide. SnO_x thin films were deposited directly onto this chemical oxide. After loading into the reactor, samples were allowed to outgas for at least 20 min before the reactor was

heated to achieve the desired substrate temperature. After injection of a given precursor for a certain pulse time, the excess precursor was purged with nitrogen before the counter-reactant was introduced. The ALD sequence is compactly expressed as t_1:t_2:t_3:t_4, where t_1 and t_3 correspond to the pulse lengths of TDMASn and water, respectively, and t_2 and t_4 to N_2 purge times following these doses. A typical timing sequence was 1:30:2:30 s.

The deposited SnO_x films were analyzed *ex-situ* by a variety of methods. A PHI VersaProbe 5000 Scanning X-ray Photoelectron Spectrometer with Al Kα radiation was used to determine elemental compositions, using the C1s peak at 285.0 eV as a reference. After initial survey scans, adventitious carbon was removed by Ar^+ sputtering for 12 s (1 keV, 0.5 μA, 1 mm x 1 mm at 45 º incidence from the sample). As-deposited films were annealed under flow of N_2 (1 cm^3/s) in a Mellen Series SC13R-1300 ºC, single zone, split hinged, round tubular furnace with an Omega 7832 process controller at 500 ºC and 600 ºC. X-ray diffraction (XRD) measurements were taken as a function of anneal temperature using the PANalytical X'Pert PRO system in parallel beam mode with Cu Kα radiation at 45 kV and 40 mA. Film thickness and optical constants of SnO_x deposited on Si(100) were determined using a J.A. Woollam M2000 Variable Angle Spectroscopic Ellipsometer (VASE). Plan view and cross-sectional images of SnO_x film morphology were examined using a FEI Magellan 400 XHR Scanning Electron Microscope with FEG source (5 kV and 25 pA). Optical extinction spectra of films deposited on microscope slide glass were recorded using a Varian Cary 6000i UV-Vis-NIR spectrometer. Topographical information for the films

was determined by atomic force microscopy using a Park System Atomic Force Microscope in tapping mode.

5.3. Results and Discussion

5.3.1. SnO_x ALD Growth Characterization

Considering the surface reactions involved in the process is important for understanding the film growth by ALD. Elam et al. proposed a possible mechanism for the SnO_2 ALD using TDMASn and H_2O_2 based on in-situ quartz crystal microbalance (QCM) analysis[76]. The corresponding reaction mechanism with water as the counter-reactant is

$$(OH)^*_x + Sn(DMA)_4 \rightarrow (O)_xSn(DMA)_{4-x}^* + x\ HDMA \quad (5.1)$$

$$(O)_xSn(DMA)_{4-x}^* + 2H_2O \rightarrow (OH)^*_x + SnO_2 + (4-x)\ HDMA \quad (5.2)$$

where DMA represents the dimethylamino ligand, HDMA is dimethylamine (released to gas phase), the * refers to surface-bound species and x the number of DMA ligands released during the TDMASn pulse. Measurements by Elam et al. indicated that $x \approx 2.5$ with H_2O as the counter- reactant, compared to a higher value of $x \approx 3$ when using H_2O_2. They suggest that this reaction stoichiometry is consistent with the lower growth rate observed with H_2O at higher temperatures and largely reflects a lower degree of surface hydroxylation. The first reaction (1) shows the importance of the surface hydroxylation state for the initial adsorption of the precursor.

To determine the conditions for saturated ALD of SnO_x in these studies, the growth rate as a function of TDMASn precursor pulse time (t_1) was investigated. Thin films of SnO_x were deposited on Si(100) at 150 ºC for 200 cycles with a timing sequence of t_1:30:2:30 s. The purge times of 30 s were conservatively selected to be

long enough to purge away excess reactant, as judged by the downstream gas composition monitored by mass spectroscopy and purge studies (Figure 5.5). In this way, contributions from chemical vapor deposition (CVD) were minimized. Average film thicknesses determined by VASE were used to calculate the SnO_x growth rate. Figure 5.2a represents the saturation curve for TDMASn and shows that, within the uncertainty of the experiment, saturated behavior is reached already for the shortest pulse time of 0.5 s at 150 ºC. The TDMASn pulse time was fixed to 1 s to ensure saturation in subsequent experiments. The SnO_x growth as a function of water pulse length (t_3) was also investigated following a similar procedure as before but using a pulse-purge sequence of 1:30: t_3:30 s. Figure 5.2b shows that a relatively steady growth rate is established after 0.5 s H_2O pulse times. The first data point, although small, is non-zero. The amino-tin bond is known to be highly reactive with oxidant sources [288]. Given its high reactivity, this growth in the absence of the water pulse may have resulted from reactions with residual surface hydroxyl groups or water on the substrate, or from trace amounts of water in the reactor chamber. These precursor saturation studies suggest that saturated growth is accomplished for a broad range of pulse lengths. Growth rates with good reproducibility for a timing sequence of 1:30:2:30 s at 150 ºC were obtained.

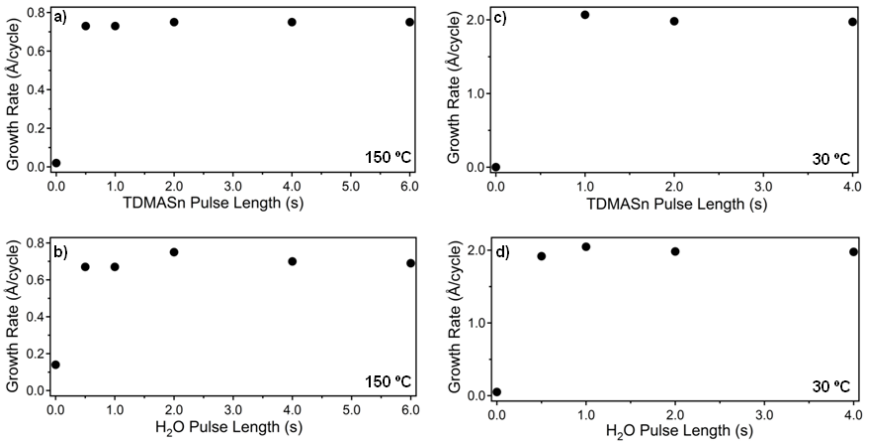


Figure 5.2. SnO_x growth rate determined by VASE, as a function of (a) and (c) TDMASn pulse length *x* for timing sequences of *x*:30:2:30 s and (b) and (d) H_2O pulse length *y* for timing sequences of 1:30:*y*:30 s. The substrate was Si(100) at 150 ºC for (a) and (b) and at 30 ºC for (c) and (d).

The precise conditions for establishing ALD saturation in terms of precursor exposure time depend on the particular reactor design in addition to the choice of precursor and counter- reactant. The work of Elam et al. using the tin precursor, TDMASn and H_2O_2 to deposit SnO_x by ALD showed a gradual approach toward saturated growth. To explain this gradual ascent toward saturation, it was proposed that DMA binds strongly to the hydroxylated substrate resulting in slow desorption, thereby limiting the adsorption of further TDMASn for pulse times below 2 s. However, this effect was not observed in our studies in which water was used as the counter- reactant; for the pulse time intervals explored, there is little difference between growth rates at shorter (0.5 s) and longer pulse times (>1.0 s) suggesting that surface saturation occurred quickly.

Figure 5.3 presents the SnO_x film thickness as a function of number of ALD cycles over the range of 20 to 700 cycles. The data were collected using VASE for deposition on a Si(100) substrate at 150 ºC with a timing sequence of 1:30:2:30 s. The linear

dependence of film thickness on cycle number indicates sustained layer-by-layer growth characteristic of ALD. The average growth rate is 0.70 Å /cycle, in close agreement with the previously reported value at this temperature by Elam et al. [76].

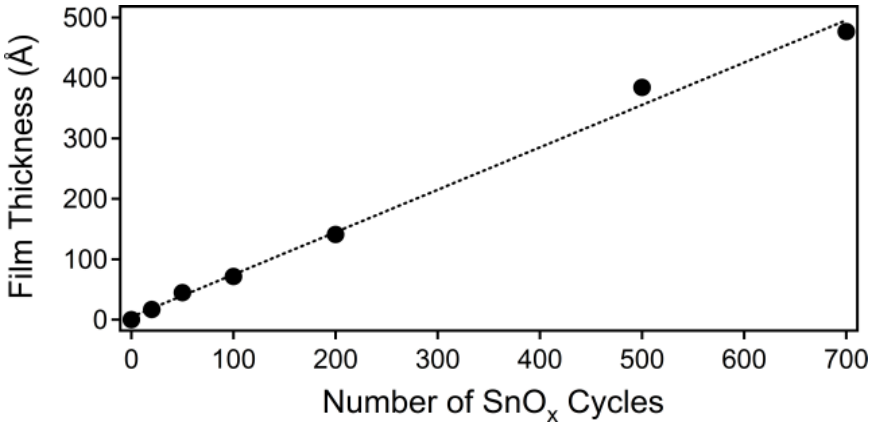


Figure 5.3. SnO_x film thickness as a function of number of ALD cycles yielding a growth rate of 0.70 Å/cycle. Thicknesses were obtained using VASE for films deposited on Si(100) at 150 ºC with a time sequence of 1:30:2:30.

Figure 5.4 shows the growth rate of SnO_x as a function of deposition temperature ranging from 30 to 200 ºC. The growth rate displays a clearly decreasing trend with increasing deposition temperature over the entire interval, with a slight plateau in the range from 150 to 175 ºC. The growth rate at 30 ºC of ~2.1 Å/cycle is about 4 times higher than that at 200 ºC where it is ~0.5 Å/cycle. This sensitivity to deposition temperature is much higher than that reported for the TDMASn and H_2O_2 ALD system[76]. In that system, the growth rate varied less dramatically from 50 ºC to 200 ºC, (from ~1.6 Å /cycle to ~1.3 Å /cycle, respectively). Also, a region of near constant growth rate was shown between 100 ºC and 200 ºC. On the other hand, it is interesting to note that the use of water as a counter-reactant results in a higher growth rate at low temperatures than that previously observed with H_2O_2. Comparing with the data

presented by Elam et al., the crossover is around 80 ºC. So even though the use of water as a TDMASn counter-reactant is expected to result in lower concentration of reactive surface hydroxyl groups at the higher temperatures investigated, the overall SnO_x growth rate is higher at the lower temperatures.

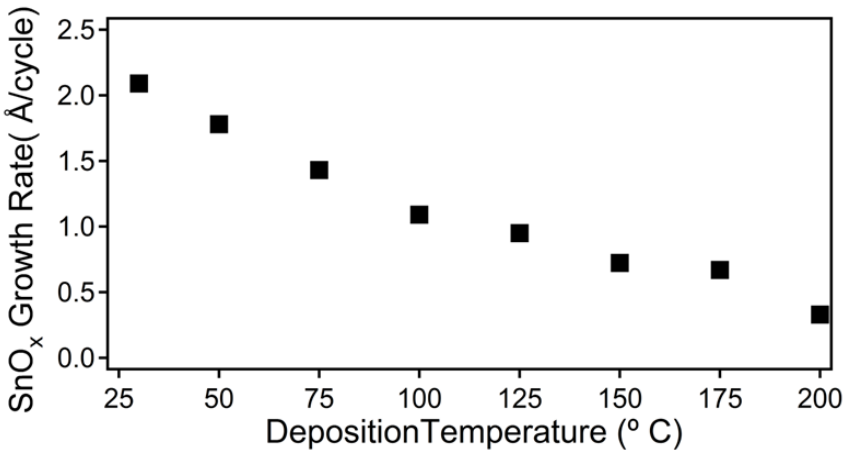


Figure 5.4. SnO_x ALD growth rate as a function of temperature determined using VASE for films deposited on Si(100) for 200 cycles with timing sequence 1:30:2:30 s

It is speculated that larger amounts of more loosely bonded molecular water or water-derived species are available in this temperature range and capable of contributing to the growth observed. However, measurement of the growth rates at 30 ºC presented in Figure 5.2c and 2d show that the reactions still saturate with the water precursor pulse length. Furthermore, at this low temperature, growth rate purge time dependence following the 1s TDMASn pulse (Figure 5.5a) and 2 s water pulse (Figure 5.5b), show saturated growth characteristic of ALD. Taken together, these data imply that the water and water-derived species present at the surface contribute to the growth of the SnO_x film at this low temperature. Though in-situ or fundamental studies may be needed to elucidate the detailed nature of the water derived species responsible for the

high growth rate in this regime, it is a significant finding that growth saturation behavior, characteristic of ALD, can be achieved at 30 ºC.

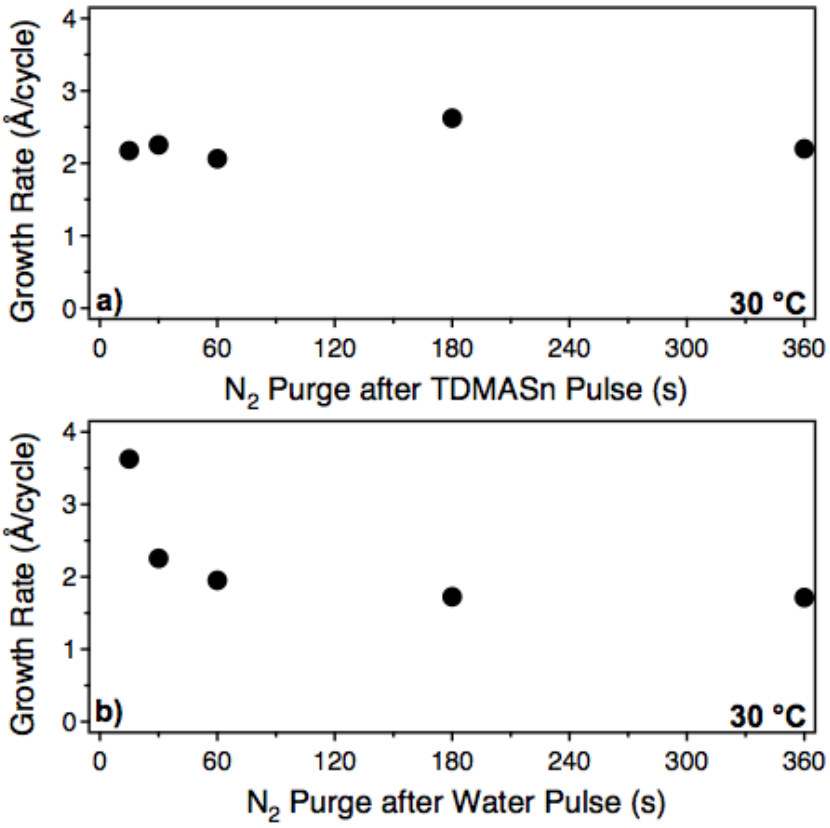


Figure 5.5. SnO_x growth rate at 30 ºC determined by VASE as a function of nitrogen purge time following (a) TDMASn pulse length and (b) H_2O pulse length for timing sequences of $1:t_2:2:t_4$ s. time dependence . The substrate was Si(100). substrate was Si(100).

5.3.2. SnO_x Film Characterization and Properties

5.3.2.1. Elemental and Structural Analysis

X-ray photoelectron spectroscopy (XPS) was performed to determine the film composition. Figure 5.6 shows an XPS survey scan of a 46 nm SnO_x film deposited at 150 ºC on Si(100) after removal of adventitious surface carbon by Ar^+ sputtering. The

data show the presence of both Sn and O, confirming the deposition of an oxide of tin; no carbon or nitrogen contamination is observed.

Providing a quantitative stoichiometry of the SnO_x film from XPS data is difficult. The atomic ratio of Sn:O before sputtering was close to 1:2 which would suggest a stoichiometry of SnO_2. After sputtering the ratio of Sn:O was closer to 1:1 suggesting a stoichiometry of SnO. However, the possibility of preferential sputtering of one element over another leads to uncertainty in the compound stoichiometry. Using the core level shifts to determine the oxidation state of as-deposited SnO_x using XPS is also challenging due to the closeness in values of the $Sn3d_{5/2}$ binding energies for SnO (486.8 eV) and SnO_2 (487.2 eV).

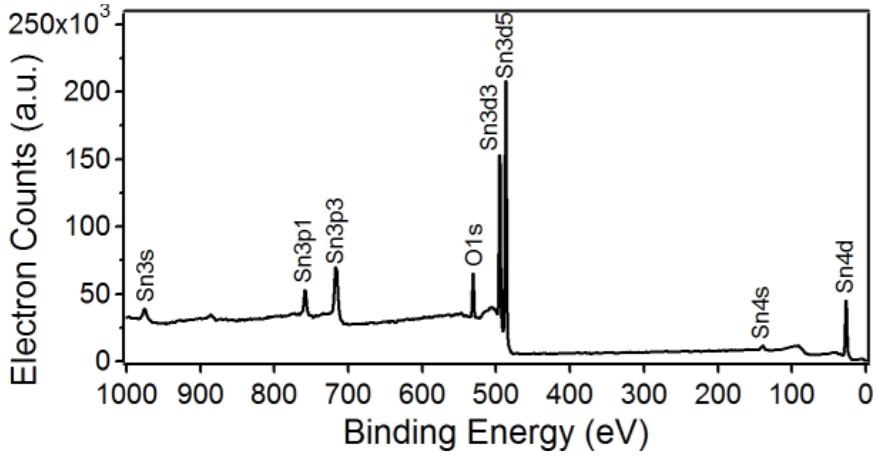


Figure 5.6. X-ray photoelectron spectroscopy survey scan of 46 nm SnO_x film deposited on Si(100) at 150 ºC after Ar^+ sputtering**.**

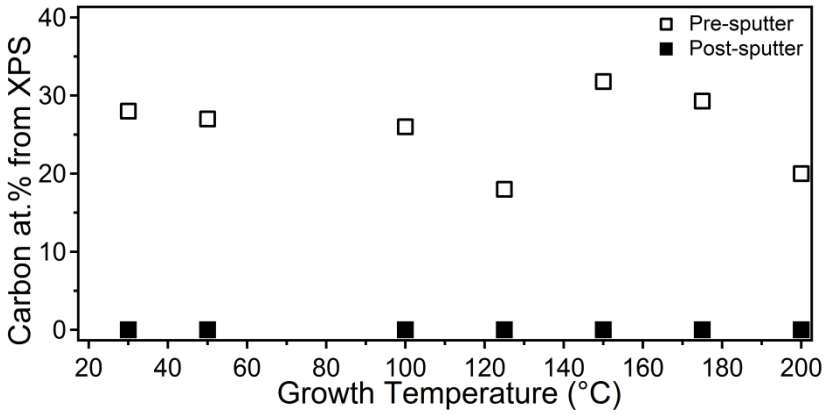


Figure 5.7. Atomic concentration of carbon as a function of deposition temperature of SnO_x deposited on Si(100) at 150 ºC before and after Ar^+ sputtering

XPS spectra were also obtained for SnO_x films as a function of ALD temperature. The data show that nearly carbon-free films can be deposited at all growth temperatures studied. Carbon levels determined by XPS as a function of deposition temperature are shown in Figure 5.7, both before and after Ar^+ sputtering to remove adventitious carbon. Although carbon is observed in all films before sputtering, the films were solely comprised of Sn and O independent of deposition temperature. Importantly, these data indicate that SnO_x ALD films can be deposited without significant carbon contamination even near room temperature. In contrast, nitrogen and carbon contamination was observed by Elam et al. when using H_2O_2 rather than H_2O at temperatures below ~100 ºC.

The SnO_x films were examined by XRD both as deposited and after annealing in nitrogen. Figure 5.8 shows the XRD patterns as deposited and after nitrogen annealing to 600 ºC; reference diffraction patterns of SnO and SnO_2 are included for comparison. For the as-deposited film at 150 ºC, the film appears to be amorphous. Patterns appear but exhibit broad peaks upon annealing at 600 ºC.

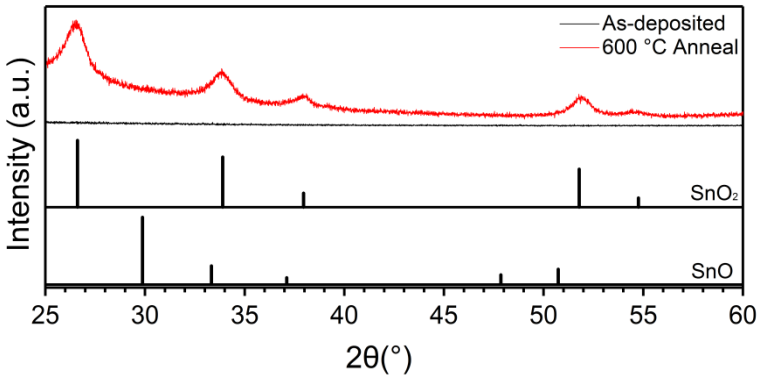


Figure 5.8. XRD patterns for a 130 nm film of SnO_x deposited on Si(100) at 150 ºC as function of annealing temperature under flow of N_2, as-deposited (black) and 600 ºC anneal (red).

The diffraction patterns after annealing are characteristic of the SnO_2 phase, including reflection of the (110), (101), (200) and (211) planes at 26.6º, 33.9º, 37.9º and at 51.8º. The diffraction peaks in Figure 5.8 are indexed on the basis of the rutile SnO_2 unit cell. Patterns indicative of SnO for reflection of the (101) and (110) planes at 29.9º and 33.3º were not evident. The large width and low intensities of the peaks may be the result of small crystallites from incomplete crystallization as well as the relatively small thickness of the films (130 nm). The data strongly suggest that these films consist of rutile SnO_2.

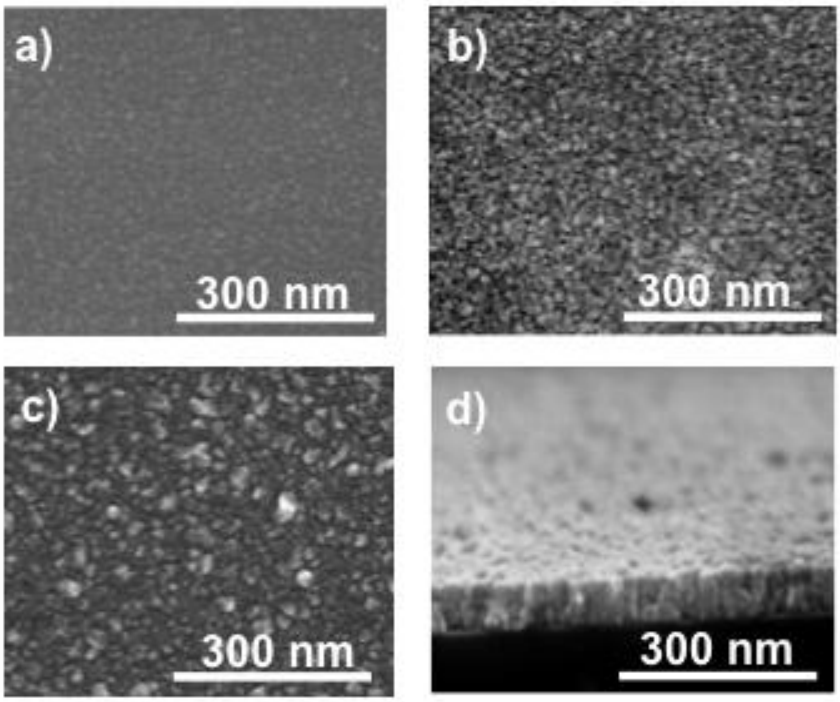


Figure 5.9. SEM images of a 46 nm SnO_x film deposited on Si(100) at 150 ºC (a) as-deposited; (b) post-500 ºC anneal; (c) post-600 ºC anneal; (d) cross-section of post-600 ºC anneal.

The film morphology as a function of annealing temperature in N_2 is shown in Figure 5.9 for a 46 nm thick SnO_x sample deposited at 150 ºC on Si(100). Figure 5.9a indicates that the as-deposited film morphology is somewhat rough but with little variation in features. From AFM (data not shown), the root mean squared (rms) roughness of the as-deposited film was 3.3 nm. Figure 5.9(b-c) show plan view SEM images of films annealed at 500 ºC and 600 ºC, respectively. Upon annealing, the film roughness and the crystallite size increase. The appearance of a more polycrystalline film is consistent with the diffraction pattern from XRD. The cross-sectional image in Figure 5.9d of the film annealed at 600 ºC provides more support for polycrystallinity. The rms roughness of this film was 4.5 nm as determined by AFM, which is larger than for the as-deposited case and consistent with the growth of larger crystallites.

5.3.2.2. Optical Analysis

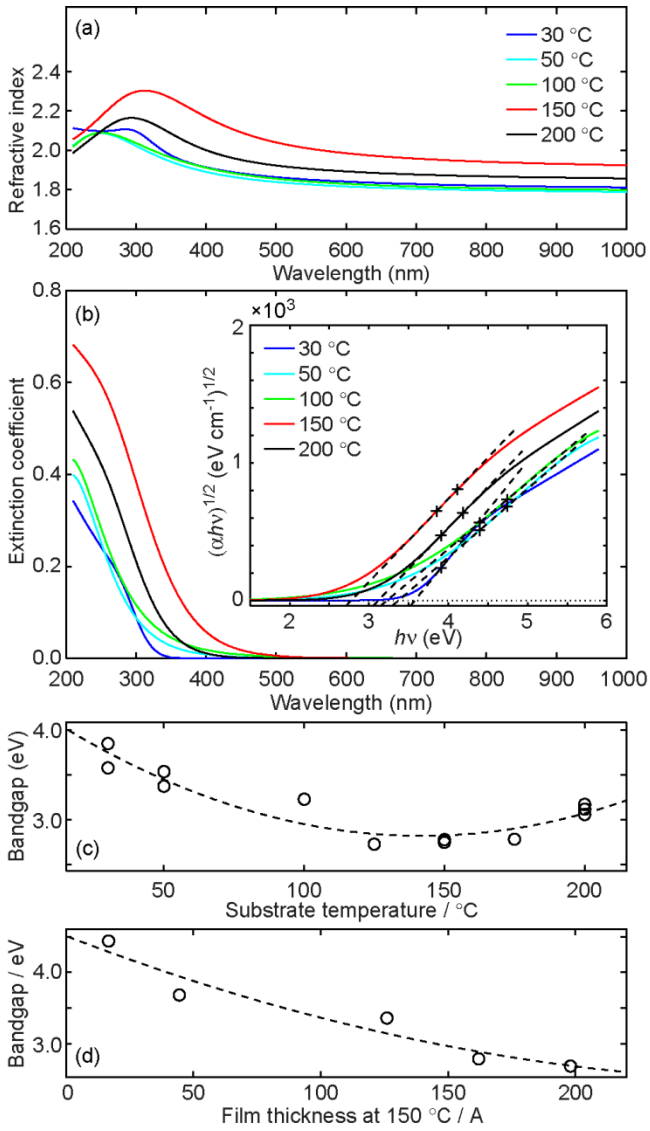


Figure 5.10. SnO_x film refractive index and (b) extinction coefficient extracted from spectroscopic ellipsometry, as a function of the substrate temperature for films deposited using 200 ALD cycles. The inset in (b) illustrates plots of $(\alpha h\nu)^{1/2}$ with linear fits (dashed lines) to the approximately linear portion of the curve. Bandgaps are estimated from the intersection of the linear fits with $(\alpha h\nu)^{1/2} = 0$. (c) Estimated bandgaps as a function of temperature, after 200 cycles of ALD. (d) Bandgaps as a function of film thickness for varying number of ALD cycles and a substrate temperature fixed to 150 °C. The dashed lines in (c-d) represents quadratic fits to the data.

Variable angle spectroscopic ellipsometry was used to analyze the optical properties of SnO_x films deposited on Si(100) using 200 cycles of ALD and varying substrate temperatures (30-200 ºC). The resulting refractive index *n* and extinction coefficient *k* are displayed in Figure 5.10a and b, respectively. They both vary with temperature, and display maximum values for films deposited around 150 ºC. In order to analyze the corresponding bandgaps of these films, the absorption coefficients are obtained from the extinction coefficients through $\alpha = 4\pi k/\lambda$, where λ is the wavelength of light. For amorphous and indirect bandgap semiconductors, a linear portion in the energy dependence of the function $(\alpha h\nu)^{1/2}$ is typically found near the bandgap. By extrapolating this linear portion to zero absorption in a Tauc-plot, the bandgap is obtained as the energy value at the intersection (see inset of Figure 5.10b). Figure 5.10c shows the bandgaps obtained in this way as a function of substrate temperature. For reference, though dependent on deposition method, SnO_2 bandgaps typically fall within the range of 3.6 to 4.0 eV[253, 289, 290].

Again, a significant temperature dependence is observed, with a minimum in the bandgap around 150 ºC. Because the number of ALD cycles were fixed in this experiment, the varying growth rates (Figure 5.4) means that the film thickness were higher for the lower temperatures. To investigate if the bandgap energy and other properties depend on the film thickness, additional experiments at fixed temperature (150 ºC), and varying number of ALD cycles were performed. The results, shown in Figure 5.10d, indicate a monotonic decrease of bandgap with thickness, from 4.4 eV for the thinnest (approximately 2 nm) film down to 2.7 eV for the thickest (20 nm) film.

Work is in progress to further analyze this sensitive dependence of the optical properties on film thickness and substrate temperature in the SnO_x ALD system..

5.4. Conclusions

By exploring in detail the usage of water as a counter-reactant, this work expands on the application of tetrakis(dimethylamino)tin (TDMASn) for the deposition of high quality tin oxide films in a low temperature range of 30-200 ºC. Spectroscopic analyses show no appreciable change in elemental composition as a function of deposition temperature. Morphological and topographical analyses show that as-deposited SnO_x film is relatively smooth, with little crystalline features. XRD measurements before and after annealing in inert atmosphere confirms that the deposited films consist of amorphous SnO_2 which transform to rutile SnO_2 after annealing. The optical properties of the films display an interesting dependence on both deposition temperature and film thickness. Thin films grown at low temperature (30 ºC) display relatively high bandgaps in excess of 4.0 eV, while thicker films grown at 150 ºC have bandgaps below 3 eV. Thus, high-quality SnO_x films which may to some extent be tailored can be grown using this ALD process. This scheme for SnO_x ALD can allow for electrically and optically useful films, such as for transparent conductors and solar cell buffer layers, to be produced from earth abundant and inexpensive raw materials. The ability to grow this important metal oxide at near room temperature may further be favorable for biological applications and in industrial processes where reduced thermal demands are desired

Chapter 6. Thin Film Characterization of Zinc Tin Oxide Deposited by Thermal Atomic Layer Deposition

Zinc tin oxide (ZTO) thin films are of interest for many applications, including transparent conducting oxides (TCO) and buffer layers in thin film solar cells. In this work, the ability of atomic layer deposition (ALD) to control both thickness and composition of the ternary material is explored and the resulting film properties are characterized. ZTO was deposited at 150 ºC by alternating growth of tin oxide (SnO_x) and zinc oxide (ZnO) using tetrakis(dimethylamino) tin (TDMASn) and diethyl zinc (DEZn) as metal precursors and water as the oxygen source. The growth behavior of ZTO was systematically examined as a function of the relative fraction of SnO_x to ZnO and their bilayer period. Variable angle spectroscopic ellipsometry (VASE) was used to show that the growth rate was strongly reduced as the bilayer period decreased. Inductively-coupled plasma optical emission spectroscopy (ICP-OES) showed that the composition and other properties of ZTO films were not simply proportional to the growth rates and ALD cycle fractions of the individual metal oxides. For instance, at 150° C the average growth rate decreased from ~ 1.93 Å/cycle for ZnO to less than half (~ 0.80 Å/cycle) for films with ~50% composition of Sn and Zn. Structurally, the deposited films were shown by X-ray diffraction (XRD) to be amorphous for tin content exceeding 10%, for which only smooth features were observed by scanning electron microscopy (SEM). Optically, VASE revealed a minimum refractive index in the visible range for intermediate compositions and a maximum for the pure SnO_x phase. Conversely, the ZTO bandgap was maximized for intermediate compositions near ~50%, and converged to the direct ZnO bandgap of 3.3 eV for compositions with

decreasing amounts of SnO_x . The SnO_x bandgap type could not be unambiguously determined, but linear extrapolations gave a range of 2.9 to 4.0 eV depending on the bandgap type (indirect or direct). This is in line with previous reports for SnO_2.

6.1. Introduction

Transparent conducting oxides (TCOs) are wide bandgap (≥ 3 eV), transmissive to visible light (≥ 80%) and highly conductive (≥10^3 S-cm^{-1}) metal oxides with many applications in consumer electronics and in photovoltaics [80, 82, 132, 133]. The oxides of indium, tin and zinc, which comprise the ZITO family, are the most commercially-important TCOs [82, 134]. These binary TCOs are typically doped with an impurity to improve stability at high temperatures [135]. Within the ZITO family, indium tin oxide (ITO) remains the industry-standard for high-end TCOs because of its high conductivity (≥10^4 S-cm^{-1}) [136-138]. However, the scarcity of indium coupled with the increasing demand in consumer electronic and photovoltaic markets has led to rising costs [81], which motivates the need to find alternative TCO materials.

Impurity-doped or alloyed zinc oxides are interesting candidates for this purpose, where intermixes with aluminum (AZO) or gallium (GZO) are well known examples [80, 291-293]. While AZO and GZO exhibit attractive properties as inexpensive indium-free alternatives, other options such as zinc tin oxide (ZTO) are also being studied as an inexpensive indium-free TCO [80, 81, 294-302]. Notably, the National Renewable Energy Laboratory used ZTO as a TCO in its then champion CdTe 16.5 % efficient solar cell [303]. In addition to its use as a TCO and buffer layer in high efficiency solar cells [91, 303, 304], ZTO has been used in thin-film transistors [83-85, 304] and may also serve as potential varistors [305, 306]. Despite its promise, a

comprehensive review of the literature suggests little agreement among various structural, optical and electrical properties of ZTO, motivating a more detailed characterization of this material.

In general, there is agreement that ZTO forms two crystal structures. The metastable $ZnSnO_3$ phase, known as zinc metastannate, that has two polymorphs – a face-centered perovskite [77] and an ilmenite [78] structure. The other structure, Zn_2SnO_4, is known as zinc orthostannate and has a cubic spinel structure which is stable under ambient conditions [79]. However, the correlation between composition and crystallinity is not well-understood. The most extensively used deposition techniques for ZTO have been by sputtering [135, 294, 295, 298, 299, 307, 308]. During crystallization, ZTO transforms to $ZnSnO_3$ from 300-500 ºC and to Zn_2SnO_4 for temperatures exceeding 600 ºC [79]. At these high temperatures, however, obtaining pure Zn_2SnO_4 is difficult, as mixed phases including both forms of ZTO and SnO_2 are formed [79]. Other techniques for ZTO deposition have included sol-gel spin coating [83-85], chemical vapor deposition [86] and only very recently ALD [87-91].

A lack of agreement on the ZTO crystal structure as a function of composition may explain the variation in reports on its optical properties. One study (using pulsed laser deposition) has reported bandgaps for amorphous ZTO, of 2.80 eV for $ZnSnO_3$ and 2.86 eV for Zn_2SnO_4 [309]. Young et al. found crystalline Zn_2SnO_4 to have a fundamental bandgap of 3.35 eV that could be widened to 3.89 eV by a Burstein-Moss shift due to high carrier concentration [310]. For ZTO synthesized by hydrothermal methods, the optical bandgap for crystalline Zn_2SnO_4 has been reported with great variation in the range of 3.3 to 3.9 eV [311, 312]. The bandgap for crystalline $ZnSnO_3$

has not been rigorously characterized experimentally, but one report presents a value of ~3.9 eV [313].

Most previous studies using ZTO focused on device performance instead of film characterization, resulting in few comprehensive reports of material and electrical properties as a function of composition. Because ALD allows one to carefully dope or alloy material with control over growth on the order of ~1 Å per cycle with uniform and conformal growth [5-7, 9], it provides an opportunity to systematically analyze ZTO properties as a function of composition. So far, ALD has been used to deposit ternary metal oxides including AZO [140-144], GZO [145, 146], ITO [56], $(Zn,Mg)O_x$ [147] and $(Sn,Al)O_x$ [149].

The most extensive analyses for thermal ALD of ZTO thin films have been for use as a CIGS buffer layer [88-91]. These reports however, do not systematically address the ALD experimental design in terms of how finely the different binary metal oxide are intermixed, as determined by the number of heterointerfaces formed in the ALD process and how this factor affects growth rates and material properties.

In this chapter, a reproducible thermal ZTO ALD process is demonstrated. The composition, optical and structural properties of the resulting thin films are characterized by variable angle spectroscopic ellipsometry (VASE), x-ray photoelectron spectroscopy (XPS), inductively-coupled plasma optical emission spectroscopy (ICP-OES), scanning electron microscopy (SEM), x-ray diffraction (XRD) and ultraviolet-visible spectroscopy. A formalism for ALD super cycles is defined from which the important characteristics of cycle ratios (composition) and film lamination described in

terms of bilayer period follows. The effects of the composition and bilayer period on growth rate, composition, structural and optical properties are reported.

6.2. Experimental Methods

The ALD experiments were carried out in a custom-built, viscous-flow, hot-wall reactor previously described [314]. Diethyl zinc (DEZn; Sigma-Aldrich) and tetrakis(dimethylamino)tin (TDMASn; Strem, >99% purity) were used as precursors with deionized water as the counter-reactant. Precursors were dosed from 10 cm^3 stainless steel sample vials using computer controlled air-actuated valves. The water and DEZn sample vials were kept at room temperature, while the TDMASn vial was heated to 45 ºC during depositions. A positive temperature gradient was maintained towards the reaction zone to prevent precursor condensation.

Substrates for ZnO, SnO_x and ZTO ALD were n-type Si(100) with phosphorous dopant and a resistivity of 1.0-5.0 Ω-cm (WRS Materials) and fused silica quartz (ChemGlass). Substrates were pre-cleaned using a UV-ozone (PSD Benchtop UV-Ozone Cleaner) to remove organic contamination, after which the thin films were deposited onto the native Si oxide. During the ALD process, excess amounts of precursors were purged with nitrogen for half-reaction separation and reaction completion. For ZnO ALD, the pulse time sequences are expressed as z_1:z_2:z_3:z_4, where z_1 and z_3 correspond to the pulse lengths of DEZn and water, respectively, and z_2 and z_4 correspond to N_2 purge times following these doses. A typical ZnO ALD pulse time sequence was 1:15:1:30 s. The purge times of z_2 = 15 s and z_4 = 30 s were chosen based on the return of the precursor concentrations to their baseline values as monitored by in-situ mass spectrometry, as well as previously found saturation in this range for the ZnO

system [141, 148]. For SnO_x ALD, the ALD sequences are similarly expressed as t_1:t_2:t_3:t_4, where t_1 and t_3 correspond to the pulse lengths of TDMASn and water, respectively, and t_2 and t_4 correspond to N_2 purge times following these doses. A typical timing sequence was 1:30:2:30 s which corresponded to saturated ALD of SnO_x as previously as previously described [314].

A variety of ex-situ analyses were performed on the as-deposited ZnO, SnO_x and ZTO films. A PHI VersaProbe 5000 Scanning X-ray Photoelectron Spectrometer with Al-Kα radiation was used to survey film elemental content. The C1s peak at 285.0 eV was used as a reference. After initial survey scans, adventitious carbon was removed by Ar^+ sputtering for 12 s (1 keV, 0.5 μA, 1 mm x 1 mm at 45 º incidence from the sample). A Thermo Scientific ICAP 6300 Duo View spectrometer was used to perform inductively-coupled plasma optical emission spectroscopy (ICP-OES) on ZTO deposited on Si(100). For these measurements, films were dissolved in aqua regia (3:1 concentrated HCl: HNO_3) and sonicated for at least 6 h before characterization. X-ray diffraction (XRD) measurements of ZTO on fused-silica quartz were performed as a function of ALD cycle fractions (and thus compositions) using the PANalytical X'Pert PRO system in parallel beam mode with Cu Kα radiation at 45 kV and 40 mA. Grazing incidence x-ray diffraction (GIXRD) was also performed on ZTO films deposited on Si(100) using 12.7 keV x-rays that were incident on the sample at 0.48 º. Diffracted x-rays were collected with an MAR34 two dimensional imagining detector calibrated using a LaB_6 reference.

Film thickness and optical properties of ZTO deposited on Si(100) were determined using a J.A. Woollam M2000 Variable Angle Spectroscopic Ellipsometer

(VASE) at 65, 70 and 75° angles of incidence and wavelengths ranging from 210 to 1688 nm. In the analysis, the optical properties of the films were represented by a sum of oscillator terms, described in more detail below. A model with a single homogeneous layer (to be referred to as a single layer model) was found accurate for finely layered ZTO, but for the most coarsely layered stacks, the root mean squared error (MSE) was lower if taking the periodic structure into account with a two layer unit cell corresponding to the super cycle of ZnO and SnO_x used in the ALD sequence. The latter will be referred to as a super cycle model.

Plan view images of ZTO film morphology on Si(100) were examined using a FEI Magellan 400 XHR Scanning Electron Microscope with FEG source (5 kV and 25 pA). Optical extinction spectra of films deposited on quartz were recorded using a Varian Cary 6000i UV-Vis-NIR spectrometer.

6.3. Results and Analysis

6.3.1. ZTO Properties as a Function of Bilayer Period

Designing a reproducible ZTO ALD process first required optimization of the binary ZnO and SnO_x ALD processes in our reactor. It is convenient that there is overlap in the ALD temperature windows for these binary metal oxide processes. It was reported previously that within the ZnO ALD temperature window, a maximum growth rate of about ~2.0 Å /cycle occurs at 150 ºC [315] which matches closely with the optimized growth rate of 1.9 Å /cycle for our reactor. The ALD of SnO_x, reported elsewhere [314], results in SnO_x growth rate of about 0.70 Å/cycle at 150 ºC. In addition to the disparity between the growth rates, another difference between SnO_x and

ZnO is the long-range order of the as-deposited materials at this temperature. For the optimized SnO_x ALD system, the as-deposited film is amorphous [314]. On the other hand, it is well-known that as-deposited ZnO grown by ALD at 150 ºC has a crystalline hexagonal wurtzite structure [316].

Given the significant difference in growth rate and phase, obtaining a preliminary understanding of how one binary oxide grows on another is necessary. Atomic layer deposition allows the sequential dosing of an arbitrary number of SnO_x and ZnO cycles in any desired ratio. It is hypothesized that the more finely spaced these dosing sequences are, the more laminated the film will be and the less the film will resemble its constituent binaries in growth rate and material properties. The super cycle is defined as the minimum sequence of SnO_x and ZnO cycles that is repeated over the course of the ZTO ALD process. A corresponding super cell results from the stack of layers produced by one super cycle. To characterize the ALD system, we define

- *t*, the total number of SnO_x ALD cycles in one ZTO ALD super cycle
- *z*, the total number of ZnO ALD cycles in one ZTO ALD super cycle

Using these parameters, illustrated in Figure 6.1, the system can be characterized by:

(1) the *bilayer period, Λ,* defined as the number of cycles in one super cycle,

$$\Lambda = (t + z) \tag{6.1}$$

(2) the relation for the total number of ZnO and SnO_x cycles in a ZTO ALD process, if a total number of *super cycles S* are performed,

$$A = S \times \Lambda \tag{6.2}$$

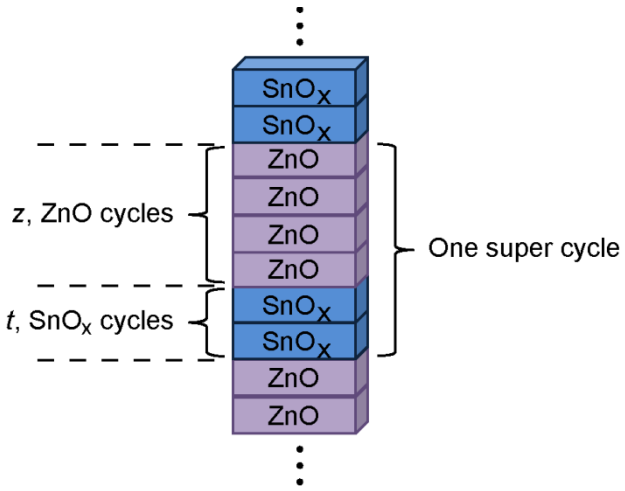


Figure 6.1. Schematic of ZTO super cycle formalism visualized as a lamellar stack of ALD cycles of constituent binary oxides. One super cycle is defined by a certain number of SnO_x cycles, *t*, and ZnO cycles, *z*.

This ZTO ALD super cycle formalism provides a systematic approach to determining the effects of the bilayer period, Λ, on the growth rate and other properties. To study the effect of lamination without changing the overall ZTO composition, we fixed the total number of ZnO and SnO_x cycles to 200 and 600, respectively. Fixing these parameters yielded a tin cycle fraction $f_{Sn} = 0.75$, which based on the binary growth rates would result in an intermediate (c_{Sn} ~43%) overall composition. In order to maintain the same number of ALD cycles, we had to vary *S*, the total number of super cycles. Table 6.1 summarizes the sample and growth properties, including the bilayer period and the measured Sn composition fraction and growth rate as a function of the super cycle settings.

Table 6.1. Summary of experiments for varying bilayer period Λ and total number of super cycles, S and the growth rate, determined by VASE. Constants were Sn/(Sn+Zn) cycle fraction, f_{Sn} = 0.75, and A = 800 total number of ZTO ALD cycles comprised of 200 ZnO ALD cycles and 600 SnO_x total ALD cycles. Tin composition fractions, c_{Sn}, were determined by ICP-OES. Films were deposited at 150 ºC on Si(100) and on fused silica quartz.

Number of Super Cycles, *S*	***t***	***z***	**Bilayer Period Λ**	**Sn Composition Fraction, c_{Sn}**	**Growth Rate (Å/cycle)**
200	3	1	4	0.35	0.52
100	6	2	8	0.46	0.55
20	30	10	40	0.36	0.79
5	120	40	160	0.37	0.94
2	300	100	400	0.38	0.97
1	600	200	800	0.42	1.06

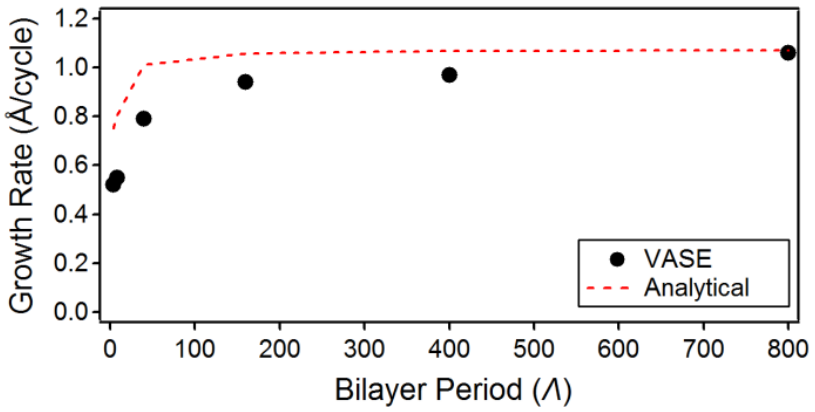


Figure 6.2. Growth rate versus bilayer period based, Λ, on experimentally-determined values from VASE and an analytical method (Equation 5.5).

The data in Table 6.1 and Figure 6.2 show that the growth rate of the intermixed system decreases decreasing bilayer period, Λ.. When a weighted average of the binary growth rates is calculated for f_{Sn} = 0.75, a value of 0.99 Å /cycle results, which closely matches the growth rates of the films with the highest values of Λ. In contrast, for the films with low values of Λ, the growth behavior deviates significantly from predicted

binary growth rates. This reduced growth rate suggests that at least one of the materials does not grow as well on its counterpart as on itself. An analytical model, described in a later section, has been used to predict the growth rate dependence on bilayer period, Λ.

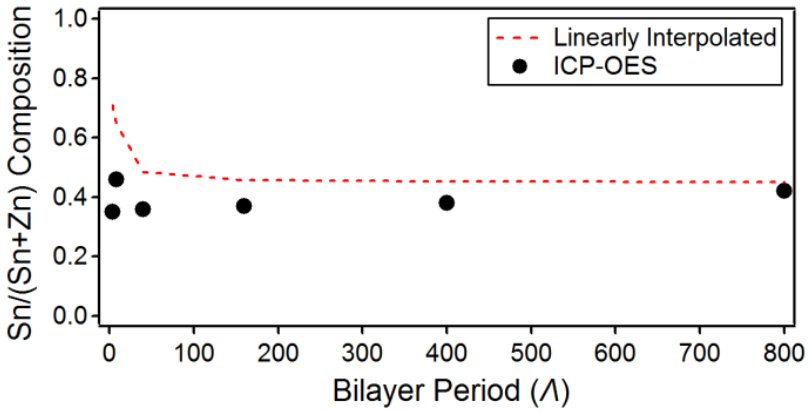


Figure 6.3. Tin composition fraction versus bilayer period based, Λ, on experimentally-determined values from ICP-OES (black circles)and an analytical model (red dashed line, Equation 5.5).

In general, as shown in Figure 6.3, the overall tin content is also observed to vary only slightly from the average value (c_{Sn} = 0.43). Below, the observed growth rate dependence and the relation between tin content and ZTO growth rate, using a model based on the analysis of the precursor surface chemistry will be discussed.

X-ray photoelectron spectroscopy (XPS) was performed to verify the elemental composition of Zn, Sn and O, for the films of varying bilayer period described in Table 6.1. Figure 6.4 shows an XPS survey scan for a film with a low degree of lamination, Λ = 400 and c_{Sn} = 0.38 from ICP-OES. No contaminants are observed after removal of adventitious surface carbon by Ar^+ sputtering, which is representative for the other films investigated here. As this also holds for the binary films [314, 315], it is concluded that this thermal ZTO ALD process deposits films of high purity.

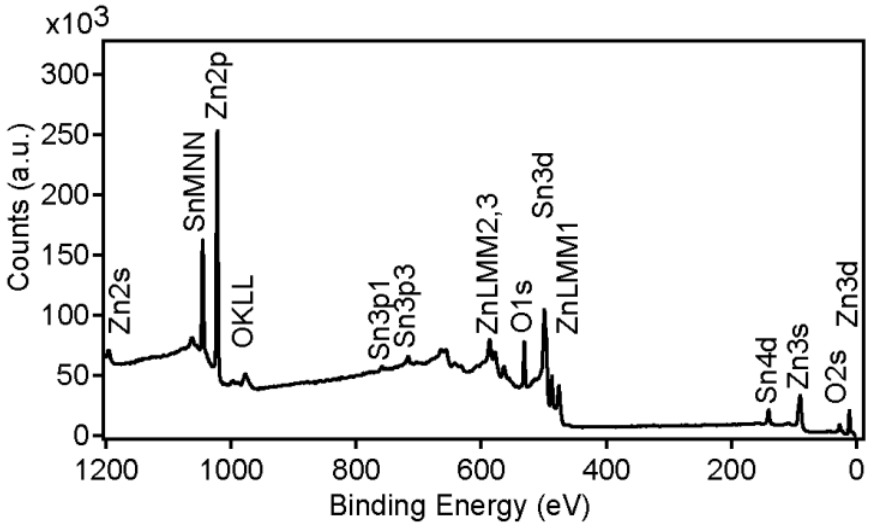


Figure 6.4. X-ray photoelectron spectroscopy survey scan of ZTO deposited on Si(100) at 150 ºC after Ar^+ sputtering for 12 s for Λ = 400 and c_{Sn} = 0.38 from ICP-OES.

Film morphology as a function of increasing Λ using SEM was also studied (Figure 6.5). The films appeared to be smooth and without large and distinct crystalline domains for all degrees of lamination studied, with a morphology resembling that of pure amorphous SnO_x [76, 314]. Although the domains are not large, their sizes increase as a function of increasing Λ.

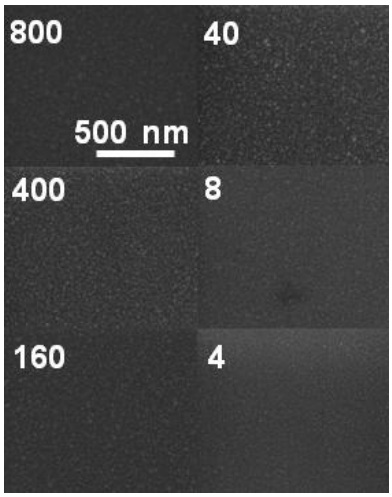


Figure 6.5. Plan-view, high-resolution SEM images for with bilayer period, Λ, overlaid under the conditions described in Table 6.1.

6.3.2. ZTO Properties as a Function of Composition

The influence of the composition on the film growth and properties is explored in this section. Because film characteristics was seen to vary significantly as a bilayer period, this parameter was fixed to a value to 6 to examine the role of composition for the ZTO film properties. With a fixed total number of cycles $A = 600$ and a number of super cycles $S = 100$, the tin cycle fraction, f_{Sn}, was sampled in multiples of 1/6.. Details of these experiments for each sampled value of f_{Sn} are summarized in Table 6.2.

Table 6.2. Summary of ZTO experiments as a function of Sn cycle fraction across a duplicate of samples. Systematic variation of tin cycle fractions, f_{Sn} =Sn/(Sn+Zn), gave rise to changes in Sn composition fraction, c_{Sn}, determined by ICP-OES and influenced growth rate, determined by VASE. Constants were total number of ZTO ALD cycles, 600, total number of super cycles, S=100 and degree of lamination, Λ= 6. Films were deposited at 150 ºC on Si(100) and fused-silica quartz.

Sn Cycle Fraction, f_{Sn} = Sn/(Sn+Zn)	**Average Sn Composition Fraction, c_{Sn}**	**Average Growth Rate (Å/cycle)**
0.00	0.00	1.92
0.17	0.10	1.35
0.33	0.20	1.18
0.50	0.31	0.79
0.67	0.50	0.83
0.83	0.48	0.80
1.00	1.00	0.84

The growth rates for films averaged over two sample sets are plotted against the Sn/(Sn+Zn) cycle fraction, f_{Sn}, in Figure 6.6. The two endpoints on the plot, f_{Sn}=0 and f_{Sn}=1.0, correspond to the two binary systems, ZnO and SnO_x. Based on a linear interpolation between the two binary growth rates, the observed growth rate for the intermixed system is lower than expected.

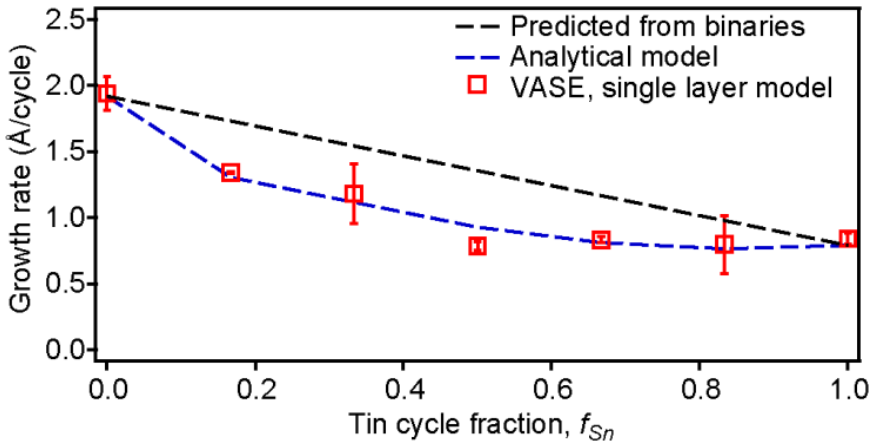


Figure 6.6. Film growth characteristics determined by VASE (red squares) and an analytical model described by Equation 5 (blue dashed line) as a function of tin cycle fraction. For reference, the growth rates linearly interpolated from the binary ALD processes.

The decreased ZTO ALD growth rates observed as a function of f_{Sn} resemble the growth behavior of the mixed ZnO/Al_2O_3 ALD process, an analogue to ZTO ALD, reported by George and Elam [141]. They deposited ZnO/Al_2O_3 from DEZn and trimethylaluminum (TMA) with H_2O as the oxygen source. Supported by detailed quartz crystal microbalance (QCM) experiments, the authors discuss potential causes for the reduced ZnO/Al_2O_3 ALD growth, and these include etching of surface Zn by TMA, deficiency of hydroxyl groups on the binary surfaces and surface hydroxyls that are less reactive to the TMA and DEZn reactants. The same arguments apply for ZTO ALD, except for the etching, which in the ZnO/Al_2O_3 system was attributed to two processes: (1) the transfer of CH_3 from TMA to surface Zn and concomitant release of DMZn and (2) the formation of thermodynamically stable $ZnAl_2O_4$ spinel. Etching in ZTO ALD could take place via cleaving a C-N bond in a DMA ligand of TDMASn followed by forming DMZn and a C-Zn bond, but this is hindered by a stronger C-N bond, with a bond strength of about 82 kcal/mol in $HN(CH_3)_2$ [317] as compared to the

C-Zn bond having a bond strength of about 64 kcal/mol [318]. Notably, Al-C bond has a bond strength practically equal with the bond strength of C-Zn in DMZn [319]. Accordingly, the observed reduced ZTO ALD growth is likely to originate from reduced surface hydroxyl density and/or less reactive surface hydroxyls.

Analysis of the ZTO growth rate behavior provides insight into the origin of the growth rate reduction. According to Figure 6.6, the growth rate drops about 30% when mixing a cycle of SnO_x with five cycles of ZnO within a super cycle (f_{Sn} = 0.17), and then at higher f_{Sn} converges toward the growth rate of pure SnO_x ALD. To model the ZTO growth, we calculated growth rates for ZTO films deposited at f_{Sn} = 0 – 1 by assuming that ZnO growth rate after SnO_x cycle(s) is reduced and then linearly restored during the subsequent ZnO cycles. ZnO growth rates reduced by factors of 1/6, 2/6, 3/6, and 5/6, and restoration of the ZnO growth rate in 1, 2, 3, 4, and 5 ZnO cycles were considered. Thus, the growth rates (r_{ZTO}) were calculated from

$$r_{ZTO} = \frac{1}{(n_{ZnO} + n_{SnOx})}\left[r_{SnOx} n_{SnOx} + r_{ZnO}(n_{ZnO} - n^*_{ZnO}) + r_{ZnO} \sum_{i=1}^{n^*_{ZnO}} \left(\frac{1}{3} + \frac{2}{3} \times \frac{i-1}{n^*_{ZnO}} \right) \right], \quad (6.5)$$

where r, n, and n^*_{ZnO} refer to growth rate, number of ZnO or SnO_x ALD cycles in a super cycle, and number of ZnO ALD cycles with reduced growth rate in a super cycle, respectively. The summation term provides the reduced ZnO growth rates. The best fit with experimental growth rates was obtained for ZnO growth rate reduced down to 2/6 of the pure ZnO growth rate and with restoration of the pure ZnO growth rate in 3 ZnO cycles, suggesting this to be the nucleation period for restoring the pure ZnO ALD

growth. Notably, a nucleation period of 4-6 ALD cycles was reported for ZnO in the ZnO/Al_2O_3 ALD on the basis of *in situ* QCM experiments [141].

It should be noted that for $f_{Sn} > 0.17$ the growth is affected also by surface disordering introduced by the deposition of amorphous ZTO (vide infra). Thus, the observed convergence of the growth rate towards pure SnO_x ALD is not only due to reduced ZnO growth but has complex contributions from the growth of amorphous material as well. More insight into the mechanistic details of the ZTO ALD growth mechanism will be provided by future theoretical investigations.

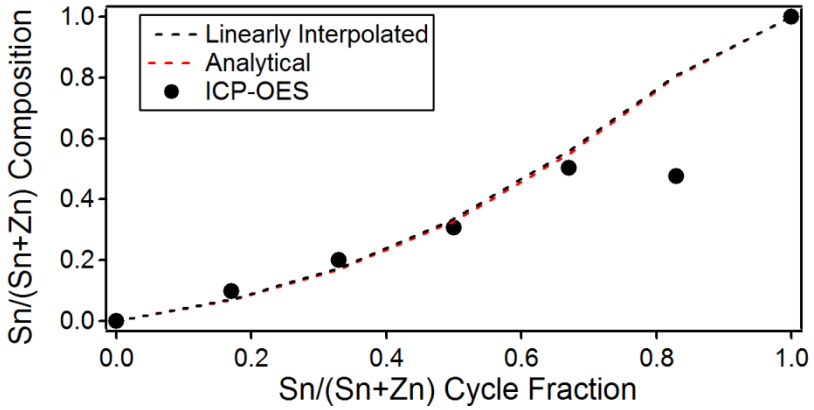


Figure 6.7. Composition of ZTO determined by ICP-OES, using an analytical model for the growth rate described by Equation 6.6 and linearly interpolated fractional Sn composition as a function of Sn/(Sn+Zn) cycle fraction, f_{Sn}. Number of ZTO ALD cycles, A= 600, number of super cycles, S = 100 and bilayer period, Λ = 6. Films were deposited on Si(100) at 150 ºC and each data point is an average over two data sets.

The reduced ZnO growth rates after SnO_x ALD cycles should be reflected in the ZTO composition as an excess of Sn with respect to the composition estimated from the growth rates and densities of the binaries. The relative metal compositions of the ZTO films deposited using a constant number of ALD cycles in a super cycle, the compositions calculated from the analytical ZTO growth rate from Equation 6.5, and linearly interpolated compositions calculated from the growth rates and densities of the

binaries (Equation 6.6, as shown below) are illustrated in Figure 6.7 as a function of tin cycle fraction, f_{Sn}. The interpolated compositions were calculated from

$$c_{Sn} = \frac{Sn}{Sn+Zn} = \left[n_{SnO_x} * \frac{\rho_{SnO_x} * r_{SnO_x}}{M_{SnO_x}} \right] \Bigg/ \left[n_{SnO_x} * \frac{\rho_{SnO_x} * r_{SnO_x}}{M_{SnO_x}} + n_{ZnO} * \frac{\rho_{ZnO} * r_{ZnO}}{M_{ZnO}} \right], \quad (6.6)$$

where r, n, ρ, and M refer to growth rate, number of ALD cycles in a super cycle, density, and molecular mass, respectively. Densities and molecular masses of both SnO and SnO_2 were used for SnO_x, but the results were practically equal and hence only results for SnO_2 were used in calculating the interpolated compositions. Values for densities of constituent binaries are as follows: ρ_{ZnO} = 5.61 g/cm^3, ρ_{SnO} = 6.45 g/cm^3 and ρ_{SnO2} = 6.95 g/cm^3 [320]. The experimentally-determined compositions from ICP-OES deviate from those calculated from manipulating the analytical ZTO growth rate equation (Equation 6.5) and those linearly interpolated at and above f_{Sn} = 0.83, further illuminating the complex effects on ZTO growth that originate from structural disordering as noted above.

Previous reports of as-deposited ZTO grown by ALD show that the films are largely amorphous [87-91]. To better understand the compositional behavior of the ZTO phases, we have characterized the structural properties of as-deposited films for a range of Sn cycle fractions, f_{Sn}, and compositions. Figure 6.8 shows diffraction patterns for the constituent binary oxides and intermediate ZTO compositions performed using grazing incidence x-ray diffraction (GIXRD). The diffraction patterns of the pure ZnO sample is characteristic of the hexagonal wurtzite phase, showing reflection of the (100), (002), (101) (110), (201) planes at 31.86º, 34.4,º 36.8,º 56.6, º and 69.1, º referenced to Cu-Kα, respectively. The peak broadening for these patterns is due to the limited

resolution of the two dimensional GIXRD experiment. For f_{Sn} = 0.17 (~10 % Sn), the film still shows patterns, albeit significantly broader and weaker for reflection of the (101), (002), (101) and (201) planes of hexagonal wurtzite ZnO. The result suggests that a small percentage of tin begins to decrease the long range order of the ZnO crystal. Beyond this composition, the films are x-ray amorphous, as is pure SnO_x [314], showing no reflections for ZnO, SnO, SnO_2, Zn_2SnO_4 or $ZnSnO_3$. The consequences of the mixing of crystalline and amorphous materials on the atomic scale, as is the case in mixing ZnO and SnO_x, are poorly-understood [321]. An alternative route to exploring the optoelectronic properties of ALD of ZTO may be to choose a tin precursor that yields crystalline as-deposited films that are compatible with the ZnO ALD temperature window. A promising precursor with for future investigation is N^2,N^3-di-*tert*-butyl-butane-2,3-diamido-tin(II) synthesized by Heo et al. [58, 59].

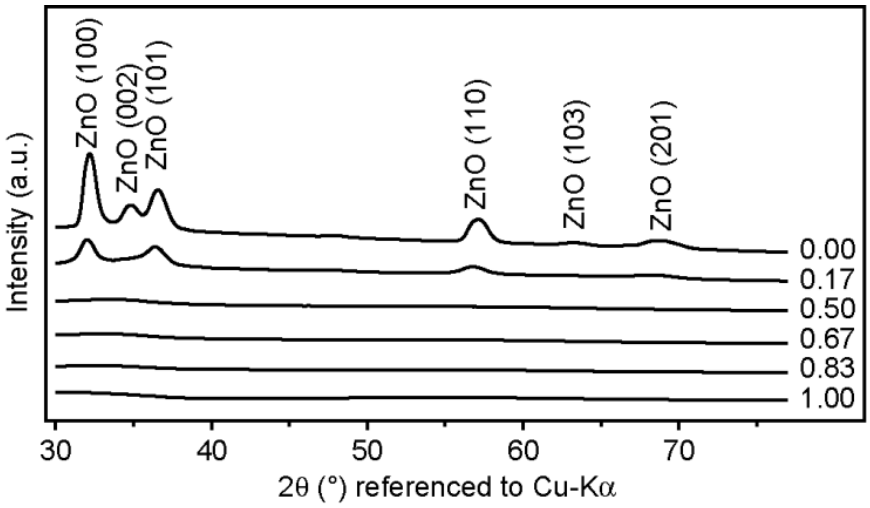


Figure 6.8. Grazing incidence x-ray diffraction (GIXRD) show patterns for a range of ZTO compositions sampled by Sn/(Sn+Zn) cycle fraction, f_{Sn}. Films of ZTO were deposited at 150º C on Si (100).

In sum, the XRD data show that the films have reflections along planes for hexagonal wurtzite ZnO then become amorphous, like pure SnO_x, for tin fractions, f_{Sn} exceeding 0.17 (~ 10% Sn); therefore, it may not be surprising that most of the films appear to resemble the morphology of pure SnO_x, as shown in Figure 6.9. A previous report on ZTO ALD shows films that resemble ours [87].

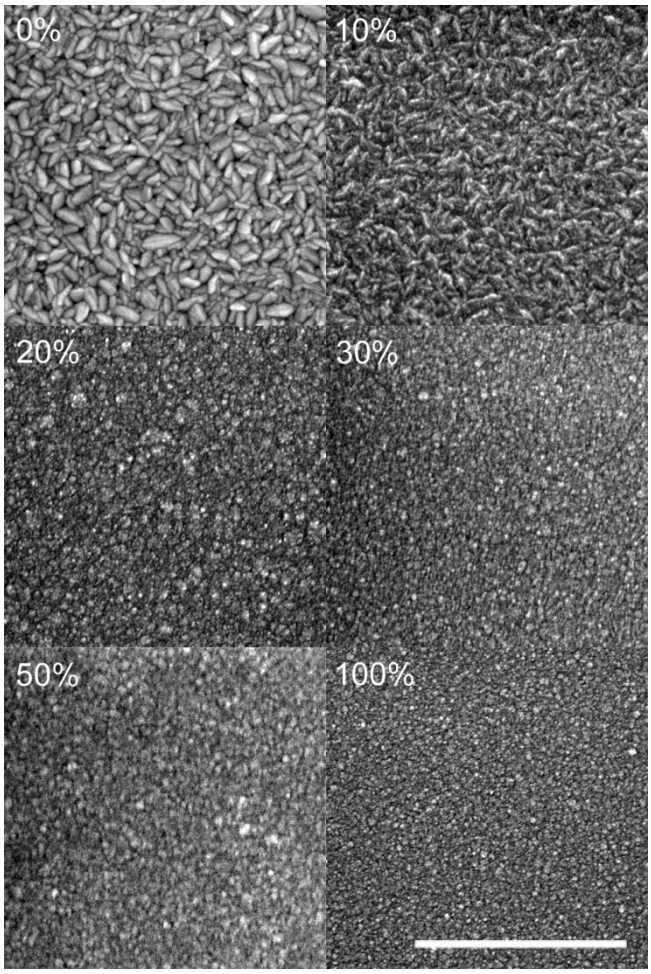


Figure 6.9. High resolution SEM images of ZTO on Si(100) with bilayer period, Λ=6, for A = 600 ZTO ALD cycles as a function of increasing percentages of tin from ICP-OES. The scale bar is 500 nm.

To explore the dependence of morphology on film thickness, we conducted two additional experiments to replicate the extreme cases of Sn composition fraction: (1) ~

10 % Sn (at f_{Sn} = 0.17) for half as many ZTO ALD cycles (300) and (2) ~ 50 % (at f_{Sn}= 0.83) for twice as many ZTO ALD cycles (1200). In the case of f_{Sn} = 0.17, the film thickness determined by VASE was ~504 Å and the morphology shown in Figure 6.10a shows less-defined domains compared to its counterpart in Figure 6.9. However, the domains are still sharper than for compositions with greater amounts of tin. For the other extreme case, f_{Sn} = 0.83 for 1200 ZTO ALD cycles, as shown in Figure 6.10b the film thickness was ~1056 Å and 56 % Sn. This tin-rich film shows a morphology that is similar to its counterpart in Figure 6.9. These findings suggest that differences in morphology are not only dependent on film thickness, but also likely due to variations in composition.

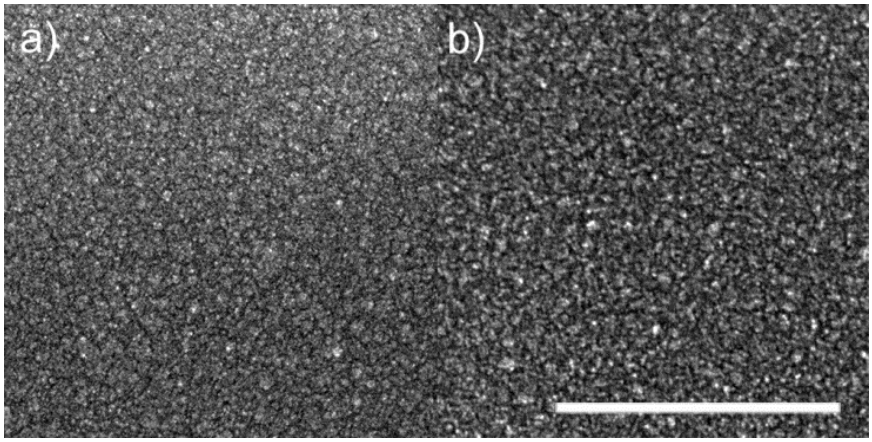


Figure 6.10. High resolution SEM images of ZTO on Si(100) with bilayer period, Λ=6 for (a) A = 300 ZTO ALD cycles for f_{Sn} = 0.17 and (b) A = 1200 ZTO ALD cycles for f_{Sn} = 0.83. The scale bar is 500 nm.

Spectroscopic ellipsometry was used to characterize the optical properties of the ZTO films grown on Si(100) as a function of the Sn cycle fraction Sn/(Sn+Zn), and thus composition (Figure 6.11). This may be the first comprehensive report of optical constants over a full range of compositions for ZTO by thermal ALD. An oscillator model was used to represent the optical properties of the ZTO films. This included a

polynomial spline function (the psemi-m0 oscillator[322]), a Lorentz oscillator and poles on each side of the spectrum to represent the optical constants of the films in a Kramers-Kronig consistent manner. A multi-sample analysis was used to fit a common set of oscillator parameters to samples sharing the same cycle fraction of Sn. However, film thicknesses were allowed to vary individually for each sample in the analysis. As a control for the ellipsometry results, light extinction at normal incidence was also analyzed over a wavelength range from 200 to 1000 nm for films deposited on fused silica quartz in the same ALD runs, as shown in Figure 6.11c. The general trends and features including absorption onset show good agreement with the extinction coefficients obtained from VASE.

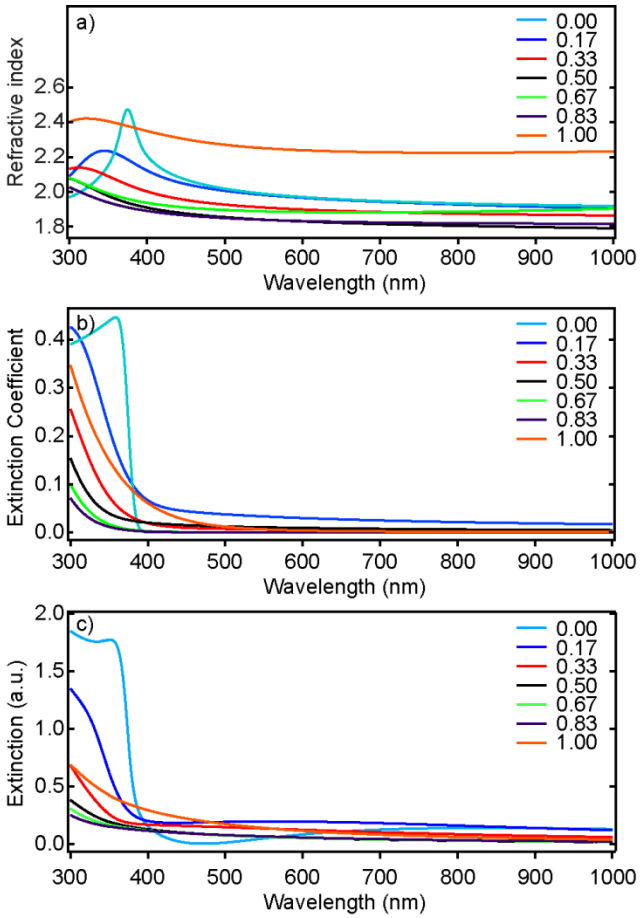


Figure 6.11. Spectroscopic ellipsometry results for (a) refractive index and (b) extinction coefficient vs. wavelength for ZTO on Si(100) over a range of tin cycle fractions (indicated in the color-coded legend in the upper right hand corner of each plot). For comparison, optical extinction vs. wavelength from measurements of the ZTO transmittance on fused silica is also included in (c).

For pure ZnO, the extinction coefficient displays a characteristic, sharp and direct type bandgap (Figure 6.11b). The introduction of low levels of Sn appears to increase the absorption over the entire visible range. This could, for instance, be due to defects associated with a more disordered phase, and/or free carrier-like absorption as the Sn act as an n-type dopant in the ZnO [323]. For intermediate ZTO compositions, the refractive index shown in Figure 6.11a drops with increasing Sn content. For the pure SnO_x, however, the refractive index increases quite dramatically. This is accompanied

by a drop in the bandgap size as well, as seen in Figure 6.11b and further discussed below. Although crystalline features were not observed by XRD for SnO_x, it is still possible that these changes are associated with a transition from an amorphous to a more crystalline phase but with very small grains.

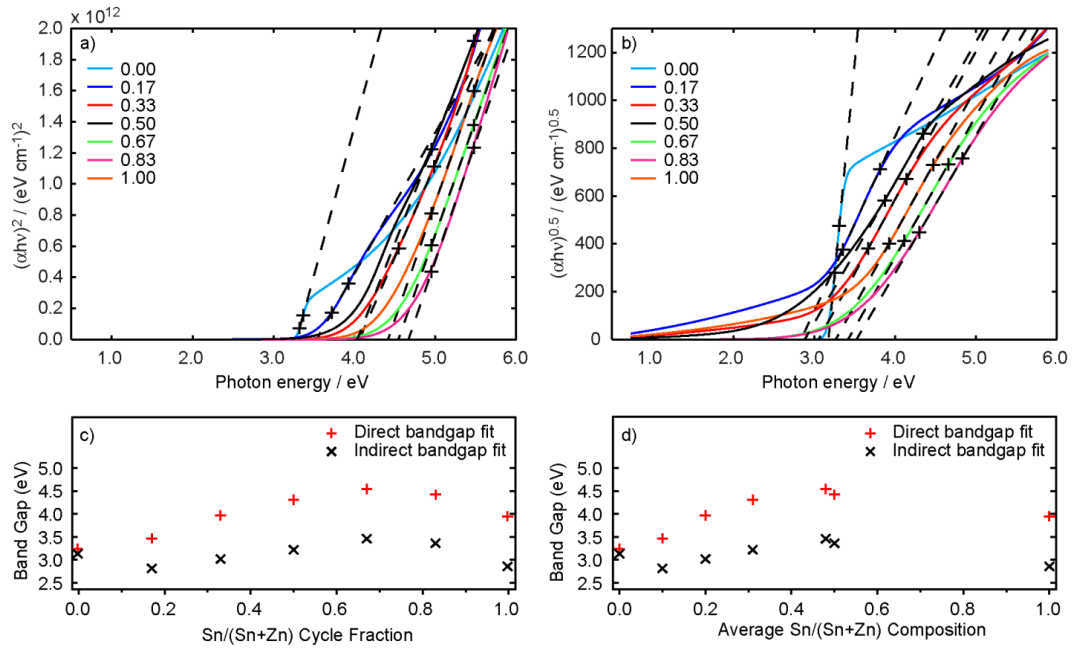


Figure 6.12. VASE multi-sample analyses of bandgaps for a range of ZTO cycle fractions. The bandgaps are found by extrapolating linear portions of the function $(\alpha h\nu)^x$ to zero. In this expression, $h\nu$ is the photon energy and α the absorption coefficient ($\alpha = 4\pi k/\lambda$ with k the extinction coefficient of the material, as determined by VASE). For the direct type bandgap fits in (a), the exponent x = 2, while for the indirect or amorphous type bandgap in (b), x = 0.5. The tin cycle fractions are indicated in the legends. The results are summarized versus the Sn cycle fraction, f_{Sn}, in (c), and versus the composition c_{Sn}, in (d).

To analyze the bandgaps, extrapolations of linear segments in the absorption onset region were performed as shown in Figure 6.12 As it is not clear what bandgap type is most appropriate for the intermediate compositions, fits to both direct and indirect/amorphous type bandgaps are presented in Figure 6.12a and b, respectively. XRD data has shown that for cycle fractions exceeding f_{Sn} = 0.17, these films are x-ray

amorphous. The extracted amorphous type bandgaps deviate more from the direct bandgaps with increasing SnO_x content, and follows a less trivial saw-tooth dependence with peak bandgap values for intermediate SnO_x content. Interestingly, Kapilashrami et al. observed a similar dependence for amorphous ZTO ALD films by soft x-ray spectroscopy [90].

6.4. Conclusions

The structural and optical properties of zinc tin oxide deposited by thermal ALD over a range of metal fractions, including the binary oxides, and for various bilayer periods of the ZnO and SnO_x phases are reported. Non-trivial dependences on these parameters were observed for the ALD growth rates, structural and optical properties. Growth rates decreased with increasing amounts of tin (~ 1.93 Å/cycle for 0% to ~0.80 Å/cycle for 100% at 150 °C), and were lower than what would be expected from a linear interpolation of the growth rates of the binary oxides. An analytical model accounting for this decreased growth was developed to provide insight into the reduced growth. X-ray diffraction showed that the crystallinity of the pure ZnO is largely lost when the fraction of tin exceeds 10%. As for the structural properties, the optical characteristics are found sensitive to increased tin content. Optical constants derived by spectroscopic ellipsometry are presented for the whole range of compositions, and used to determine the optical bandgaps. The direct bandgap of ZnO was found to be 3.3 eV. At 10% Sn concentration, a fit to an amorphous type bandgap gave a value of 2.8 eV, which increased to about 3.4 eV at 50% concentration and then decreased for pure SnO_x (~2.9 eV). The refractive index of the intermediate compositions decreased with tin content over a wide spectral range, but increased to a maximum for the pure SnO_x film,

concomitant with the bandgap reduction. This mild ZTO ALD process may be easily adapted for use in thin film solar cells and in thin film transistors. Because the ALD processes for these binary metal oxides are reproducible at near-room temperature [314, 315], this ZTO ALD process may also be used in systems where low-temperature processing is required, such as for biological and organic electronic applications.

Chapter 7. Conclusions

7.1. General Conclusions

The previous chapters of this thesis have showed how ALD can be used to control the spatial deposition and composition of conductive materials. One of the conductive materials studied was Pt, a highly effective yet extremely scarce catalyst, whose demand increases in spite of its prohibitive cost. Placing platinum only where needed helps to economize the use of this scarce and expensive material. Furthermore, feature size and spacing of materials on the nanoscale influence catalytic behavior; therefore being able to control these parameters may provide insight into the development of more powerful platinum catalysts. The use of area-selective atomic layer deposition (AS-ALD) of Pt and using microcontact printing (μCP) of a water-soluble polymer, polymethacrylamide (PMAM) as an ALD resist, is detailed in Chapter 3 and as a published work [42]. The use of octadecyltrichlorosilane (ODTS) self-assembled monolayer (SAM) defect sites to serve as nucleation templates to control the aerial density and size of Pt nanoparticles deposited via ALD is described in Chapter 4 and as a published work [248].

The other conductive material studied was zinc tin oxide (ZTO), because of its potential as an indium-free photovoltaic component and as a transparent conducting oxide (TCO) in high-end electronics. Because ZTO conduction behavior, certain optical characteristics and other useful material properties are not well understood as a function of composition, having nanoscale control over its growth may be an effective approach to learning more. As a result, ALD was explored as a flexible system for sampling a variety of compositions and varying the degree to which the films are

laminated. The ALD growth rate as well as structural and optical properties of these films were characterized and shown to vary significantly as a function of bilayer period and composition. These findings suggest that having nanoscale control over these film characteristics is critical in further understanding ZTO material properties. The details of this work are presented in Chapters 5 and 6.

7.2. Future Experimental Directions for ALD of Conductive Materials

7.2.1. Area-Selective ALD (AS-ALD)

The work described for the selective growth of Pt via ALD using SAM templates and μCP may provide groundwork for further studies. For either selective growth template for Pt ALD, electrochemical methods could be used to determine how the nanoparticles or stamped features affect catalytic ability in comparison with ultrathin films of similar thickness. Previous Bent Research Group electrochemical studies have examined the influence of Pt thin films as an electrode/catalyst layer for solid oxide fuel cells [187]. It may be possible to modify this system so that the electrode consists of nanoparticles or μCP features of Pt in order to compare current-voltage characteristics with previous thin film results.

In the case of μCP of PMAM, the polymer template can be easily removed via sonication in water, as described in Chapter 3, to avoid organic contamination during electrochemical experiments. As a result, this system may lend itself to greater ease in experimental design. More sophisticated equipment, such as an oxygen plasma chamber, would be needed to remove the ODTS SAMs before electrochemical characterizations. If these experiments show that nanoparticles or small features of Pt deposited using area-selective ALD (AS-ALD) significantly improve catalytic ability,

parallel and further studies may involve examining other organic growth templates and catalytic ALD systems.

7.2.2. Future Studies for ZTO ALD Film Characterization

A major finding of the ZTO ALD work presented in the Chapter 6 is the significance of film lamination on ALD growth characteristics. At the heart of this idea may be better understanding how different materials grow on one another. Characterizing the first few Ångstroms of ZnO deposited on SnO_x or vice-versa may be challenging to perform, so perhaps in-situ ALD with a variety of characterization tools may be one route to this end. For these in-situ studies, it is likely that a new ALD chamber would need to be built with many components, which may include XPS, AFM, TEM and the ability to be compatible with high-resolution grazing incidence x-ray diffraction (GIXRD) with different beam lines at a synchrotron radiation source such as SSRL. The long-term benefit of these potential in-situ experiments may make the development of such a system worthwhile; however the costs may be high in terms of time and money. In the interim, well-designed experiments with ex-situ film characterization may be a more efficient route to learning more about ZTO film growth..

One approach to determining growth of the binary metal oxides on each other may be to characterize the interface between larger film thicknesses of ZnO and SnO_x. Instead of trying to characterize films of a few Ångstroms of one material on its counterpart, characterizing tens of nanometers of the interface may be more straightforward to do. Similar techniques described above for in-situ analysis may be applied for these ex-situ studies. Furthermore, electrical techniques such as the four-point probe method and Hall measurements may provide insight into how conduction

and carrier concentration vary at the interface. Once these interfacial characteristics on the nanoscale are better understood, techniques that are also sensitive on the Ångstrom scale such as AFM and spectroscopic ellipsometry may be applied to interfaces of decreasing film thickness.

Whether in-situ or ex-situ routes are taken for these future ZTO ALD studies, film crystal phase will be an important parameter to address. So far, there have not been any rigorous studies in the ALD literature for electrical properties as a function of crystal structure for ZTO films. To better understand conduction behavior and various optical and structural properties as functions of composition and film lamination producing crystalline films will be helpful. As shown in Chapter 6, the ZTO ALD system resulted in amorphous as-deposited films, where the ZnO ALD system produces as-deposited polycrystalline films and the SnO_x system, amorphous films. For the same ZTO ALD system, performing film temperature anneal studies as a function of these properties may be one approach. An alternative method would be synthesizing or getting access to a compatible tin oxide precursor with a crystalline as-deposited rutile SnO_2 phase.

7.3. Outlook for ALD Scale-up for Industrial Applications

Early ALD processes were concerned with electroluminescence displays, semiconductor materials and understanding epitaxial growth [5, 9]. In the semiconductor industry, consumer demand for smaller and more powerful devices and keeping pace with Moore's law have increased interest in ALD for the growth of ultra thin films on increasingly complex three-dimensional structures [28, 29]. Though the concept of ALD was first described in the 1970s [5, 9], applications in industry are in

their relative infancies. As a result, there is still much to be discovered and learned from using this technique. Some of exciting opportunities are described in the next sections.

7.3.1. ALD in the Semiconductor Industry

Beginning with the turn of the twenty-first century, the semiconductor industry started to use ALD reactors for critical layers on surfaces with complex geometries. For instance, dynamic random-access memory (DRAM) manufacturers began using ALD for conformal deposition of high-κ dielectrics in high aspect ratio capacitor structures [5, 324]. Though specific details are proprietary, it is reported that Intel has used ALD in multiple areas of the 22 nm logic process flow and specifically in a tri-gate CMOS transistor [4, 324]. Because Intel is one of the most powerful companies in the semiconductor industry whose advances in transistor technology drives the market, its use of ALD may be an indication that this technique is well-poised for wider-scale industrial application.

7.3.2. ALD in the Photovoltaics (PV) Industry

7.3.2.1. Precedence for ALD in PV Applications

Outside of semiconductors, the photovoltaics (PV) industry is showing interest in using ALD as means of carefully nanoengineering solar cell interfaces for the growth of buffer layers, passivating surfaces and moisture permeation barriers [325]. ALD has already been used for Al_2O_3 passivation layers and stacks of Al_2O_3-SiN and Al_2O_3-SiO_2 for Cu(In,Ga)Se_2 (CIGS) solar cells [326]. In the past, ALD has been used to grow CdS

buffer layers for CIGS solar cells [325]. For the purpose of finding earth-abundant, non-toxic and oftentimes less costly alternatives, there have been recent advances in the ALD of cadmium-free buffer layers including ZTO, (Zn,Mg)O, Zn(O,S) and In_2S_3 [325, 327].

7.3.2.2. High Throughput ALD: Scale up for PV Industrial Applications

According to van Delft et al., successful industrial scale-up of ALD for PV lies in reactor design in order to combat traditional time-inefficient processes [325]. High-throughput ALD may be accomplished by batch reactions, spatial processes, roll-to-roll methods and the use of large-area substrates.

Batch processing of multiple wafers could drastically reduce the ALD process time, but some disadvantages may be low tolerance for poorly-optimized chemistries and single-sided deposition only [60, 63, 325]. In spite of these drawbacks, batch ALD may be useful for well-controlled ALD systems such as for high-quality Al_2O_3 surface passivation layers for crystalline silicon (c-Si) solar cells [60]. Beneq, a Finnish ALD equipment company, has commercialized a reactor for this very purpose with a batch size of 500 wafers and a process rate of 3200 wafers per hour with 20 nm thick Al_2O_3 films [328].

Another approach for decreasing ALD process time for industrial scale up is in-line spatial ALD. In spatial ALD, cycles take place in a spatial domain so that the precursor and reactant pulsing occur at different positions using different reaction zones separated by domains of purge gases [325]. Depending on reactor configuration, either the substrate or ALD deposition head moves in order to create these spatially separated reaction zones. Suntola patented the basic concept of spatial ALD in 1983 [329]. Levy

et al. of Eastman-Kodak were the first to publish findings using spatial ALD [330, 331]. Currently, SoLayTec and Levitech are two companies that are developing spatial ALD reactors for deposition of Al_2O_3 passivating layers [325].

Another approach to making ALD more time-efficient has been through the design of reactors to process large-area substrates. For example, Beneq has developed a crossflow reactor for Cd-free buffer layers capable of depositing 20 nm of Zn(O,S) on 60 x 120 cm^2 CIGS panels with a throughput of 24 panels per hour [328]. Another reactor design under development is for a roll-to-roll process where precursor gasses are confined in certain volumes and a flexible substrate is transferred through these volumes to enable the appropriate level of exposure [325]. In the Beneq WCS 500 roll-to-roll ALD reactor, a flexible substrate is attached to a feed-in reel through an ALD process drum which is exposed to an ALD contact head and exits via a take-up reel [325, 328]. For a film thickness of 25 nm, the output for this reactor is ~400,000 m^2/year [328].

Whatever the design of the ALD reactor, the diversity of options for increasing throughput to deposit high-quality materials makes ALD a strong candidate for use in the PV and semiconductor industries. As advances are made in the processing of flexible substrates under mild operating conditions, potential for integration into applications for biological and organic electronics applications are likely to follow.

Chapter 8. References

[1] G. Moore, Electronics 38/8 (1965).
[2] K. Seshan, Handbook of Thin Film Deposition, Elsevier Science, 2012.
[3] M. Bohr, Electron Devices Meeting (IEDM), 2011 IEEE International, IEEE, p. 1.1. 1.
[4] C. Auth, Custom Integrated Circuits Conference (CICC), 2012 IEEE, 2012, p. 1.
[5] S.M. George, Chemical reviews 110/1 (2010) 111.
[6] M. Leskelä, M. Ritala, Thin Solid Films 409/1 (2002) 138.
[7] M. Leskelä, M. Ritala, Angewandte Chemie International Edition 42/45 (2003) 5548.
[8] R.L. Puurunen, Journal of Applied Physics 97 (2005) 121301.
[9] M. Ritala, M. Leskelä (Eds.), Atomic Layer Deposition, Academic Press: San Diego, CA, 2001.
[10] H. Kim, Surface & Coatings Technology 200/10 (2006) 3104.
[11] Z. Li, A. Rahtu, R.G. Gordon, Journal of the Electrochemical Society 153/11 (2006) C787.
[12] H. Kim, Journal of Vacuum Science & Technology B 21/6 (2003) 2231.
[13] B.S. Lim, A. Rahtu, R.G. Gordon, Nature Materials 2/11 (2003) 749.
[14] T. Aaltonen, M. Ritala, V. Sammelselg, M. Leskela, Journal of the Electrochemical Society 151/8 (2004) G489.
[15] T. Aaltonen, M. Ritala, T. Sajavaara, J. Keinonen, M. Leskela, Chemistry of Materials 15/9 (2003) 1924.
[16] Z.W. Li, S.T. Barry, R.G. Gordon, Inorganic Chemistry 44/6 (2005) 1728.
[17] X. Wang, S.M. Tabakman, H. Dai, Journal of the American Chemical Society 130/26 (2008) 8152.
[18] M.M. Frank, G.D. Wilk, D. Starodub, T. Gustafsson, E. Garfunkel, Y.J. Chabal, J. Grazul, D.A. Muller, Applied Physics Letters 86/15 (2005).
[19] M. Ritala, K. Kukli, A. Rahtu, P.I. Raisanen, M. Leskelä, T. Sajavaara, J. Keinonen, Science 288/5464 (2000) 319.
[20] P.D. Ye, G.D. Wilk, B. Yang, J. Kwo, S.N.G. Chu, S. Nakahara, H.J.L. Gossmann, J.P. Mannaerts, M. Hong, K.K. Ng, J. Bude, Applied Physics Letters 83/1 (2003) 180.
[21] P.D. Ye, G.D. Wilk, B. Yang, J. Kwo, H.J.L. Gossmann, M. Hong, K.K. Ng, J. Bude, Applied Physics Letters 84/3 (2004) 434.
[22] J.Y. Kim, S.M. George, Journal of Physical Chemistry C 114/41 (2010) 17597.
[23] L. Reijnen, B. Meester, A. Goossens, J. Schoonman, Chemical Vapor Deposition 9/1 (2003) 15.
[24] P. Sinsermsuksakul, J. Heo, W. Noh, A.S. Hock, R.G. Gordon, Advanced Energy Materials 1/6 (2011) 1116.
[25] E.B. Yousfi, B. Weinberger, F. Donsanti, P. Cowache, D. Lincot, Thin Solid Films 387/1-2 (2001) 29.
[26] A. Hand, Semiconductor International 26/5 (2003) 46.
[27] P. Singer, Semiconductor International 27/5 (2004) 40.
[28] M. Knez, K. Niesch, L. Niinistö, Advanced Materials 19/21 (2007) 3425.

[29] H. Kim, H.-B.-R. Lee, W.J. Maeng, Thin Solid Films 517/8 (2009) 2563.
[30] B.S. Sang, A. Yamada, M. Konagai, Japanese Journal of Applied Physics Part 2-Letters 37/2B (1998) L206.
[31] D. Hariskos, S. Spiering, M. Powalla, Thin Solid Films 480 (2005) 99.
[32] S.-M. Lee, E. Pippel, U. Goesele, C. Dresbach, Y. Qin, C.V. Chandran, T. Braeuniger, G. Hause, M. Knez, Science 324/5926 (2009) 488.
[33] D. Losic, G. Triani, P.J. Evans, A. Atanacio, J.G. Mitchell, N.H. Voelcker, Journal of Materials Chemistry 16/41 (2006) 4029.
[34] J. Huang, X. Wang, Z.L. Wang, Nano Letters 6/10 (2006) 2325.
[35] M. Knez, A. Kadri, C. Wege, U. Gosele, H. Jeske, K. Nielsch, Nano Letters 6/6 (2006) 1172.
[36] A.J. Bard, M.A. Fox, Accounts of Chemical Research 28/3 (1995) 141.
[37] Y. Hua, W.P. King, C.L. Henderson, Microelectronic Engineering 85/5-6 (2008) 934.
[38] X. Jiang, S.F. Bent, Journal of the Electrochemical Society 154/12 (2007).
[39] X. Jiang, S.F. Bent, Journal of Physical Chemistry C 113/41 (2009).
[40] H.-B.-R. Lee, K. Jaemin, K. Hyungjun, K. Woo-Hee, L. Jeong Won, H. Inchan, Journal of the Korean Physical Society 56/1 (2010).
[41] W. Lee, F.B. Prinz, Journal of the Electrochemical Society 156/9 (2009).
[42] M.N. Mullings, H.-B.-R. Lee, N. Marchack, X. Jiang, Z. Chen, Y. Gorlin, K.-P. Lin, S.F. Bent, Journal of the Electrochemical Society 157/12 (2010) D600.
[43] R.H.A. Ras, E. Sahramo, J. Malm, J. Raula, M. Karppinen, Journal of the American Chemical Society 130/34 (2008) 11252.
[44] A. Sinha, D.W. Hess, C.L. Henderson, Proceedings of the SPIE - The International Society for Optical Engineering 6519 (2007).
[45] H. Yueming, W.P. King, C.L. Henderson, Microelectronic Engineering 85/5-6 (2008).
[46] D.B. Farmer, R.G. Gordon, Electrochemical and Solid-State Letters 8/4 (2005) G89.
[47] D.B. Farmer, R.G. Gordon, Nano Letters 6/4 (2006) 699.
[48] C.F. Herrmann, F.H. Fabreguette, D.S. Finch, R. Geiss, S.M. George, Applied Physics Letters, vol. 87, American Institute of Physics, 2005, p. 123110.
[49] W.-H. Kim, S.-J. Park, J.-Y. Son, H. Kim, Nanotechnology 19/4 (2008).
[50] J.S. King, D. Heineman, E. Graugnard, C.J. Summers, Applied Surface Science 244/1-4 (2005) 511.
[51] J.S. Lee, B. Min, K. Cho, S. Kim, J. Park, Y.T. Lee, N.S. Kim, M.S. Lee, S.O. Park, J.T. Moon, Journal of Crystal Growth 254/3-4 (2003) 443.
[52] I.M. Povey, M. Bardosova, F. Chalvet, M.E. Pemble, H.M. Yates, Surface & Coatings Technology 201/22-23 (2007) 9345.
[53] H. Viirolä, L. Niinistö, Thin Solid Films 251/2 (1994) 127.
[54] X. Du, Y. Du, S. George, Journal of Vacuum Science & Technology A: Vacuum, Surfaces, and Films 23 (2005) 581.
[55] G. Choi, L. Satyanarayana, J. Park, Applied Surface Science 252/22 (2006) 7878.
[56] J.W. Elam, D.A. Baker, A.B.F. Martinson, M.J. Pellin, J.T. Hupp, The Journal of Physical Chemistry C 112/6 (2008) 1938.

[57] M.N. Mullings, C. Hägglund, J.T. Tanskanen, S.F. Bent, 2012.
[58] J. Heo, A.S. Hock, R.G. Gordon, Chemistry of Materials 22/17 (2010) 4964.
[59] J. Heo, S.B. Kim, R.G. Gordon, Journal of Materials Chemistry 22/11 (2012) 4599.
[60] E. Granneman, P. Fischer, D. Pierreux, H. Terhorst, P. Zagwijn, Surface and Coatings Technology 201/22-23 (2007) 8899.
[61] P. Poodt, A. Lankhorst, F. Roozeboom, K. Spee, D. Maas, A. Vermeer, Advanced Materials 22/32 (2010) 3564.
[62] J.I. Skarp, ECS Transactions 33/2 (2010) 447.
[63] P. Poodt, D.C. Cameron, E. Dickey, S.M. George, V. Kuznetsov, G.N. Parsons, F. Roozeboom, G. Sundaram, A. Vermeer, Journal of Vacuum Science & Technology A: Vacuum, Surfaces, and Films 30/1 (2012) 010802.
[64] B. Vermang, A. Rothschild, A. Racz, J. John, J. Poortmans, R. Mertens, P. Poodt, V. Tiba, F. Roozeboom, Progress in Photovoltaics: Research and Applications 19/6 (2011) 733.
[65] C.-J. Yang, Energy Policy 37/5 (2009) 1805.
[66] L.N. Lewis, J. Stein, Y. Gao, R.E. Colborn, G. Hutchins, Platinum Metals Review 41 (1997) 66.
[67] M.A. Kromer, F. Joseck, T. Rhodes, M. Guernsey, J. Marcinkoski, International Journal of Hydrogen Energy 34/19 (2009) 8276.
[68] N.H. Behling, B. Noriko Hikosaka, Fuel Cells, Elsevier, 2013, p. 423.
[69] N. Farrell, Coordination Chemistry Reviews 232/1-2 (2002) 1.
[70] J. Emsley, Nature's Building Blocks: An A-Z Guide to the Elements, Oxford University Press, 2003.
[71] S.M. Jasinksi, U.S. Geological Survey, Mineral Commodity Summaries 2012: "Platinum-Group Metals.", U.S. Geological Survey
2012.
[72] T. Aaltonen, A. Rahtu, M. Ritala, M. Leskelä, Electrochemical and Solid-State Letters 6/9 (2003) C130.
[73] W.M.M. Kessels, H.C.M. Knoops, S.A.F. Dielissen, A.J.M. Mackus, M.C.M.v.d. Sanden, Applied Physics Letters 95/1 (2009) 013114.
[74] C. Dücsö, N.Q. Khanh, Z. Horváth, I. Bársony, M. Utriainen, S. Lehto, M. Nieminen, L. Niinistö, Journal of The Electrochemical Society 143 (1996) 683.
[75] V.E. Drozd, V.B. Aleskovski, Applied Surface Science 82-
83/0 (1994) 591.
[76] J.W. Elam, D.A. Baker, A.J. Hryn, A.B.F. Martinson, M.J. Pellin, J.T. Hupp, Journal of Vacuum Science & Technology A: Vacuum, Surfaces, and Films 26/2 (2008) 244.
[77] S. Yu-Sheng, Z. Tian-Shu, Sensors and Actuators B: Chemical 12/1 (1993) 5.
[78] D. Kovacheva, K. Petrov, Solid State Ionics 109/3 (1998) 327.
[79] S. Baruah, J. Dutta, Science and Technology of Advanced Materials 12/1 (2011) 013004.
[80] T. Minami, Semiconductor Science and Technology 20 (2005) S35.
[81] T. Minami, Thin Solid Films 516/17 (2008) 5822.
[82] C.A. Hoel, T.O. Mason, J.F. Gaillard, K.R. Poeppelmeier, Chemistry of Materials 22/12 (2010) 3569.

[83] Y.J. Chang, D.H. Lee, G. Herman, C.H. Chang, Electrochemical and Solid-State Letters 10/5 (2007) H135.
[84] Y. Jeong, K. Song, D. Kim, C.Y. Koo, J. Moon, Journal of the Electrochemical Society 156/11 (2009) H808.
[85] S.K. Park, Y.H. Kim, H.S. Kim, J.I. Han, Electrochemical and Solid-State Letters 12/7 (2009) H256.
[86] R. Gordon, D. Pang, R. Broomhall-Dilard, X. Liu, J. Barton, Transparent conductors and barrier layers for thin-film solar cells, technical report, Harvard Univerity/NREL, 2001.
[87] W.S. Choi, Journal of Korean Physical Society 57 (2010) 1472.
[88] A. Hultqvist, M. Edoff, T. Törndahl, Progress in Photovoltaics: Research and Applications 19/4 (2010) 478.
[89] A. Hultqvist, C. Platzer-Björkman, U. Zimmermann, M. Edoff, T. Törndahl, (2011).
[90] M. Kapilashrami, C.X. Kronawitter, T. Törndahl, J. Lindahl, A. Hultqvist, W.-C. Wang, C.-L. Chang, S.S. Mao, J. Guo, Physical Chemistry Chemical Physics 14/29 (2012) 10154.
[91] J. Lindahl, J.T. Wätjen, A. Hultqvist, T. Ericson, M. Edoff, T. Törndahl, Progress in Photovoltaics: Research and Applications (2012) n/a.
[92] J.D. Plummer, Silicon VLSI Technology: Fundamentals, Practice, and Modeling, Pearson Education, 2009.
[93] M.J. Madou, Fundamentals of Microfabrication: The Science of Miniaturization, CRC, 2002.
[94] R. Bashir, F. Hebert, Journal of Vacuum Science & Technology B: Microelectronics and Nanometer Structures 18/4 (2000) 2008.
[95] R. Bashir, T. Su, J. Sherman, G. Neudeck, J. Denton, A. Obeidat, Journal of Vacuum Science & Technology B: Microelectronics and Nanometer Structures 18/2 (2000) 695.
[96] I.J. Raaijmakers, H. Sprey, A. Storm, T. Bergman, J. Italiano, D. Meyer, Journal of Vacuum Science & Technology B: Microelectronics and Nanometer Structures 17/5 (1999) 2311.
[97] F. Schäffler, Semiconductor Science and Technology 12/12 (1999) 1515.
[98] K. Choy, Progress in materials science 48/2 (2003) 57.
[99] H.O. Pierson, Handbook of Chemical Vapor Deposition: Principles, Technology and Applications, William Andrew, 1999.
[100] X.R. Jiang, S.F. Bent, Journal of Physical Chemistry C 113/41 (2009) 17613.
[101] A. Ulman, Chemical reviews 96/4 (1996) 1533.
[102] J.C. Love, L.A. Estroff, J.K. Kriebel, R.G. Nuzzo, G.M. Whitesides, Chemical Reviews-Columbus 105/4 (2005) 1103.
[103] M.H. Park, Y.J. Jang, H.M. Sung-Suh, M.M. Sung, Langmuir 20/6 (2004) 2257.
[104] C. Bae, H. Shin, J. Moon, M.M. Sung, Chem. Mater. 18/5 (2006) 1085.
[105] C. Bae, J. Moon, H. Shin, J. Kim, M.M. Sung, J. Am. Chem. Soc. 129/46 (2007) 14232.
[106] R. Chen, S.F. Bent, Advanced Materials 18/8 (2006) 1086.
[107] R. Chen, H. Kim, P.C. McIntyre, S.F. Bent, Chem. Mater. 17/3 (2005) 536.

[108] R. Chen, H. Kim, P.C. McIntyre, D.W. Porter, S.F. Bent, Appl. Phys. Lett. 86/19 (2005) 191910.
[109] X.R. Jiang, R. Chen, S.F. Bent, Surface & Coatings Technology 201/22-23 (2007) 8799.
[110] J. Hong, D.W. Porter, R. Sreenivasan, P.C. McIntyre, S.F. Bent, Langmuir 23/3 (2007) 1160.
[111] X. Jiang, S.F. Bent, J. Electrochem. Soc. 154/12 (2007) D648.
[112] X. Jiang, H. Huang, F.B. Prinz, S.F. Bent, Chem. Mater. 20/12 (2008) 3897.
[113] E. Färm, M. Kernell, M. Ritala, M. Leskela, Chem. Vapor Depos. 12/7 (2006) 415.
[114] R. Chen, S.F. Bent, Chemistry of Materials 18/16 (2006) 3733.
[115] W. Lee, N.P. Dasgupta, O. Trejo, J.-R. Lee, J. Hwang, T. Usui, F.B. Prinz, Langmuir 26/9 (2010) 6845.
[116] D. Kim, J. Yoon, H. Kim, Journal of Nanoscience and Nanotechnology 12/2 (2010) 1483.
[117] H.-B.-R. Lee, S.F. Bent, in: M. Knez, N. Pinna (Eds.), Atomic Layer Deposition of Nanostructured Materials, Wiley-VCH Verlag GmbH & Co. KGaA, Berlin, 2011, p. 193.
[118] J.P. Lee, M.M. Sung, J. Am. Chem. Soc. 126/1 (2004) 28.
[119] H.B.R. Lee, W.H. Kim, J.W. Lee, J.M. Kim, K. Heo, I.C. Hwang, Y. Park, S. Hong, H. Kim, J. Electrochem. Soc. 157/1 (2010) D10.
[120] W.R. Childs, R.G. Nuzzo, Adv. Mater. 16/15 SPEC. ISS. (2004) 1323.
[121] O. Lima, L. Tan, A. Goel, M. Negahban, Z. Li, J. Vac. Sci. Technol., B 25 (2007) 2412.
[122] J. Hong, D.W. Porter, R. Sreenivasan, P.C. McIntyre, S.F. Bent, Langmuir 23/3 (2006) 1160.
[123] R.H.A. Ras, E. Sahramo, J. Malm, J. Raula, M. Karppinen, J. Am. Chem. Soc. 130/34 (2008) 11252.
[124] E. Färm, M. Kemell, M. Ritala, M. Leskelä, Journal of Physical Chemistry C 112/40 (2008) 15791.
[125] A. Sinha, D.W. Hess, C.L. Henderson, J. Vac. Sci. Technol., B 24/6 (2006) 2523.
[126] A. Sinha, D.W. Hess, C.L. Henderson, Journal of the Electrochemical Society 153/5 (2006) G465.
[127] A. Sinha, D.W. Hess, C.L. Henderson, J. Vac. Sci. Technol., B 25/5 (2007) 1721.
[128] Y.M. Hua, W.P. King, C.L. Henderson, Microelectronic Engineering 85/5-6 (2008) 934.
[129] M.J. Biercuk, D.J. Monsma, C.M. Marcus, J.S. Becker, R.G. Gordon, Appl. Phys. Lett. 83/12 (2003) 2405.
[130] E. Färm, M. Kemell, E. Santala, M. Ritala, M. Leskela, J. Electrochem. Soc. 157/1 (2010) K10.
[131] A. Sinha, D.W. Hess, C.L. Henderson, Electrochem. Solid-State Lett. 9 (2006) G330.
[132] I. Hamberg, C.G. Granqvist, Journal of applied physics 60/11 (1986) R123.
[133] R.G. Gordon, Mrs Bulletin 25/8 (2000) 52.
[134] E. Fortunato, D. Ginley, H. Hosono, D.C. Paine, Mrs Bulletin 32/3 (2007) 242.
[135] T. Minami, H. Nanto, S. Shooji, S. Takata, Thin Solid Films 111/2 (1984) 167.

[136] G. Frank, H. Köstlin, Applied Physics A: Materials Science & Processing 27/4 (1982) 197.
[137] P. Nath, R.F. Bunshah, B.M. Basol, O.M. Staffsud, Thin Solid Films 72/3 (1980) 463.
[138] I.A. Rauf, Materials Letters 18/3 (1993) 123.
[139] A.C. Tolcin, U.S. Geological Survey, 2012, Mineral Commodity Summaries 2012 (2012) 74.
[140] H. Yuan, B. Luo, D. Yu, A. Cheng, S.A. Campbell, W.L. Gladfelter, Journal of Vacuum Science & Technology A: Vacuum, Surfaces, and Films 30/1 (2012) 01A138.
[141] J. Elam, S. George, Chemistry of Materials 15/4 (2003) 1020.
[142] T. Dhakal, D. Vanhart, R. Christian, A. Nandur, A. Sharma, C.R. Westgate, Journal of Vacuum Science & Technology A: Vacuum, Surfaces, and Films 30/2 (2012) 021202.
[143] S.C. Gong, Y.-J. Choi, H. Kim, C.-S. Park, H.-H. Park, J.G. Jang, H.J. Chang, G.Y. Yeom, Journal of Vacuum Science & Technology A: Vacuum, Surfaces, and Films 31/1 (2013) 01A101.
[144] J.Y. Kim, Y.-J. Choi, H.-H. Park, S. Golledge, D.C. Johnson, Journal of Vacuum Science & Technology A: Vacuum, Surfaces, and Films 28/5 (2010) 1111.
[145] P.R. Chalker, P.A. Marshall, S. Romani, M.J. Rosseinsky, S. Rushworth, P.A. Williams, J. Buckett, N. McSporran, J. Ridealgh, MRS Proceedings, Cambridge Univ Press, 2011.
[146] K. Saito, Y. Hiratsuka, A. Omata, H. Makino, S. Kishimoto, T. Yamamoto, N. Horiuchi, H. Hirayama, Superlattices and Microstructures 42/1 (2007) 172.
[147] C. C. Platzer-Björkman , T. Törndahl, A. Hultqvist, J. Kessler, M. Edoff, Thin Solid Films 515/15 (2007) 6024.
[148] J.R. Bakke, J.T. Tanskanen, C. Hagglund, T.A. Pakkanen, S.F. Bent, Journal of Vacuum Science & Technology A: Vacuum, Surfaces, and Films 30/1 (2012) 01A135.
[149] J. Heo, Y. Liu, P. Sinsermsuksakul, Z. Li, L. Sun, W. Noh, R.G. Gordon, The Journal of Physical Chemistry C 115/20 (2011) 10277.
[150] X. Jiang, R. Chen, S.F. Bent, Surface and Coatings Technology 201/22 (2007) 8799.
[151] R. Azzam, A.R.M. Zaghloul, N. Bashara, JOSA 65/3 (1975) 252.
[152] G. Jellison, Thin Solid Films 313 (1998) 33.
[153] H.G. Tompkins, E.A. Irene, Handbook of Ellipsometry, William Andrew, 2005.
[154] K.W. Kolasinski, Surface Science: Foundations of Catalysis and Nanoscience, Wiley, 2008.
[155] R.J. Good, Journal of Adhesion Science and Technology 6/12 (1992) 1269.
[156] S.R. Wasserman, Y.T. Tao, G.M. Whitesides, Langmuir 5/4 (1989) 1074.
[157] R. Chen, H. Kim, P.C. McIntyre, S.F. Bent, Integration of Advanced Micro- and Nanoelectronic Devices-Critical Issues and Solutions (Materials Research Society Vol.811) (2004).
[158] B.W. Rossiter, R.C. Baetzold, Physical Methods of Chemistry, Investigations of Surfaces and Interfaces, Wiley, 1992.
[159] J. Goldstein, Scanning Electron Microscopy and X-Ray Microanalysis, Kluwer Academic Pub, 2003.
[160] FEI, FEI Company, 2010.

[161] P. Echlin, Handbook of Sample Preparation for Scanning Electron Microscopy and X-Ray Microanalysis, Springer London, Limited, 2009.
[162] J.F. Moulder, W.F. Stickle, P.E. Sobol, K.D. Bomben, Handbook of X-ray Photoelectron Spectroscopy, ULVAC-Phi, Chigasaki, 1995.
[163] P. Auger, J. Phys. Radium 6/205 (1925).
[164] P. Auger, Compt. Rend. Acad. Sci. 180/65 (1923).
[165] S. Howard, Hidden Giants, 2nd Edition, Lulu.com, 2008.
[166] R.L. Sime, Lise Meitner: A Life in Physics, University of California Press, 1996.
[167] P.W. Palmberg, J. Appl. Phys. 38/213 (1967).
[168] E.J.S. L.N.Tharp., J. Appl. Phys. 38/13320 (1967).
[169] P.W. Palmberg, G.K. Bohn., J.C. Tracy, Appl. Phys. Lett. 15/254 (1969).
[170] C.D. Childs, B.A. Carlson, L.A. La Vanier, J.F. Moulder, D.F. Paul, W.F. Stickle, D.G. Watson, C.L. Hedberg (Eds.), Handbook of Auger Electron Spectroscopy, 3rd Edition, Physical Electronics, Inc., 1995.
[171] M. Che, J.C. Vedrine, Characterization of Solid Materials and Heterogeneous Catalysts, Wiley, 2012.
[172] D.L. Pavia, Introduction to Spectroscopy, Brooks/Cole, 2009.
[173] J. Tauc, Materials Research Bulletin 3/1 (1968) 37.
[174] E. Davis, N.F. Mott, Philosophical Magazine 22/179 (1970) 903.
[175] D. Wood, J. Tauc, Physical Review B 5/8 (1972) 3144.
[176] S.M. Sze, K.K. Ng, Physics of Semiconductor Devices, Wiley, 2006.
[177] A.R. West, Basic solid state chemistry, John Wiley & Sons, 1999.
[178] M.L. Weaver, 2011.
[179] M. Tisza, Physical Metallurgy for Engineers, ASM International, 2001.
[180] C.R. Brundle, C.A. Evans, S. Wilson, Elsevier Science & Technology Books, 1992, p. 633.
[181] J.W. Olesik, Analytical Chemistry 63/1 (1991) 12.
[182] S. George, A. Ott, J. Klaus, The Journal of Physical Chemistry 100/31 (1996) 13121.
[183] M.H. Park, Y.J. Jang, H.M. Sung-Suh, M.M. Sung, Langmuir 20/6 (2004) 2257.
[184] C. Bae, H. Shin, J. Moon, M.M. Sung, Chemistry of Materials 18/5 (2006) 1085.
[185] C. Bae, J. Moon, H. Shin, J. Kim, M.M. Sung, Journal of the American Chemical Society 129/46 (2007) 14232.
[186] R. Chen, H. Kim, P.C. McIntyre, D.W. Porter, S.F. Bent, Applied Physics Letters 86/19 (2005).
[187] X. Jiang, H. Huang, F.B. Prinz, S.F. Bent, Chemistry of Materials 20/12 (2008) 3897.
[188] H.B.R. Lee, W.H. Kim, J.W. Lee, J.M. Kim, K. Heo, I.C. Hwang, Y. Park, S. Hong, H. Kim, Journal of the Electrochemical Society 157/D10 (2010).
[189] W. Childs, R.G. Nuzzo, Advanced Materials 16/15 (2004) 1323.
[190] O. Lima, L. Tan, A. Goel, M. Negahban, Z. Li, Journal of Vacuum Science & Technology B: Microelectronics and Nanometer Structures 25/6 (2007) 2412.
[191] E. Färm, M. Kemell, M. Ritala, M. Leskelä, The Journal of Physical Chemistry C 112/40 (2008) 15791.
[192] A. Sinha, D.W. Hess, C.L. Henderson, Journal of Vacuum Science & Technology B: Microelectronics and Nanometer Structures 24/6 (2006) 2523.

[193] A. Sinha, D.W. Hess, C.L. Henderson, Journal of Vacuum Science & Technology B: Microelectronics and Nanometer Structures 25/5 (2007) 1721.
[194] M. Biercuk, D. Monsma, C. Marcus, J. Becker, R. Gordon, Applied Physics Letters 83/12 (2003) 2405.
[195] E. Färm, M. Kemell, E. Santala, M. Ritala, M. Leskelä, Journal of the Electrochemical Society 157/1 (2010) K10.
[196] A. Sinha, D.W. Hess, C.L. Henderson, Electrochemical and Solid-State Letters 9/11 (2006) G330.
[197] M. Kutz, Handbook of Materials Selection, Wiley, 2002.
[198] I. McNeill, M. Zulfiqar, Journal of Polymer Science: Polymer Chemistry Edition 16/10 (1978) 2465.
[199] R. Jones, S.B. Desu, MRS Bulletin 21/6 (1996) 55.
[200] J.L. Gland, B.A. Sexton, G.B. Fisher, Surface Science 95/2 (1980) 587.
[201] N.L. Jeon, W. Lin, M.K. Erhardt, G.S. Girolami, R.G. Nuzzo, Langmuir 13/14 (1997) 3833.
[202] B. Michel, A. Bernard, A. Bietsch, E. Delamarche, M. Geissler, D. Juncker, H. Kind, J.P. Renault, H. Rothuizen, H. Schmid, IBM Journal of Research and Development 45/5 (2001) 697.
[203] C.D. Wagner, G.E. Muilenberg, Handbook of X-ray Photoelectron Spectroscopy, Perkin-Elmer, 1979.
[204] M. Alexander, F. Jones, Carbon 32/5 (1994) 785.
[205] P.V. Kamat, The Journal of Physical Chemistry B 106/32 (2002) 7729.
[206] K.L. Kelly, E. Coronado, L.L. Zhao, G.C. Schatz, The Journal of Physical Chemistry B 107/3 (2002) 668.
[207] S.G. Penn, L. He, M.J. Natan, Current Opinion in Chemical Biology 7/5 (2003) 609.
[208] P. Ray, G. Darbha, A. Ray, J. Walker, W. Hardy, Plasmonics 2/4 (2007) 173.
[209] H. Zhang, S. Evans, J. Henderson, R. Miles, T. Shen, Nanotechnology 13/3 (2002) 439.
[210] I.H. El-Sayed, X. Huang, M.A. El-Sayed, Cancer Letters 239/1 (2006) 129.
[211] S.A. Ivanov, J. Nanda, A. Piryatinski, M. Achermann, L.P. Balet, I.V. Bezel, P.O. Anikeeva, S. Tretiak, V.I. Klimov, The Journal of Physical Chemistry B 108/30 (2004) 10625.
[212] D.M. Schaadt, B. Feng, E.T. Yu, Applied Physics Letters 86/6 (2005) 063106.
[213] R.D. Schaller, V.I. Klimov, Physical Review Letters 92/18 (2004) 186601.
[214] W.J.E. Beek, M.M. Wienk, R.A.J. Janssen, Advanced Functional Materials 16/8 (2006) 1112.
[215] Z. Liang, K.L. Dzienis, J. Xu, Q. Wang, Advanced Functional Materials 16/4 (2006) 542.
[216] S. Pillai, K.R. Catchpole, T. Trupke, M.A. Green, Journal of Applied Physics 101/9 (2007) 093105.
[217] M.S. Chen, D.W. Goodman, Science, vol. 306, American Association for the Advancement of Science, 2004, p. 252.
[218] D. Astruc, M.-C. Daniel, J. Ruiz, Chemical Communications 0/23 (2004) 2637.
[219] R. Ferrando, J. Jellinek, R.L. Johnston, Chemical Reviews 108/3 (2008) 845.
[220] M.A. El-Sayed, Accounts of Chemical Research 37/5 (2004) 326.

[221] J.W. Elam, D. Routkevitch, P.P. Mardilovich, S.M. George, Chemistry of Materials 15/18 (2003) 3507.
[222] J.S. Becker, S. Suh, S. Wang, R.G. Gordon, Chemistry of Materials 15/15 (2003) 2969.
[223] J.E. Crowell, Journal of Vacuum Science & Technology A: Vacuum, Surfaces, and Films 21/5 (2003) S88.
[224] A. Johansson, T. Törndahl, L.M. Ottosson, M. Boman, J.O. Carlsson, Materials Science and Engineering: C 23/6-8 (2003) 823.
[225] S.O. Kucheyev, J. Biener, Y.M. Wang, T.F. Baumann, K.J. Wu, T.v. Buuren, A.V. Hamza, J. J. H. Satcher, J.W. Elam, M.J. Pellin, Applied Physics Letters 86/8 (2005) 083108.
[226] T.P. Brennan, P. Ardalan, H.-B.-R. Lee, J.R. Bakke, I.K. Ding, M.D. McGehee, S.F. Bent, Advanced Energy Materials 1/6 (2011) 1169.
[227] N.P. Dasgupta, H.J. Jung, O. Trejo, M.T. McDowell, A. Hryciw, M. Brongersma, R. Sinclair, F.B. Prinz, Nano Letters 11/3 (2011) 934.
[228] H.-B.-R. Lee, H. Kim, Journal of Crystal Growth 312/15 (2010) 2215.
[229] S.T. Christensen, H. Feng, J.L. Libera, N. Guo, J.T. Miller, P.C. Stair, J.W. Elam, Nano Letters 10/8 (2010) 3047.
[230] J. Heo, D. Eom, S.Y. Lee, S.-J. Won, S. Park, C.S. Hwang, H.J. Kim, Chemistry of Materials 21/17 (2009) 4006.
[231] C. Liu, C.-C. Wang, C.-C. Kei, Y.-C. Hsueh, T.-P. Perng, Small 5/13 (2009) 1535.
[232] J. Lu, P.C. Stair, Langmuir 26/21 (2010) 16486.
[233] J.P. Lee, Y.J. Jang, M.M. Sung, Advanced Functional Materials 13/11 (2003) 873.
[234] E.K. Seo, J.W. Lee, H.M. Sung-Suh, M.M. Sung, Chemistry of Materials 16/10 (2004) 1878.
[235] K. Bierbaum, M. Kinzler, C. Woell, M. Grunze, G. Haehner, S. Heid, F. Effenberger, Langmuir 11/2 (1995) 512.
[236] T. Balgar, R. Bautista, N. Hartmann, E. Hasselbrink, Surface Science 532 (2003) 963.
[237] K. Bierbaum, M. Grunze, A.A. Baski, L.F. Chi, W. Schrepp, H. Fuchs, Langmuir 11/6 (1995) 2143.
[238] S.C. Clear, P.F. Nealey, Langmuir 17/3 (2001) 720.
[239] C.R. Kessel, S. Granick, Langmuir 7/3 (1991) 532.
[240] A. Ulman, Chemical Reviews 96/4 (1996) 1533.
[241] R. Chen, H. Kim, P.C. McIntyre, S.F. Bent, Applied Physics Letters 84/20 (2004) 4017.
[242] K. Niesz, M. Grass, G.A. Somorjai, Nano Letters 5/11 (2005) 2238.
[243] T.K. Sau, A.L. Rogach, Advanced Materials 22/16 (2010) 1781.
[244] C.-K. Tsung, J.N. Kuhn, W. Huang, C. Aliaga, L.-I. Hung, G.A. Somorjai, P. Yang, Journal of the American Chemical Society 131/16 (2009) 5816.
[245] H. Kim, S. Woo, S. Bang, Y. Kim, D. Choi, H. Jeon, Electrochemical and Solid-State Letters 12/4 (2009) H92.
[246] S.S. Yim, D.J. Lee, K.S. Kim, M.S. Lee, S.H. Kim, K.B. Kim, Electrochemical and Solid-State Letters 11/9 (2008) K89.

[247] R.H.A. Ras, E. Sahramo, J. Malm, J. Raula, M. Karppinen, Journal of the American Chemical Society 130/34 (2008) 11252.
[248] H.-B.-R. Lee, M.N. Mullings, X. Jiang, B.M. Clemens, S.F. Bent, Chemistry of Materials 24/21 (2012) 4051.
[249] J.L.G. Fierro, Metal Oxides: Chemistry And Applications, Taylor & Francis, 2006.
[250] H. Ogawa, A. Abe, M. Nishikawa, S. Hayakawa, Journal of the Electrochemical Society 128 (1981) 2020.
[251] K. Ishiguro, T. Sasaki, T. Arai, I. Imai, Journal of the Physical Society of Japan 13 (1958) 296.
[252] J.T. Jacobs, Electrical Properties of Tin Oxide Thin Films, University of Illinois at Urbana-Champaign, 1964.
[253] M. Batzill, U. Diebold, Progress in Surface Science 79/2-4 (2005) 47.
[254] P. Cox, The surface science of metal oxides, Cambridge Univ Pr, 1996.
[255] J. Watson, Sensors and Actuators 5/1 (1984) 29.
[256] B. Panchapakesan, D.L. DeVoe, M.R. Widmaier, R. Cavicchi, S. Semancik, Nanotechnology 12 (2001) 336.
[257] C.J. Martinez, B. Hockey, C.B. Montgomery, S. Semancik, Langmuir 21/17 (2005) 7937.
[258] A. Kolmakov, Y. Zhang, G. Cheng, M. Moskovits, Advanced Materials 15/12 (2003) 997.
[259] H. De Waal, F. Simons, Thin Solid Films 77/1 (1981) 253.
[260] M. Vergohl, N. Malkomes, T. Matthee, G. Brauer, U. Richter, F.W. Nickol, J. Bruch, Thin Solid Films 392/2 (2001) 258.
[261] R.G. Gordon, J. Proscia, F.B. Ellis Jr, A.E. Delahoy, Solar Energy Materials 18/5 (1989) 263.
[262] H. Klasens, Solid State Electronics 7 (1964) 701.
[263] H.K. Liao, J.C. Chou, W.Y. Chung, T.P. Sun, S.K. Hsiung, Sensors and Actuators B: Chemical 50/2 (1998) 104.
[264] F. Chen, M. Liu, Chem. Commun./18 (1999) 1829.
[265] P. Gao, Y. Ding, Z. Wang, Nano letters 3/9 (2003) 1315.
[266] A. Hagemeyer, Z. Hogan, M. Schlichter, B. Smaka, G. Streukens, H. Turner, A. Volpe, H. Weinberg, K. Yaccato, Applied Catalysis A: General 317/2 (2007) 139.
[267] S. Ferrere, A. Zaban, B.A. Gregg, The Journal of Physical Chemistry B 101/23 (1997) 4490.
[268] S.C. Lee, J.H. Lee, T.S. Oh, Y.H. Kim, Solar energy materials and solar cells 75/3 (2003) 481.
[269] R. Gordon, Journal of Non-Crystalline Solids 218 (1997) 81.
[270] J. Proscia, R.G. Gordon, Thin Solid Films 214/2 (1992) 175.
[271] R.B.H. Tahar, T. Ban, Y. Ohya, Y. Takahashi, Journal of Applied Physics 83 (1998) 2631.
[272] G. Sanon, R. Rup, A. Mansingh, Thin Solid Films 190/2 (1989) 287.
[273] Y.C. Lee, O.K. Tan, M.S. Tse, A. Srivastava, Ceramics International 30/7 (2004) 1869.
[274] J. Kane, H. Schweizer, W. Kern, Journal of The Electrochemical Society 122 (1975) 1144.

[275] R. D. Tarey, T.A. Raju, Thin Solid Films 128/3â€“4 (1985) 181.
[276] J. Sundqvist, J. Lu, M. Ottosson, A. Hårsta, Thin Solid Films 514/1-2 (2006) 63.
[277] S.H. Park, Y.C. Son, W.S. Willis, S.L. Suib, K.E. Creasy, Chemistry of Materials 10/9 (1998) 2389.
[278] V. Brinzari, G. Korotcenkov, V. Golovanov, Thin Solid Films 391/2 (2001) 167.
[279] G. Sberveglieri, Sensors and Actuators B: Chemical 6/1-3 (1992) 239.
[280] M. Utriainen, H. Lattu, H. Viirolä, L. Niinistö, R. Resch, G. Friedbacher, Mikrochimica Acta 133/1-4 (2000) 119.
[281] D.H. Kim, J.-H. Kwon, M. Kim, S.-H. Hong, Journal of Crystal Growth 322/1 (2011) 33.
[282] J.J. Robbins, R.T. Alexander, M. Bai, Y.J. Huang, T.L. Vincent, C.A. Wolden, Journal of Vacuum Science & Technology A: Vacuum, Surfaces, and Films 19 (2001) 2762.
[283] J. Sundqvist, J. Lu, M. Ottosson, A. Harsta, Thin Solid Films 514/1-2 (2006) 63.
[284] J. Sundqvist, A. Tarre, A. Rosental, A. Harsta, Chemical Vapor Deposition 9/1 (2003) 21.
[285] A. Yamada, B.S. Sang, M. Konagai, Applied Surface Science 112 (1997) 216.
[286] B.S. Sang, M. Konagai, Japanese Journal of Applied Physics Part 2-Letters 35/5B (1996) L602.
[287] R. Methaapanon, S.M. Geyer, C. Hägglund, P.A. Pianetta, S.F. Bent, Review of Scientific Instruments 84/1 (2013) 015104.
[288] Y.I. Dergunov, V. Gerega, O. D'yachkovskaya, Russian Chemical Reviews 46 (1977) 1132.
[289] D. Davazoglou, Thin Solid Films 302/1-2 (1997) 204.
[290] J. Melsheimer, D. Ziegler, Thin Solid Films 129/1-2 (1985) 35.
[291] J. Montero, C. Guillén, J. Herrero, Thin Solid Films 519/21 (2011) 7564.
[292] J. Perrenoud, L. Kranz, S. Buecheler, F. Pianezzi, A.N. Tiwari, Thin Solid Films 519/21 (2011) 7444.
[293] H. Liu, V. Avrutin, N. Izyumskaya, Ü. Özgür, H. Morkoç, Superlattices and Microstructures 48/5 (2010) 458.
[294] T. Minami, S. Takata, H. Sato, H. Sonohara, Journal of Vacuum Science & Technology A: Vacuum, Surfaces, and Films 13/3 (1995) 1095.
[295] Y. Hayashi, K. Kondo, K. Murai, T. Moriga, I. Nakabayashi, H. Fukumoto, K. Tominaga, Vacuum 74/3-4 (2004) 607.
[296] T. Moriga, Y. Hayashi, K. Kondo, Y. Nishimura, K.-i. Murai, I. Nakabayashi, H. Fukumoto, K. Tominaga, Journal of Vacuum Science & Technology A: Vacuum, Surfaces, and Films 22/4 (2004) 1705.
[297] J.D. Perkins, J.A. del Cueto, J.L. Alleman, C. Warmsingh, B.M. Keyes, L.M. Gedvilas, P.A. Parilla, B. To, D.W. Readey, D.S. Ginley, Thin Solid Films 411/1 (2002) 152.
[298] D.L. Young, D.L. Williamson, T.J. Coutts, Journal of applied physics 91/3 (2002) 1464.
[299] H. Enoki, T. Nakayama, J. Echigoya, Physica Status Solidi A 129/1 (1992) 181.
[300] E. Çetinórgü, S. Goldsmith, Z. Barkay, R. Boxman, Journal of Physics D: Applied Physics 39/24 (2006) 5245.

[301] S. Vijayalakshmi, S. Venkataraj, M. Subramanian, R. Jayavel, Journal of Physics D: Applied Physics 41/3 (2008) 035505.
[302] A. Kurz, M.A. Aegerter, Journal of Sol-Gel Science and Technology 31/1 (2004) 267.
[303] X. Wu, R. Dhere, D. Albin, T. Gessert, C. Dehart, J. Keane, A. Duda, T. Coutts, S. Asher, D. Levi, Proceedings of NCPV program review meeting, 2001.
[304] H.Q. Chiang, J.F. Wager, R.L. Hoffman, J. Jeong, D.A. Keszler, Applied Physics Letters 86/1 (2005) 013503.
[305] G. Zang, J. Wang, H. Chen, W. Su, W. Wang, P. Qi, C. Wang, Journal of Materials Science 39/10 (2004) 3537.
[306] P.R. Bueno, J.A. Varela, E. Longo, Journal of the European ceramic society 28/3 (2008) 505.
[307] J.H. Ko, I.H. Kim, D. Kim, K.S. Lee, T.S. Lee, B. Cheong, W.M. Kim, Applied Surface Science 253/18 (2007) 7398.
[308] J. Perkins, J. Del Cueto, J. Alleman, C. Warmsingh, B. Keyes, L. Gedvilas, P. Parilla, B. To, D. Readey, D. Ginley, Thin Solid Films 411/1 (2002) 152.
[309] M.K. Jayaraj, K.J. Saji, K. Nomura, T. Kamiya, H. Hosono, Journal of Vacuum Science & Technology B: Microelectronics and Nanometer Structures 26/2 (2008) 495.
[310] D.L. Young, H. Moutinho, Y. Yan, T.J. Coutts, Journal of Applied Physics 92/1 (2002) 310.
[311] X. Fu, X. Wang, J. Long, Z. Ding, T. Yan, G. Zhang, Z. Zhang, H. Lin, X. Fu, Journal of solid state chemistry 182/3 (2009) 517.
[312] J. Zeng, M.D. Xin, K.W. Li, H. Wang, H. Yan, W.J. Zhang, The Journal of Physical Chemistry C 112/11 (2008) 4159.
[313] M. Miyauchi, Z. Liu, Z.G. Zhao, S. Anandan, K. Hara, Chemical Communications 46/9 (2010) 1529.
[314] M. Mullings, C. Hägglund, and S.F. Bent, Thin Solid Films (unpublished).
[315] J.T. Tanskanen, J.R. Bakke, T.A. Pakkanen, S.F. Bent, Journal of Vacuum Science & Technology A: Vacuum, Surfaces, and Films 29/3 (2011) 031507.
[316] L. Wachnicki, M. Lukasiewicz, B. Witkowski, T. Krajewski, G. Luka, K. Kopalko, R. Minikayev, E. Przezdziecka, J. Domagala, M. Godlewski, physica status solidi (b) 247/7 (2010) 1699.
[317] Y.R. Luo, Comprehensive Handbook of Chemical Bond Energies, CRC Press, 2007, p. 414.
[318] R.L. Jackson, Chemical physics letters 163/4 (1989) 315.
[319] Y.R. Luo, Comprehensive Handbook of Chemical Bond Energies, CRC Press, 2007, p. 1058.
[320] M. Niederberger, ChemPhysChem 8/4 (2007) 617.
[321] D. Wang, A. Fernandez-Martinez, Science 337/6096 (2012) 812.
[322] Guide to using WVASE32, J. A. Woollam Co., Inc., Lincoln, NE.
[323] S. Venkataraj, S. Hishita, Y. Adachi, I. Sakaguchi, K. Matsumoto, N. Saito, H. Haneda, N. Ohashi, J. Electrochem. Soc. 156/6 (2009) H424.
[324] M. Verghese, J.W. Maes, N. Kobayashi, Solid State Technology 53/10 (2010) 18.
[325] J.A. van Delft, D. Garcia-Alonso, W.M.M. Kessels, Semiconductor Science and Technology 27/7 (2012) 13.

[326] R. Bock, J. Schmidt, S. Mau, B. Hoex, R. Brendel, Electron Devices, IEEE Transactions on 57/8 (2010) 1966.
[327] J.R. Bakke, K.L. Pickrahn, T.P. Brennan, S.F. Bent, Nanoscale 3/9 (2011) 3482.
[328] Beneq, http://beneq.com (Last accessed: January 12, 2013).
[329] T.S. Suntola, A.J. Pakkala, S.G. Lindfors, US Patent No. 44130221983
[330] D.H. Levy, D. Freeman, S.F. Nelson, P.J. Cowdery-Corvan, L.M. Irving, Applied Physics Letters 92/19 (2008) 192101.
[331] D.H. Levy, S.F. Nelson, D. Freeman, Display Technology, Journal of 5/12 (2009) 484.